

ENERGY TRANSFER IN AMORPHOUS SOLID WATER:
LIGHT-MEDIATED EXPULSION OF N₂O₄ GUEST MOLECULES

by

Stephanie Anne McKean

A Dissertation Presented to the
FACULTY OF THE USC GRADUATE SCHOOL
UNIVERSITY OF SOUTHERN CALIFORNIA
In Partial Fulfillment of the
Requirements for the Degree
DOCTOR OF PHILOSOPHY
(CHEMISTRY)

July 2015

DEDICATION

This thesis is dedicated to my mother, Kristine Haataja, for supporting and encouraging me in all aspects of my life while still letting me forge my own path, fully believing in my ability to make my own decisions. It is also dedicated to my late grandparents, Don and Betty McKean, for providing me with access to an education they could never have dreamed of for themselves.

ACKNOWLEDGEMENTS

I would like to start off thanking my advisors, Drs. Curt Wittig and Hanna Reisler. They have both been wonderful and encouraging mentors. They have different styles of mentoring, despite their long research relationship; as co-advisors, they struck a balance that was an ideal environment for me. I am very thankful to both of them for their wisdom, knowledge, and advice. Most importantly, I am thankful for their faith in me.

Jaimie and I have shared an office from day one of graduate school, and ended up working on the same research project. We have pretty much spent the whole day in the same room, five days a week, most weeks of the year, for six years. I have been very fortunate to get “stuck” with a person that I actually enjoy being around, and I cannot express how much our relationship has been essential to my life during graduate school.

Chris brought fresh insight to our project, and really invigorated it. Four years working on the same project can become maddening, especially when there are roadblocks that last for more than six months. He came just when we needed a new perspective, and was a great addition to our research team.

I am grateful to all of my family and friends who have supported me throughout my education. My mom has been a role model of strength and hard work, and always been there when I have needed her. The last person I need to thank is my friend Elianna Rivkin. She has been my constant cheerleader, my #1 fan, and an impossibly positive voice in my life.

TABLE OF CONTENTS

Dedication	i
Acknowledgements	ii
List of Figures	v
List of Tables	viii
List of Equations	ix
Abstract	xi
1 Introduction and Background	1
1.1 Ice and Amorphous Solid Water	3
1.2 NO ₂ and N ₂ O ₄	10
1.3 Methods	13
1.4 Chapter 1 References	20
2 Experimental Set-Up	25
2.1 Laser and Optics	25
2.2 Main Structure of Chamber	28
2.3 Manipulators and Cold Finger	35
2.4 Sample Holder	37
2.5 Instruments Connected to the Chamber	41
2.6 Chapter 2 References	46
3 Experimental Methods	47
3.1 Materials and Experimental Preparation	47

3.2	Sample Deposition	49
3.3	Sample Irradiation	53
3.4	Time-of-Flight Mass Spectrometry	55
3.5	Fourier-Transform Infrared Spectroscopy	57
3.6	Simulating Heat Transfer Behaviors in COMSOL	59
3.7	Chapter 3 References	69
4	Results and Discussion	71
4.1	Single-Species Mass Spectra and Infrared Spectra of Ice	72
4.2	Irradiation of Exposed N_2O_4	80
4.3	Single-Pulse Results from Multi-Layer Samples	85
4.4	Subsequent Pulses Incident on the Same Spot	90
4.5	Fissure Growth in Stages	90
4.6	Isotope Scrambling — Scraping the Walls	92
4.7	Fourier-Transform Infrared Spectroscopic Results	94
4.8	Discussion	95
4.9	Chapter 4 References	102
5	Future Experiments	103
5.1	Expanding the Infrared Range	103
5.2	Introducing Gold Nanoparticles	104
5.3	Chapter 5 References	116
6	Conclusion	117
	Bibliography	120

LIST OF FIGURES

1.1	Schematic drawing of layered films used in this study	1
1.2	A simplified depiction of the differences in bonding between ice I_h , ice I_c , and low-density amorphous ice	4
1.3	The structure of planar N_2O_4 at 100 K	11
1.4	Cartoon of the basic principle of mass separation in a time-of-flight mass spectrometer	16
2.1	A simplified schematic of the experiment	26
2.2	The bench optics	27
2.3	An external view of the entire chamber	29
2.4	The bottom tier of the ultra-high vacuum chamber	30
2.5	The middle tier of the ultra-high vacuum chamber	33
2.6	A diagram of the directed doser	33
2.7	The top tier of the ultra-high vacuum chamber	35
2.8	The cold finger	36
2.9	A front view of the sample holder	38
2.10	An exploded diagram of the sample holder	38
2.11	The top tier of the chamber, with Fourier-transform infrared spectrometer included	42
2.12	Acquisition of a temporal profile via pulsed time-of-flight mass spectrometry	44
3.1	Temperature-programmed desorption traces for 12 to 60 Langmuirs of H_2O exposure	51
3.2	Integrated signals from Figure 3.1 as a function of exposure.	51
3.3	Calibration of the directed doser using H_2O	53

3.4	Nine-spot irradiation scheme and Fourier-transform infrared spectroscopy irradiation scheme	55
3.5	Heat capacity of solid N_2O_4 as a function of temperature	61
3.6	Heat capacities of ice I_h and low-density amorphous ice	63
3.7	Geometry of a $\text{H}_2\text{O}(\text{as})/\text{N}_2\text{O}_4$ film, as used in COMSOL	67
4.1	Schematic drawing of layered films used in this study	71
4.2	Apertured time-of-flight mass spectrometer accelerating plates	75
4.3	Gas-phase mass spectra of NO_2 , NO , H_2O , and N_2O_4	75
4.4	Fourier-transform infrared spectra of $\text{H}_2\text{O}(\text{as})$, a partially crystallized film, and ice I_c	79
4.5	Mass spectra of exposed N_2O_4 subjected to focused 266-nm radiation (1 mJ), presented on the same scale; (a) no spacer between 80 L of N_2O_4 and MgO ; (b) spacer of 180 L of $\text{H}_2\text{O}(\text{as})$. Thermal insulation increased signal intensity	80
4.6	Evolution over time of the maximum temperature of a 50-nm film of N_2O_4 atop 0–60 L of $\text{H}_2\text{O}(\text{as})$ on a MgO substrate. At $t = 0$, the MgO and $\text{H}_2\text{O}(\text{as})$ are at 100 K, and the N_2O_4 is at 400 K. Increasing the thickness of the $\text{H}_2\text{O}(\text{as})$ layer decreases the rate of cooling of the N_2O_4 layer	81
4.7	Extractions from the temporal profile at 20 and 150 μs (black arrows in panel a) yielding the mass spectra shown in panels b and c, respectively. The film composition is depicted in the upper left. At 20 μs , neutral NO_2 plays a significant role; its role is diminished at later times	84
4.8	Temporal profiles and mass spectra for upper $\text{H}_2\text{O}(\text{as})$ layer thickness: (1) 360 L, (2) 720 L, and (3) 1440 L of $\text{H}_2\text{O}(\text{as})$ over 40 L N_2O_4 (from 80 L of NO_2) and 180 L of $\text{D}_2\text{O}(\text{as})$	87
4.9	R_N values for a large number of extractions: First-pulse R_N values settle down after the first few extractions to values of order unity. Second-pulse R_N values are consistent with the presence of a significant amount of N_2O_4 in the surface region	89
4.10	Temporal profiles of desorbed material for different spots on 1440 L of $\text{H}_2\text{O}(\text{as})$ over a N_2O_4 film and an $\text{H}_2\text{O}(\text{as})$ thermal buffer layer	89

4.11	Temporal profiles are shown for a second 1-mJ laser pulse at the same locations as in Figure 4.8	91
4.12	(a) and (b) show spectra for extractions at 50–60 μ s, following first-pulse 266-nm irradiation (1.5 mJ) for samples that have 40 L of N_2O_4 atop a 180 L $H_2O(as)$ spacer and alternating $H_2O(as)$ and $D_2O(as)$ upper layers. In (a), the upper amorphous solid water layer has 120 L of $D_2O(as)$ atop 120 L of $H_2O(as)$, and in (b) this is reversed. In (c), a spectrum of 300-K gaseous D_2O recorded the same day shows only modest HDO contamination.	93
4.13	Transmission Fourier-transform infrared spectra of a $D_2O(as)/N_2O_4/H_2O(as)$ film before and after irradiation	94
4.14	Cartoon illustrating how fissure effluents might interact	98
4.15	Surface temperature of 360, 720, and 1440-L films over $H_2O(as)$ over 40 L N_2O_4 and 180 L $H_2O(as)$ after heating the N_2O_4 to 400 K . . .	100
5.1	Formation of “chimneys” by irradiating a gold nanosphere embedded in amorphous solid water and N_2O_4	105
5.2	Heat transfer from a 400-K gold nanosphere into a surrounding matrix	108
5.3	Atomic force microscopy image of bare MgO	110
5.4	Atomic force microscopy image of 20-nm gold nanospheres on MgO .	111
5.5	How an atomic force microscope tip creates artifacts in the imaging of small particles	111
5.6	Time-of-flight spectra of water desorbed via irradiation of 20-nm gold nanospheres with amorphous solid water on top	113
5.7	Atomic force microscopy image of 80-nm gold nanospheres on MgO before and after laser irradiation	114

LIST OF TABLES

3.1	Values for heat capacity, thermal conductivity, and density of MgO, N ₂ O ₄ , and H ₂ O(as) at 100 K.	66
4.1	A summary of the relative amounts of each daughter ion for pure NO, NO ₂ , and N ₂ O ₄	74
4.2	70-eV ionization cross-sections of relevant molecules	76
4.3	Peak areas and $R_N = \text{NO}^+/\text{NO}_2^+$ values for the spectra in Figure 4.8	86
4.4	Peak areas and R_N values for the spectra in Figure 4.11	88
5.1	Properties of nanoparticles for proposed future experiments	110

LIST OF EQUATIONS

1.1	Primary dissociation pathway of N_2O_4 near 266 nm	11
1.2	Force experienced by a charged particle in an electric field	16
1.3	Classical equation for the kinetic energy of a particle	17
1.4	Beer's Law	18
3.1	Time-to-mass conversion for the time-of-flight mass spectrometer . . .	56
3.2	The Jacobian used to transform the time-of-flight signal intensity from the time domain to mass	56
3.3	Power needed to maintain fluence with large spot size	58
3.4	Classical formula for thermal conductivity	63
3.5	Effective Medium Theory model of the reduction in thermal conductivity due to porosity	65
3.6	Effective Medium Theory model for porous amorphous solid water . .	65
3.7	Equation for heat transfer into a highly conductive layer	66
3.8	Eq. 3.7, reduced to fit the model parameters	67
3.9	Thermal insulation equation, used for boundaries	67
3.10	Heat transfer in solids	67
4.1	The amount of parent-ion NO_2^+ in a time-of-flight spectrum	76
4.2	The amount of parent-ion NO^+ in a time-of-flight spectrum	77
4.3	The amount of parent-ion O^+ in a time-of-flight spectrum	77
4.4	First step in deriving Equation 4.6	77
4.5	Second step in deriving Equation 4.6	77
4.6	Relationship between NO_2 and N_2O_4 fragments	78

5.1	Plasmon resonance frequency	105
5.2	Drude-Sommerfeld model for the size-dependant contribution to the dielectric function of a nanoparticle	105
5.3	Nanoparticle diameter-dependent damping effects	105

ABSTRACT

Molecular transport and morphological change were examined in films of vapor-deposited amorphous solid water, $\text{H}_2\text{O}(\text{as})$. A buried N_2O_4 layer absorbs pulsed 266-nm radiation, creating heated fluid. Temperature and pressure gradients facilitate the formation of fissures through which fluid travels to vacuum. Film thickness up to 1440 Langmuirs was examined. In all cases, transport to vacuum could be achieved with a single pulse. Material that entered vacuum was detected using a time-of-flight mass spectrometer that recorded spectra every 10 μs . An amorphous solid water layer insulated the N_2O_4 layer from the high-thermal-conductivity $\text{MgO}(100)$ substrate; this was verified experimentally and with heat transfer calculations. Laser-heated fluid strips water from fissure walls throughout its trip to vacuum. Experiments with alternate $\text{H}_2\text{O}(\text{as})$ and $\text{D}_2\text{O}(\text{as})$ layers reveal efficient isotope scrambling, consistent with water reaching vacuum via this mechanism. It is likely that ejected water undergoes collisions just above the film surface due to the high density of material that reaches the surface via fissures. Little material enters vacuum after cessation of the 10 ns pulse because cold amorphous solid water near the film surface freezes material that is no longer being heated. A proposed model is in accord with the data.

A commercial program (COMSOL Multiphysics[©]) was used to simulate the heat transfer behavior of a multi-component system comprising solid N_2O_4 and ASW strata supported by a MgO substrate, wherein the application of heat to the amorphous solid water occurs via transfer from the N_2O_4 . The N_2O_4 layer is heated, and the system is allowed to evolve. The transience of elevated temperatures is consistent with transmission Fourier-transform infrared spectroscopy of the films before and after irradiation, together leading us to conclude that crystallization does not occur in the amorphous solid water upon irradiation of the guest molecules. The time for

heat to travel to the surface of an $\text{H}_2\text{O}(\text{as})/\text{N}_2\text{O}_4/\text{H}_2\text{O}(\text{as})$ sample with a thick upper layer argues for material transport via fissures, and not via surface evaporation.

CHAPTER 1: INTRODUCTION AND BACKGROUND

Molecular transport and morphological change were examined in a form of low-temperature solid water referred to as amorphous solid water, or $\text{H}_2\text{O}(\text{as})$. This material accounts for most of the water in the universe [1]. It has been the subject of intense research, motivated mainly by intellectual curiosity and the role it plays as a molecular factory in the interstellar medium [2]. Layers of N_2O_4 and amorphous solid water held at 100 K were irradiated with 266-nm laser pulses to selectively heat the N_2O_4 layer, as depicted in Figure 4.1. Desorbed material was detected using time-of-flight mass spectrometry, and the films were probed using transmission Fourier-transform infrared spectroscopy to detect material loss and morphological changes in the solid water layers.

This chapter introduces the fundamental concepts for the experiments presented herein. The properties of amorphous solid water are discussed in contrast to other forms of solid water, and why it is a material of interest. In particular, it will give insight into the astrophysical relevance of amorphous solid water. It will also introduce the properties of solid N_2O_4 , and why it is both a molecule of interest and why it is appealing as a probe of amorphous solid water and of the escape of heated guest molecules from a porous medium. Lastly, the principles of laser irradiation,

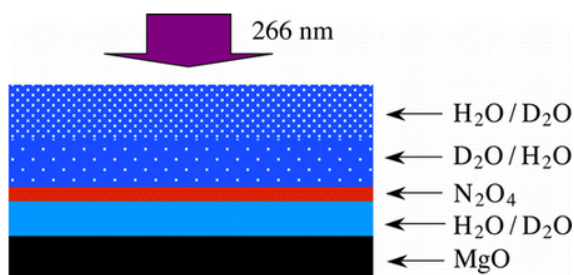


Figure 1.1: Schematic drawing indicating the structure of the films used in the present study. The black layer is the MgO substrate. Solid blue is an amorphous solid water layer that insulates the (red) N_2O_4 layer from the MgO, which has high thermal conductivity. The upper layer can be amorphous H_2O , D_2O , or a combination.

pulsed time-of-flight mass spectrometry, and transmission Fourier transform infrared spectroscopy are discussed.

Chapter 2 describes the ultra-high vacuum chamber and its instrumental components. Methods used in preparing the chamber for experimentation will be included.

Chapter 3 describes the experimental methods. It describes sample preparation and the methods used to acquire and process data. It intends to show that all aspects of the experiments were taken into consideration to yield high-quality data and to support experimental replication of results.

The results of these experiments and their interpretation are presented in Chapter 4. Results are presented in an order that shows the progressive build-up of information from these experiments until a cohesive model is constructed. A series of time-of-flight mass spectrometry studies on a variety of $\text{H}_2\text{O}(\text{as})/\text{N}_2\text{O}_4$ systems each provides insight; Fourier-transform infrared spectroscopic studies are then presented. Computational simulations that support the interpretation of the results are also presented and discussed.

Chapter 5 suggests further research on this and related systems. This includes improvements to the current experimental set-up, and some of the preliminary steps taken to venture into the next stages of experimentation.

Lastly, Chapter 6 summarizes the findings of these experiments and relates them to the goals of the experiments. It also remarks on the relationship between the conclusions made from the experiments presented herein and the insight into the relevant systems of interest.

1.1 Ice and Amorphous Solid Water

Water's unique properties sustain life as we know it. Beyond its abundance on Earth, water plays a potentially vital role in phenomena both within and exterior to our solar system. On a macroscopic scale it forms icy mantles on moons, comets and asteroids; in an analogous fashion, it forms layers on microscopic dust particles everywhere from the rings of Saturn to the vast, diffuse clouds in star forming regions of the interstellar medium [3–8].

1.1.1 *Properties of Solid Water*

Including the recently-discovered structure of a de-gassed clathrate hydrate, there are currently 17 crystalline phases of water-ice that have been classified [9]. They form under a range of pressures and temperatures and are denoted by roman numerals I–XVI, although ice I has been further divided into I_h , which has a hexagonal crystal structure, and I_c , a cubic structure that is metastable with respect to I_h [10, 11]. Only ice I_h , I_c , and XI, however, can be formed at or below atmospheric pressure [12].

Water-ice that is amorphous, as opposed to crystalline, is a metastable polymorph that can exist at temperatures as high as 155 K. In the range 130–155 K, what existed as an amorphous solid at lower temperatures is a highly viscous liquid [1, 13]. Above 155 K, it irreversibly undergoes a phase transition to cubic ice (ice I_c), which can then irreversibly transition to hexagonal ice (ice I_h) around 230 K [11, 14, 15]. Crystalline ice I_h and I_c are composed of puckered sheets of water molecules arranged in repeating hexagons of hydrogen-bonded water molecules (Fig. 1.2). In ice I_h , these sheets are hydrogen bonded to one another with the hexagons aligned. In ice I_c , the sheets are offset. Amorphous ice formed at 100 K has the same intrinsic density as ice I_h . On

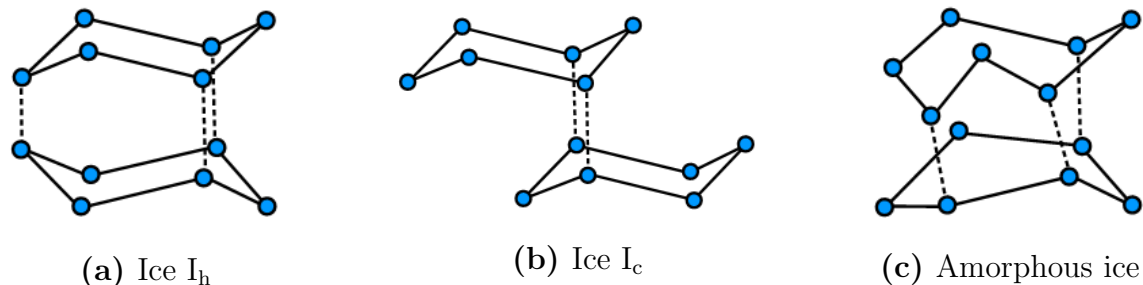


Figure 1.2: A simplified depiction of the differences in bonding between ice I_h , ice I_c , and low-density amorphous ice. Only the oxygen atoms are shown, and all lines represent hydrogen bonds. Water molecules form a puckered sheet of repeating hexagons; the dashed lines indicate hydrogen bonds that connect these sheets.

average, its oxygen molecules occupy the same locations as ice I_h , but with a greatly increased standard deviation of position. Amorphous ice is also proton-disordered [16].

Amorphous ice has been resistant to consistent characterization because different methods of preparation result in different macroscopic material “textures,” resulting in poorly defined physical properties. Properties of vapor-deposited amorphous solid water depend on temperature, rate, method, and substrate, so conditions need to be specified [17]. Methods of preparation include high-pressure amorphization of hexagonal ice (the structure of which persists at atmospheric pressure as long as sufficiently low temperatures are maintained); rapid thermal quenching of liquid water micro-droplets; and vapor-deposition at low temperatures and pressures via a molecular beam or an effusive flow [1, 11, 15, 18]. Many studies into the physical properties of amorphous ice have been conducted, and an understanding of how these different forms of amorphous ice behave has slowly been cultivated.

Terminology regarding amorphous ice can become a hindrance in the literature because of the varied behavior of what is, ostensibly, the same material. Amorphous ice, the general term which will be used here to encompass all forms, has been classified into sub-groups to differentiate between the different textures and their properties. Pressure-amorphized ice comes in two forms: a high-density amorph and a low-density

amorph. These two forms, which have been differentiated from one another based on density and X-ray diffraction measurements, are homogeneous and non-porous, which facilitates characterization [1, 6, 11]. Hyper-quenched glassy water, amorphous ice formed of quenched micro-droplets, is inherently granular in the bulk, and its porous nature is due in part to the voids between granules [19]. Amorphous ice formed by vapor-deposition has not acquired a unique term, but is often referred to by the general term “amorphous solid water” or “vapor-deposited amorphous solid water”. Here, the term “amorphous solid water” or $\text{H}_2\text{O}(\text{as})$ will be reserved for amorphous ice that has been produced by vapor deposition, as this is the method used for this work.

A pressure-amorphized ice, high-density amorphous ice, is created by the application of >1.2 GPa at 77 K. It is metastable with respect to low-density amorphous ice — it irreversibly transforms to the low-density amorph upon depressurisation at 130 K. Low-density amorphous ice has a more stable structure and maintains that structure when the temperature is reduced to the regime where high-density amorphous ice can form [12].

The role of water on Earth and its presence beyond our planet are sufficient to argue that it is important to understand any naturally forming state of water. However, two applications are particularly relevant to this research, despite the fact that an exploration of phenomena specifically related to them is not its goal, per se. The role of water in space is an area of research which can gain insight from these experiments because they concern water at low temperature and pressure.

1.1.2 Astrophysical Interest in Amorphous Solid Water

“Water, water, everywhere

Nor any drop to drink”

Coleridge's *The Rime of the Ancient Mariner* referred to seawater, but the same can be said of any known region of space outside our solar system: the most abundant form of water in the universe is amorphous ice [1, 20, 21]. It has been detected on dust grains in the interstellar medium and in dense star-forming regions, and is a component of the heterogeneous dust-and-ice regolith that makes up the bulk of cometary bodies [8, 22]. Amorphous ice has also been detected on bodies in our solar system, most notably on the surface of Enceladus, a moon of Saturn [23, 24].

Between 2005 and 2014, the *Cassini* spacecraft made multiple flybys of Enceladus, on one occasion reaching as close as 74 km from its surface [25]. The surface of Enceladus is a frozen tundra of almost pure water-ice, largely marred by tectonic activity and with craters from impacts [26]. At the southern pole, however, are four enormous, roughly parallel fissures, the area near which is largely devoid of craters but patterned with smaller fractures. The main fissures are each roughly 130 km long, 2 km wide, and about 500 m deep, bordered by mountainous 100-m ridges [27]. These fissures have been collectively termed the “tiger stripes” [28]. Along these massive fractures, distinctly visible curtains of material erupt, and contribute 3.4% of the mass of an enormous plume of material emitted along the tiger stripes that spans 70,000 km², equivalent to 9% of Enceladus' surface [27, 29–31]. This plume extends upwards of 435 km above the surface and is 90% H₂O (both solid and vapor), 5% CO₂, 1% N₂, and 1% CH₄, with traces of simple organics [27, 32].

Broadband reflection spectra taken by *Cassini* show that the tiger stripes themselves are composed of ice grains of around 100 μm, but highly reflective regions between the stripes show little to no absorption, indicating grains on the order of tens of micrometers [27]. These crater-free regions between the tiger stripes are 10% brighter than the rest of Enceladus. This is quite remarkable — the surface of Enceladus as a whole has the highest solar reflectivity of any body in our solar system, and is consistent with the reflectivity of fresh snow or ice [26, 27]. Indeed,

only an estimated 1% of erupted particles escape Enceladus, with the remaining 99% falling back to its surface as fresh, microparticulate snow [27]. Ice on Enceladus is partially amorphized by ion bombardment [24].

Aside from the south polar terrain, the surface of Enceladus has a daytime temperature around 75 K, but temperatures in the fissures can exceed 200 K [25, 26, 29]. Porco et al. (2014) found that geyser activity is unequivocally related to thermal emission, although it is not immediately clear which effect causes the other [29].

The high fissure temperatures, and the presence of sodium and potassium salts in the plume point to the presence of a salty, liquid ocean which geysers through tens of kilometers of an icy mantle. Recent measurements of the gravitational forces at the south polar terrain showed significant gravitational anomalies at the south pole that further indicate a reservoir of liquid water located 30 km below the surface and extending to a depth of 10 km further [33].

Cumulatively, *Cassini* data point to the presence of a regional, salty ocean which geysers through tens of kilometers of ice crust at the tiger stripes. The activity of individual geysers is modulated by the plugging and reopening of established cracks, and activity of the plume as a whole is modulated in part by tidal stresses on the crust. Salt-laden water droplets typically freeze and fall back to the surface, while vapor components with enough velocity to escape Enceladus have the potential to join Saturn's outermost ring and condense into individual ice particles, with or without dust grains as a nucleation center [29].

Before the formation of Enceladus even occurred, water likely played a part. Amorphous solid water may, in fact, be a critical participant in the formation of planets [34]. Amorphous solid water has been detected in molecular clouds, often referred to as the "nurseries" of protoplanets and protostars [35]. Molecular clouds make up the interstellar medium, which is composed of gases and a small amount of

dust that exists between stars; materials in the interstellar medium make up 20-30% of the mass in our galaxy [36, 37]. These micron-sized dust grains, which make up only about 1% of the mass of the interstellar medium, are thought to be mainly composed of silicates and carbonaceous materials [8, 37].

Molecular clouds in the interstellar medium are very inhomogeneous, but generally cold (10–106 K) and dense (100 to $> 10^4$ particles/cm³) [35, 38]. This leads very naturally to experiments such as ours, conducted at 100 K in an ultra-high vacuum chamber. In the coldest and densest regions of the interstellar medium, where dense molecular clouds are found and the first stage of star formation is initiated, water and other molecules accrete onto dust grains to form an icy mantle [35, 36, 39, 40]. Depending on the temperature range, the mantle may be almost entirely water ice, or it may also include ices such as CO₂, CO, methanol, and others [8, 40]. At 10 K, one would expect to find hardly any molecules in the gas phase; they should all have accreted onto dust grains. However, much more material has been found in the gas phase than expected. This suggests an equilibrium between accretion and desorption processes [41].

When a new star is formed, there is a limited time to begin the first stages of planet formation — the agglomeration of dust must occur more quickly than it is dispersed. Aggregates form more quickly than can be accounted for by invoking only van der Waal’s forces [42]. Wang et al. (2005) found that amorphous ice can aid in the formation of agglomerates both mechanically and through acquired, persistent electric dipoles. Amorphous ice that has coated fragile dust particles prevents their fragmentation upon impact because it reduces the elasticity of the collision, and strong dipole forces enhance the adhesion between grains to facilitate aggregation of particles [34].

The bulk of water ice accreted on dust particles is amorphous, with some components of cubic ice depending on the thermal conditions that grains have

experienced [6, 43]. Microporous amorphous ice has unique properties for trapping guest molecules within its pores [44–48]. Over 180 different molecules, mostly organics, have been detected in the interstellar medium — a much richer variety of compounds than can be explained by gas-phase chemistry alone [8, 35, 37]. It has been shown that interactions between the pore structure and guest molecules increase their adsorption energy, reduce the ionization energy of the guest molecule, and retain both neutral and ionized molecules within its pores to temperatures higher than adsorption dynamics would generally allow [49–51]. Once trapped, atoms and molecules can undergo thermal hopping and, if they encounter another guest molecule, react to form more complex compounds [8, 39]. Thermal energy can be provided to these systems via grain-grain collisions and irradiation with cosmic rays or UV radiation [35, 37, 39, 41]. Thus, icy grains in the interstellar medium are not considered surface catalysts as much as reservoirs, which increase the likelihood of two molecules interacting with one another [35].

Comets are also formed in such regions, and are considered to be the most primitive components of the solar system. Comets are porous composites of both amorphous and crystalline water, mixed with rocky debris; they can house up to 20% of its mass as trapped impurities [43]. Comets in the Oort cloud originated in the trans-Neptunian region, and underwent thermal processing up to 100 K before being ejected to the Oort cloud [6, 37]. Oort cloud comets likely have a high-density amorphous ice mantle due to interaction with cosmic rays, but it is thought that their cores remain low-density amorphous ice [6]. The properties of comet surfaces are largely controlled by structural changes induced by thermal processing [43]. When comets enter warmer regions, such as our solar system, some of the water ice crystallizes and ejects guest molecules, creating the coma we view from earth as a cometary “tail”; solar radiation can additionally induce photolysis to produce radicals and ions [37, 43].

Icy grains in the interstellar medium are a system that is closely related to this work; there is a high level of overlap. However, it must be stressed that these experiments are not intended to specifically replicate or model the types of interactions that occur in the interstellar medium, despite the insight that they provide.

1.2 NO₂ and N₂O₄

There exists a wealth of research that has already been done regarding NO₂. Nitrogen dioxide has been extensively studied, in part because of its relevance to atmospheric processes and pollution and its properties and energy transitions are quite well defined. While NO₂ is not found in the interstellar medium, it is an appealing probe molecule for understanding processes in the interstellar medium.

1.2.1 Properties of NO₂/N₂O₄

The equilibrium between NO₂ and its dimer, N₂O₄, has been studied for more than 100 years, undoubtedly in part because its existence is strikingly visible — in both the gas and liquid phase NO₂ is intensely brownish-orange, while N₂O₄ is colorless [52]. A classic demonstration is to place a transparent container of NO₂/N₂O₄ in an ice-bath, visibly driving the equilibrium from colored NO₂ towards colorless N₂O₄.

The planar N₂O₄ molecule has D_{2h} symmetry. At 100 K, the O–N–O bond angle is 134.5° and the N–O bond length is 1.186 Å. The dimeric N–N bond is unusually long: at 100 K, it is 1.756 Å. For comparison, the N–N bond length of hydrazine, N₂H₄, is 1.449 Å [53, 54]. Accordingly, the N–N bond of N₂O₄ is extremely weak (13.6 kcal/mol) in comparison to hydrazine (64 kcal/mol); this tenuous bond is why dimerization of NO₂ to N₂O₄ is an equilibrium system under standard conditions

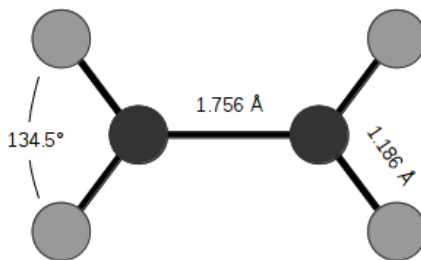


Figure 1.3: The structure of planar N_2O_4 at 100 K.

[53, 55]. Structural calculations by Bauschlicher et al. (1983) indicate that this long bond is a result of three bonding features: a σ bonding and antibonding correlation which results in an elongated bond; some π bonding, which shortens the bond and results in the planar structure; and some oxygen lone pair electron interactions which adds to the length of the bond by mixing non-bonding resonance structures [56].

Solid N_2O_4 can exist in two crystalline forms: the stable $\alpha\text{-N}_2\text{O}_4$ form with a cubic crystal structure, and metastable monoclinic $\beta\text{-N}_2\text{O}_4$. N_2O_4 condensed from vapor at 145 K and low deposition rates forms a pure, ordered film of $\alpha\text{-N}_2\text{O}_4$ [57, 58]. At 80 K, highly crystalline N_2O_4 is formed, and at 120 K a polycrystalline film results [58].

At 266 nm, the absorption cross-section of N_2O_4 is $7.3 \times 10^{-19} \text{ cm}^2$ [59]. At 248 nm, the primary dissociation process for N_2O_4 on water-ice is



However, this process can be quenched by a surrounding water matrix. Because the water ice acts as an efficient bath for cooling, the internal and translational energy of the NO and O are in a mostly relaxed state [60]. This relaxation process transfers thermal energy to its surroundings.

1.2.2 *Astrophysical Interest*

As mentioned, the interstellar medium contains a variety of small molecules whose formation may be greatly facilitated by the trapping behaviors of amorphous solid water. While embedded in amorphous solid water, guest molecules can undergo photoionization, photodesorption, and thermal processing, all of which can contribute to the destruction and/or chemical reaction of trapped compounds [8]. Many studies have explored the trapping and release of astrochemically relevant guest molecules, including N_2 , H_2 , CO , CO_2 , CH_4 , C_6H_4 , and more, in amorphous solid water [47, 61–64].

Desorption of water and guest molecules has been studied as a phenomenon called the “molecular volcano,” where they are violently ejected upon crystallization of amorphous solid water. May, Smith, and Kay (2013) studied the expulsion of material via the molecular volcano effect and showed that the formation of crystallization-induced cracks exposed an embedded layer of guest molecules and provided a pathway to vacuum. These experiments were conducted via a warming of the entire deposited film [65, 66]. In our own lab, the expulsion of CO_2 guest molecules from amorphous solid water/ CO_2 films has been explored both by heating the films to induce molecular volcano-type expulsion and by a laser-induced molecular volcano from selective heating of the amorphous solid water [67, 68].

The selective heating of a guest species, however, has not been explored as thoroughly. Irradiation of guest molecules has often been used to induce chemical reactions. Bernstein et al. (1999) studied UV processing of polycyclic aromatic hydrocarbons in amorphous solid water, but thermal processes and morphological changes in the water matrix were not the focus; amorphous solid water was used as a molecular reservoir [69].

NO and O_2 are both found in space, albeit not in large quantities, and it has

been found that NO and O₂ can react on cold surfaces to form NO₂ [70]. NO₂/N₂O₄ does not seem to play any significant role astrochemically, but the thermal processing of guest molecules via non-ionizing radiation to which amorphous solid water is transparent is of interest due to the myriad chemical processes which occur on icy dust grains in the interstellar medium [2, 8].

N₂O₄ deposited as a guest molecule in amorphous solid water provides the opportunity to probe the existence of chemical reactions within the water matrix as well as expulsion phenomena that occur when a guest species is selectively excited. The physical properties of N₂O₄, such as its freezing point, vapor pressure at 100 K, and that it absorbs in the UV all contribute to its appeal as a guest molecule, despite its apparent absence in the interstellar medium.

1.3 Methods

Experiments are initiated with laser irradiation. A plume of material emanating from the sample surface is detected using time-of-flight mass spectrometry. Changes in the sample can then be detected via transmission Fourier-transform infrared spectroscopy.

1.3.1 Irradiation with 10-ns, 266-nm laser pulses

There are three ways in which material may leave a surface in response to laser irradiation: sublimation or vaporization; heterogeneously nucleated boiling; and homogeneously nucleated explosive boiling [71].

Sublimation and evaporation do not depend on either laser fluence or pulse duration [71]. These processes involve heating of material but do not have a threshold to activation: any increase in temperature of a material will increase its

rate of desorption, as the temperature increase coincides with a change in the material's equilibrium vapor pressure [71]. Although these processes are not inherently dependent on fluence or pulse duration, the amount of material removed is usually negligible or non-existent with low fluences or on a time-scale < 1 ns [71].

Boiling is initiated by the heterogeneous nucleation of vapor bubbles, and has a temperature threshold that the material must meet or surpass. The bubbles then may diffuse through the material and, if a sufficient length of time is spent above the boiling temperature, it may diffuse all the way to the surface of the material and release the vapor. The diffusion is, however, slow enough that this does not typically occur on time scales < 100 ns [71].

Explosive boiling, which is also termed "phase explosion," occurs when material is superheated to temperatures near the critical temperature. Explosive boiling involves the homogeneous, rapid breakdown near the surface, as the rate of heating exceeds the rate of thermal relaxation [72]. Molecular dynamics simulations by Zhigilei et al. (1998) show that this results in a constant-volume heating and a pressure buildup which exceeds the mechanical strength of the surface layer, which then expels vapor, molecular clusters, and droplets of the liquid phase. The ejected plume of material cools rapidly [72]. Lower fluences lessen the degree of superheating, i.e., lower maximum temperatures are reached. This results in a less violent explosion, and a higher fraction of clusters compared to individual molecules [72]. Thus, the presence or absence of clusters at varying fluences can indicate the dominant processes which occur by irradiating the system.

Previous work in our lab has shown this effect. Using infrared radiation resonant with vibrational modes of water ($2.94 \mu\text{m}$), 10-ns pulses induced the desorption of water monomers, CO_2 guest molecules, and protonated water clusters, $(\text{H}_2\text{O})_n\text{H}^+$. Water clusters of $n = 1$ up to $n = 6$ were routinely detected by pulsed time-of-flight mass spectrometry in the same manner used for the experiments presented herein;

occasionally, clusters up to $n = 9$ were observed [68].

Desorption of water in this previously-explored system was induced by the absorption of vibrational energy [68, 73]. In contrast, in the experiments presented here, 266-nm radiation is resonant with the N_2O_4 *guest* molecules in the water matrix, not the water matrix itself. Note the connection to processes that occur in the cryo-volcanic activity of Enceladus: the initially heated material is not the surface material, but a sub-surface material which then may escape due to pressure gradients in the system. Heating of the surface layer (in this case, an $\text{H}_2\text{O}(\text{as})$ layer atop the N_2O_4) *can occur only via thermal transfer from the guest material*.

The 266-nm radiation is above the energetic threshold to break the N–N dimer bond of N_2O_4 . N_2O_4 undergoes an electronic excitation at 266 nm, and this rapidly decays to excited vibrational states which break the dimer bond and transfer heat to its surroundings.

1.3.2 Pulsed time-of-flight mass spectrometry

When a laser pulse desorbs material from a surface, the material expands in an ellipsoidal plume with its axis normal to the surface [74–76]. Even though a small amount of material is expected to desorb from the surface, the plume itself will have a high local pressure (*i.e.*, high particle density) that is sufficient for detection by time-of-flight mass spectrometry. Pulsed time-of flight mass spectrometry can be used to analyze the resulting plume over time; but, unlike a quadrupole mass spectrometer, it offers the ability to detect multiple masses ejected simultaneously from the surface. With a high enough repetition rate to sample the plume multiple times as it passes through the ionizing region, the plume content can be monitored over time.

There are three basic steps to the acquisition of a mass spectrum from a Wiley-McLaren-type, linear time-of-flight mass spectrometer. First, material enters the

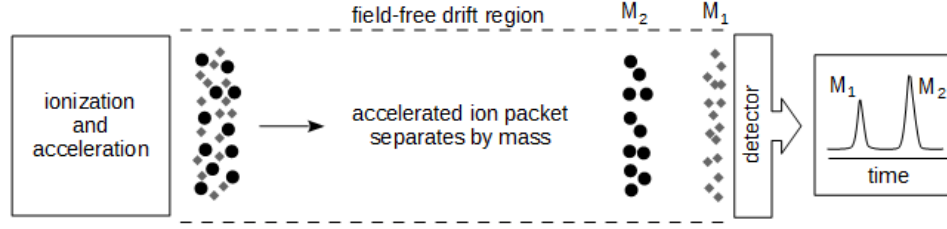


Figure 1.4: Cartoon of the basic principle of mass separation in a time-of-flight mass spectrometer. In a pulsed time-of-flight mass spectrometer, repeated ionization and acceleration results in a train of ion packets, producing a series of time-of-flight spectra with a time separation equal to the temporal separation of the pulses.

ionizing region, where the particles acquire a positive charge through the loss of an electron (*e.g.*, via electron impact ionization). The second step is the acceleration of cations. Charged plates create an electric field and accelerate cations into a field-free drift region [77]. In these experiments, the plume enters the ionizing region perpendicular to the direction it is accelerated, and the plates are pulsed. For a period of time, the two plates on either side of the ionizing region are supplied with the same voltage, and there is no gradient in the electric field between them. Particles flow freely between the plates. One of the plates then drops in voltage, creating a gradient and simultaneously deflecting the electron beam so that it does not ionize any particles during the duration of this pulse. The gradient accelerates the ions down the drift tube [78]. The force with which each particle is accelerated can be expressed as:

$$\vec{F} = -q \frac{\Delta V}{d} \quad (1.2)$$

where \vec{F} is the applied force, q is the charge given to the particle (equivalent, in this case, to the positive charge from the loss of an electron), ΔV is the difference in voltage between the two plates, and d is the distance between the plates.

Third, the ions become temporally separated according to their individual mass-to-charge ratio (Fig. 1.4). Note that when the electron ionizer is pulsed, it

creates a short packet of ions. Each ion is given the same kinetic energy, because each particle receives the same force per unit charge (some particles may be doubly ionized). Identical kinetic energies, however, will result in differing velocities for particles of different masses [78]. This can be shown by Equation 1.3, where E_K is the acquired translational kinetic energy, m is the mass of the particle, and v is its acquired velocity in the direction of acceleration [79].

$$E_K = \frac{1}{2}mv^2 \quad (1.3)$$

Within one pulsed extraction, masses are temporally separated in the field-free drift region before impacting the detector. From one extraction to the other, however, we can observe one temporal “slice” of the emergent plume and differentiate it from the subsequent temporal slice. With each “slice” a full mass spectrum is obtained. Differences in the peak intensities, *i.e.*, relative quantities, can be measured over time.

Ions created by electron impact ionization have varying degrees of stability. Some ionized molecules will dissociate while traveling to the detector; some will remain intact. However, the way in which the molecule fractures is specific to the molecule [79]. Thus, molecules such as N_2O_4 , which cannot survive as N_2O_4^+ because of its exceptionally weak dimer bond, will have a distinctly different cracking pattern from its monomer, NO_2 . Relationships between the peak areas of different ion fragments can indicate the relative quantities of molecular species that existed pre-ionization [77, 79, 80].

1.3.3 Transmission Fourier-transform infrared spectroscopy

In these experiments, transmission Fourier-transform infrared spectroscopy is used to monitor the O–H stretch of amorphous solid water. Fourier-transform

infrared spectroscopy uses a broadband infrared source with a detector, and measures the changes in intensities at different wavelengths between an empty sample (bare MgO) and a sample of condensed H₂O. The infrared light absorbed by the sample depends on the energetics of the molecular interactions and on the amount of absorbing material that is present. For morphologically identical samples, a difference in signal intensity, A , at a given wavelength, λ , will depend only on the amount of material present, N , according to Beer's Law:

$$A_\lambda = \epsilon_\lambda N \quad (1.4)$$

where ϵ_λ is a wavelength-specific coefficient of absorption. With the same morphologies and thus the same energetic interactions, the absorption coefficient will be constant for a given wavelength and the signal intensity will be proportional to the amount of material present. Differences in morphology, however, can change the values of ϵ_λ .

Fourier-transform infrared spectroscopy can be very sensitive to morphological changes. The spectra of material can change with temperatures without having undergone a phase change; temperature affects the strength of inter- and intramolecular interactions and thus the energetic signature of IR light absorption. Even though water, crystalline ice, and amorphous ice all have tetrahedral coordination with surrounding water molecules, they each have different spectroscopic signatures. Ice I_h and amorphous ice have long been known to have distinctly different infrared signatures [81].

Fourier-transform infrared spectra vary even between amorphous ice deposited under different conditions, such as the deposition temperature, method, and the resulting porosity [82]. For amorphous ice deposited by an effusive molecular beam, changes in the beam angle, which changes the resulting porosity of the film, causes

subtle changes in the infrared spectrum as detected by reflection-absorption infrared spectroscopy. Cholette et al. (2009) found a slight red-shift in the maximum of the intramolecular O–H stretching band near 3400 cm^{-1} , due to an increase in the coupled H-bonded O–H stretching vibrations of the bulk amorphous solid water [83]. Manca et al. (2004) found modifications in transmission Fourier-transform infrared spectra of amorphous ice due to the effects of annealing; they attributed these changes in part to micropore collapse [84].

Fourier-transform infrared spectroscopy can also be used to probe solid N_2O_4 . However, the major absorption peaks for N_2O_4 and NO_2 are below 1800 cm^{-1} , which is outside the range of detection for the current experimental set-up; N_2O_4 does absorb above 1800 cm^{-1} , but these are weak fundamentals or combination bands, some of which overlap with the O–H stretching region [85].

1.4 Chapter 1 References

- [1] Angell, C. A. *Annu. Rev. Phys. Chem.* **2004**, *55*, 559–583.
- [2] Hama, T.; Watanabe, N. *Chem. Rev.* **2013**, *113*, 8783–839.
- [3] Smoluchowski, R. *Science* **1978**, *201*, 809–811.
- [4] Draine, B. T. *Annu. Rev. Astron. Astrophys.* **2003**, *41*, 241–289.
- [5] Lisse, C.; Bar-Nun, A.; Laufer, D.; Belton, M.; Harris, W.; Hsieh, H.; Jewitt, D. In *Sci. Sol. Syst. Ices*; Gudipati, M. S.; Castillo-Rogez, J., Eds.; Astrophysics and Space Science Library, Vol. 356; Springer New York: New York, NY, 2013; Chapter 13, pp 455–485.
- [6] Jenniskens, P.; Blake, D. F. *Science* **1994**, *265*, 753–756.
- [7] Madey, T. E.; Johnson, R. E.; Orlando, T. M. *Surf. Sci.* **2002**, *500*, 838–858.
- [8] Burke, D. J.; Brown, W. A. *Phys. Chem. Chem. Phys.* **2010**, *12*, 5947–5969.
- [9] Falenty, A.; Hansen, T. C.; Kuhs, W. F. *Nature* **2014**, *516*, 231–233.
- [10] Salzmann, C. G.; Radaelli, P. G.; Mayer, E.; Finney, J. L. *Phys. Rev. Lett.* **2009**, *103*, 105701(4).
- [11] Mastrapa, R. M. E.; Grundy, W. M.; Gudipati, M. S. In *Sci. Sol. Syst. Ices*; Gudipati, M. S.; Castillo-Rogez, J., Eds.; Astrophysics and Space Science Library, Vol. 356; Springer New York: New York, NY, 2013; Chapter 11, pp 371–408.
- [12] Andersson, O.; Inaba, A. *Phys. Chem. Chem. Phys.* **2005**, *7*, 1441–1449.
- [13] Johari, G. P.; Hallbrucker, A.; Mayer, E. *Nature* **1987**, *330*, 552–553.
- [14] May, R. A.; Smith, R. S.; Kay, B. D. *J. Phys. Chem. Lett.* **2012**, *3*, 327–331.
- [15] Kohl, I.; Mayer, E.; Hallbrucker, A. *Phys. Chem. Chem. Phys.* **2000**, *2*, 1579–1586.
- [16] Narten, A. H.; Venkatesh, C. G.; Rice, S. A. *J. Chem. Phys.* **1976**, *64*, 1106–1121.
- [17] Dohnálek, Z.; Kimmel, G. A.; Ayotte, P.; Smith, R. S.; Kay, B. D. *J. Chem. Phys.* **2003**, *118*, 364–372.
- [18] Parent, P.; Laffon, C.; Mangeney, C.; Bournel, F.; Tronc, M. *J. Chem. Phys.* **2002**, *117*, 10842–10851.
- [19] Johari, G. P.; Hallbrucker, A.; Mayer, E. *J. Chem. Phys.* **1992**, *97*, 5851–5855.

- [20] Mitterdorfer, C.; Bauer, M.; Youngs, T. G. A.; Bowron, D. T.; Hill, C. R.; Fraser, H. J.; Finney, J. L.; Loerting, T. *Phys. Chem. Chem. Phys.* **2014**, *16*, 16013–16020.
- [21] Stevenson, K. P.; Kimmel, G. A.; Dohnálek, Z.; Smith, R. S.; Kay, B. D. *Science* **1999**, *283*, 1505–1507.
- [22] Jenniskens, P.; Banham, S. F.; Blake, D. F.; McCoustra, M. R. S. *J. Chem. Phys.* **1997**, *107*, 1232–1241.
- [23] Laufer, D.; Bar-Nun, A.; Pat-El, I.; Jacovi, R. *Icarus* **2013**, *222*, 73–80.
- [24] Newman, S. F.; Buratti, B. J.; Brown, R. H.; Jaumann, R.; Bauer, J.; Momary, T. *Icarus* **2008**, *193*, 397–406.
- [25] Goguen, J. D.; Buratti, B. J.; Brown, R. H.; Clark, R. N.; Nicholson, P. D.; Hedman, M. M.; Howell, R. R.; Sotin, C.; Cruikshank, D. P.; Baines, K. H.; Lawrence, K. J.; Spencer, J. R.; Blackburn, D. G. *Icarus* **2013**, *226*, 1128–1137.
- [26] Spencer, J. R.; Pearl, J. C.; Segura, M.; Flasar, F. M.; Mamoutkine, A.; Romani, P.; Buratti, B. J.; Hendrix, A. R.; Spilker, L. J.; Lopes, R. M. C. *Science* **2006**, *311*, 1401–1405.
- [27] Porco, C. C.; et al. *Science* **2006**, *311*, 1393–1401.
- [28] Hansen, C. J.; Esposito, L. W.; Stewart, A. I. F.; Meinke, B.; Wallis, B.; Colwell, J. E.; Hendrix, A. R.; Larsen, K.; Pryor, W.; Tian, F. *Nature* **2008**, *456*, 477–479.
- [29] Porco, C. C.; DiNino, D.; Nimmo, F. *Astron. J.* **2014**, *148*, 45(24).
- [30] Hansen, C. J.; Shemansky, D. E.; Esposito, L. W.; Stewart, A. I. F.; Lewis, B. R.; Colwell, J. E.; Hendrix, A. R.; West, R. A.; Waite, Jr., J. H.; Teolis, B. D.; Magee, B. A. *Geophys. Res. Lett.* **2011**, *38*, L11202(5).
- [31] Spitale, J. N.; Hurford, T. A.; Rhoden, A. R.; Berkson, E. E.; Platts, S. S. *Nature* **2015**, *521*, 57–60.
- [32] Waite, Jr., J. H.; et al. *Nature* **2009**, *460*, 487–490.
- [33] Iess, L.; Stevenson, D. J.; Parisi, M.; Hemingway, D.; Jacobson, R. A.; Lunine, J. I.; Nimmo, F.; Armstrong, J. W.; Asmar, S. W.; Ducci, M.; Tortora, P. *Science* **2014**, *344*, 78–80.
- [34] Wang, H.; Bell, R. C.; Iedema, M. J.; Tsekouras, A. A.; Cowin, J. P. *Astrophys. J.* **2005**, *620*, 1027–1032.
- [35] van Dishoeck, E. F. *Faraday Discuss.* **2014**, *168*, 9–47.

- [36] Ehrenfreund, P.; Dartois, E.; Demyk, K.; d'Hendecourt, L. *Astron. Astrophys.* **1998**, *20*, L17–L20.
- [37] Ehrenfreund, P.; Charnley, S. B. *Annu. Rev. Astron. Astrophys.* **2000**, *38*, 427–483.
- [38] van Dishoeck, E. F.; Herbst, E.; Neufeld, D. A. *Chem. Rev.* **2013**, *113*, 9043–9085.
- [39] Gibb, E. L.; Whittet, D. C. B.; Boogert, A. C. A.; Tielens, A. G. G. M. *Astrophys. J. Suppl. Ser.* **2004**, *151*, 35–73.
- [40] Cuppen, H. M.; Herbst, E. *Astrophys. J.* **2007**, *668*, 294–309.
- [41] d'Hendecourt, L. B.; Allamandola, L. J.; Baas, F.; Greenberg, J. M. *Astron. Astrophys.* **1982**, *109*, L12–L14.
- [42] Ossenkopf, V. *Astron. Astrophys.* **1993**, *280*, 617–646.
- [43] Jenniskens, P.; Blake, D. F. *Astrophys. J.* **1996**, *473*, 1104–1113.
- [44] Laufer, D.; Kochavi, E.; Bar-Nun, A. *Phys. Rev. B* **1987**, *36*, 9219–9227.
- [45] Bar-Nun, A.; Dror, J.; Kochavi, E.; Laufer, D. *Phys. Rev. B* **1987**, *35*, 2427–2435.
- [46] Bar-Nun, A.; Kleinfeld, I.; Kochavi, E. *Phys. Rev. B* **1988**, *38*, 7749–7754.
- [47] Bar-Nun, A.; Herman, G.; Laufer, D.; Rappaport, M. L. *Icarus* **1985**, *63*, 317–332.
- [48] Hudson, R. L.; Donn, B. *Icarus* **1991**, *94*, 326–332.
- [49] Mayer, E.; Pletzer, R. *Nature* **1986**, *319*, 298–301.
- [50] Gudipati, M. S.; Allamandola, L. J. *Astrophys. J.* **2004**, *615*, L177–L180.
- [51] Gudipati, M. S.; Allamandola, L. J. *Astrophys. J.* **2006**, *638*, 286–292.
- [52] Giaque, W. F.; Kemp, J. D. *J. Chem. Phys.* **1938**, *6*, 40–51.
- [53] Kvick, A.; McMullan, R. K.; Newton, M. D. *J. Chem. Phys.* **1982**, *76*, 3754–3761.
- [54] Kohata, K.; Fukuyama, T.; Kuchitsu, K. *J. Phys. Chem.* **1982**, *86*, 602–606.
- [55] Schlegel, H. B.; Skancke, A. *J. Am. Chem. Soc.* **1992**, *115*, 7465–7471.
- [56] Bauschlicher, Jr, C. W.; Komornicki, A.; Roos, B. *J. Am. Chem. Soc.* **1983**, *105*, 745–748.
- [57] Givan, A.; Loewenschuss, A. *J. Chem. Phys.* **1990**, *93*, 7592–7600.

- [58] Koch, T. G.; Horn, A. B.; Chesters, M. A.; McCoustra, M. R. S.; Sodeau, J. R. *J. Phys. Chem.* **1995**, *99*, 8362–8367.
- [59] Merienne, M. F.; Jenouvrier, A.; Coquart, B.; Lux, J. P. *J. Atmos. Chem.* **1995**, *20*, 281–297.
- [60] Yabushita, A.; Inoue, Y.; Senga, T.; Kawasaki, M. *J. Phys. Chem. A* **2004**, *108*, 438–446.
- [61] Gálvez, O.; Maté, B.; Herrero, V. J.; Escribano, R. *Icarus* **2008**, *197*, 599–605.
- [62] Thrower, J. D.; Collings, M. P.; Rutten, F. J. M.; McCoustra, M. R. S. *J. Chem. Phys.* **2009**, *131*, 244711.
- [63] Yabushita, A.; Hama, T.; Iida, D.; Kawanaka, N.; Kawasaki, M.; Watanabe, N.; Ashfold, M. N. R.; Looock, H.-P. *J. Chem. Phys.* **2008**, *129*, 044501.
- [64] Collings, M. P.; Anderson, M. A.; Chen, R.; Dever, J. W.; Viti, S.; Williams, D. A.; McCoustra, M. R. S. *Mon. Not. R. Astron. Soc.* **2004**, *354*, 1133–1140.
- [65] May, R. A.; Smith, R. S.; Kay, B. D. *J. Chem. Phys.* **2013**, *138*, 104501(11).
- [66] May, R. A.; Smith, R. S.; Kay, B. D.; Alan May, R.; Scott Smith, R.; Kay, B. D. *J. Chem. Phys.* **2013**, *138*, 104502(11).
- [67] Malyk, S.; Kumi, G.; Reisler, H.; Wittig, C. *J. Phys. Chem. A* **2007**, *111*, 13365–13370.
- [68] Rebolledo-Mayoral, O. R.; Stomberg, J.; McKean, S.; Reisler, H.; Wittig, C. *J. Phys. Chem. C* **2012**, *116*, 563–569.
- [69] Bernstein, M. P.; Sandford, S. A.; Allamandola, L. J.; Gillette, J. S.; Clemett, S. J.; Zare, R. N. *Science* **1999**, *283*, 1135–1138.
- [70] Minissale, M.; Congiu, E.; Baouche, S.; Chaabouni, H.; Moudens, A.; Dulieu, F.; Manicó, G.; Pirronello, V. *Chem. Phys. Lett.* **2013**, *565*, 52–55.
- [71] Miotello, A.; Kelly, R. *Appl. Phys. A* **1999**, *69*, S67–S73.
- [72] Zhigilei, L. V.; Kodali, P. B. S.; Garrison, B. J. *J. Phys. Chem. B* **1998**, *102*, 2845–2853.
- [73] Krasnopoler, A.; George, S. M. *J. Phys. Chem. B* **1998**, *102*, 788–794.
- [74] Anisimov, S. I.; Luk'Yanchuk, B. S.; Luches, A. *Appl. Surf. Sci.* **1996**, *96-98*, 24–32.
- [75] Anisimov, S. I.; Bäuerle, D.; Luk'Yanchuk, B. S. *Phys. Rev. B* **1993**, *48*, 12076–12081.

- [76] Schou, J. R.; Amaruso, S.; Lunney, J. G. In *Laser Ablation and its Applications*; Phipps, C., Ed.; Optical Sciences; Springer: Santa Fe, New Mexico, 2007; Chapter 4, pp 67–91.
- [77] Wiley, W. C.; McLaren, I. H. *Rev. Sci. Instrum.* **1955**, *26*, 1150–1157.
- [78] Mamyryn, B. A. *Int. J. Mass Spectrom.* **2001**, *206*, 251–266.
- [79] Dunning, W. J. *Q. Rev. Chem. Soc.* **1955**, *9*, 23–50.
- [80] McLafferty, F. W. *Anal. Chem.* **1956**, *28*, 306–316.
- [81] Bergren, M. S.; Schuh, D.; Sceats, M. G.; Rice, S. A. *J. Chem. Phys.* **1978**, *69*, 3477–3482.
- [82] Mayer, E. *J. Phys. Chem.* **1985**, *89*, 3474–3477.
- [83] Cholette, F.; Zubkov, T.; Smith, R. S.; Dohnálek, Z.; Kay, B. D.; Ayotte, P. *J. Phys. Chem. B* **2009**, *113*, 4131–4140.
- [84] Manca, C.; Martin, C.; Roubin, P. *Chem. Phys.* **2004**, *300*, 53–62.
- [85] Roux, J. A.; Wood, B. E. *J. Opt. Soc. Am.* **1983**, *73*, 1181–1188.

CHAPTER 2: EXPERIMENTAL SET-UP

This chapter describes the experimental apparatus, while the next chapter focuses on the processes of conducting experiments. The intent is to give a full picture of how the components fit together and how they function individually before relaying how they collectively are used to conduct experiments. The experimental apparatus is designed to accommodate four key processes: the deposition of gases onto an MgO substrate held at 100 K; the irradiation of the resulting film with laser pulses to desorb a plume of material; the detection of plume components as a function of time via rapid collection of time-of-flight mass spectra; and the detection of changes in the irradiated area of the film via transmission Fourier-transform infrared spectroscopy. To allow all of these, a three-tier chamber with an assortment of ports is used, which includes: a gas dosing system, a time-of-flight mass spectrometer, a Fourier-transform infrared spectrometer, and entry of the laser beam into the chamber (Fig. 2.1). The MgO surface on which the experiment is conducted is mounted on a manipulable cold finger with a liquid nitrogen reservoir. The set-up will be described starting with the laser and optics, following the beam path to the chamber. The chamber will be described from its bottom upward, and then down the cold finger to the sample holder and substrate. Lastly, the detection instruments (Fourier-transform infrared spectrometer and time-of-flight mass spectrometer) and their integration with the rest of the apparatus will be addressed.

2.1 Laser and Optics

A pulsed (10 Hz) Nd:YAG laser [Continuum Powerlite 9010] is used to generate 10-ns (full-width, third maximum) pulses of 266-nm radiation. The fundamental frequency (1064 nm) is generated and guided to a second- and fourth-harmonic

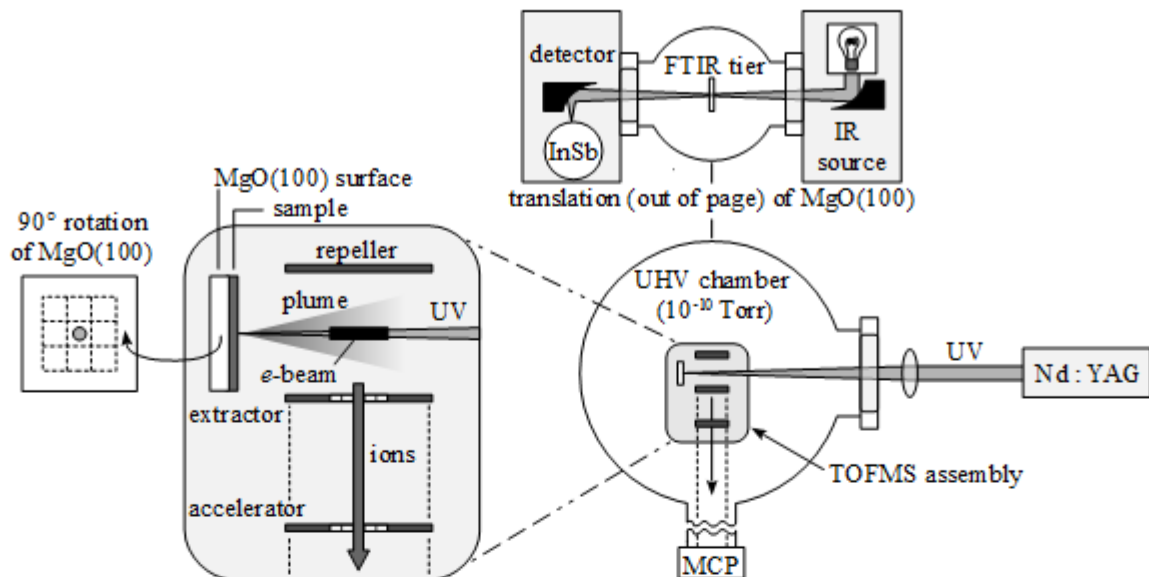


Figure 2.1: A simplified schematic of the experiment. An ultra-high vacuum chamber is equipped with a time-of-flight mass spectrometer and Fourier-transform infrared spectrometer; the arrangement of the time-of-flight mass spectrometer is indicated schematically. UV radiation excites the sample at normal incidence causing material to enter the gas phase. Ions are extracted at a repetition rate of 100 kHz. The black rectangle labeled *e*-beam indicates the portion of the ionized region that is extracted through the mesh apertures that lie below it. Samples deposited on the MgO(100) surface are irradiated in nine areas, indicated on the left, to achieve signal averaging while maintaining single-pulse conditions. For Fourier-transform infrared studies, the focusing lens is removed and a larger area is irradiated. The surface is then translated to the upper tier of the chamber; infrared light is focused on the surface with a parabolic mirror and then focused once more onto an InSb detector.

generator [SpectraPhysics QuantaRay, HG-2] external to the laser. The temperature-controlled harmonic generator crystals produce 266-nm radiation, but also transmit unconverted 1064-nm and 532-nm radiation. Turning mirrors guide the beam down the optics table. All mirrors used have a broadband (240–390 nm) dielectric coating [CVI Laser Optics]. A CaF₂ prism is used to separate the beam into its component wavelengths; residual radiation is collected in a beam dump and the isolated 266-nm radiation is guided through the remaining bench optics.

After the 266-nm beam is isolated, it is directed through a Glan-Thompson polarizer. The N₂O₄ and ASW films are isotropic in the bulk, so the polarization of the beam is unimportant; the polarizer simply functions as a convenient way to modulate the average energy of the beam by acting as a variable-percentage beam

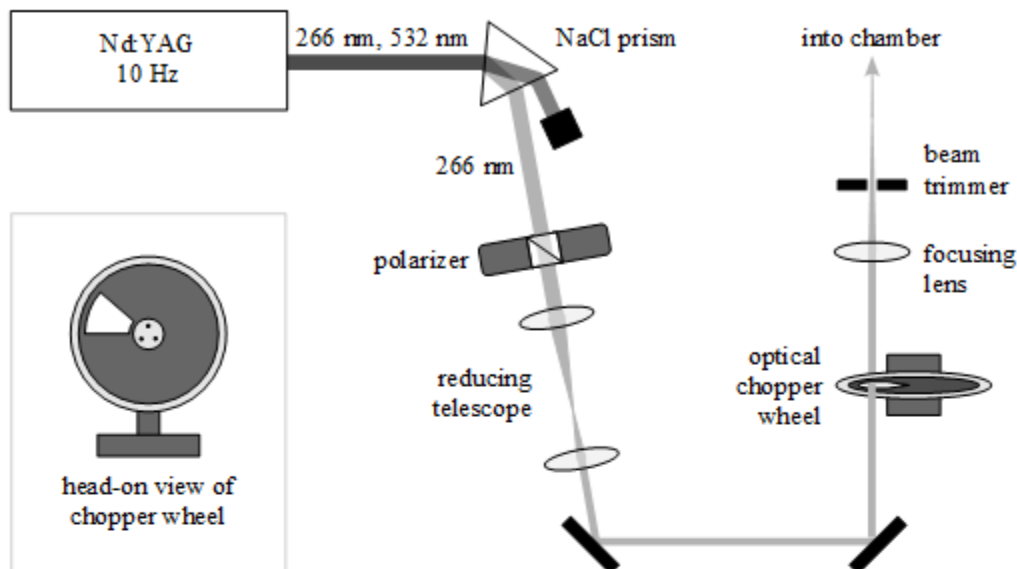


Figure 2.2: A diagram of the bench optics, with several steering mirrors omitted for clarity. The light that exits the laser is mostly 266 nm, with some residual 532 and 1064 nm. The small amount of 1064 nm is dumped at the two mirrors (not shown) that steer the beam to the prism. The prism then separates the 266-nm and 532-nm light. The 266-nm beam enters a polarizer, which is used to attenuate the beam if needed. The two lenses that make up the reducing telescope decrease the beam size. The optical chopper wheel cuts the laser pulse frequency from 10 Hz to 1 Hz. The focusing lens is removed for experiments that include Fourier-transform infrared spectroscopy. The beam trimmer is used to remove any halo of scattered light before the beam enters the chamber.

splitter. The beam is collimated and reduced in diameter by two plano-convex lenses [CVI] with an anti-reflection dielectric coating specific for 266-nm radiation. Their focal lengths are 15 and 5 cm, giving an ideal beam reduction factor of three. Aside from collimating the beam, the diameter reduction is such that the beam will irradiate only the MgO surface, and not the substrate holder. This is important when the beam is not focused onto the surface, as for experiments that include Fourier-transform infrared spectroscopy.

A chopper wheel [ThorLabs, MC1000 Optical Chopper] is controlled by a pulse generator which provides a 5-V TTL pulse at 100 Hz; its control box has a feedback that maintains the wheel rotation at precisely 1 Hz. The Teflon chopper wheel has an aperture (see Fig. 2.2) that temporally corresponds to 10 ms, reducing the laser repetition rate from 10 Hz to 1 Hz. Even at 10 Hz, one can visually distinguish individual pulses, and it is trivial to ensure that the laser pulse is not clipped. When

reduced to 1 Hz, the number of pulses incident on the sample can be easily counted.

Before the laser pulse enters the chamber a UV-grade, 40-cm biconvex lens focuses the beam from a ~ 2 -mm diameter to ~ 0.3 mm at the MgO surface. Lastly, between the focusing lens and the chamber window, an iris is used both to aid in aligning the laser to the MgO surface and to trim the beam. The main beam is not trimmed; rather, the iris is used to block any halo of scattered light that might hit the copper substrate holder or the time-of-flight plates, desorbing materials from other than the target source. The beam is guided to pass through the ionization region of the time-of-flight mass spectrometer and onto the MgO substrate at normal incidence.

2.2 Main Structure of Chamber

The ultra-high vacuum chamber consists of three tiers, designated the “bottom,” “middle” and “top” tiers (see Fig. 2.3). The bottom and middle tiers are one continuous segment of the chamber, also referred to as the “main chamber,” and it is the positions of the ports on the chamber that distinguish the tiers. These two tiers are where gas dosing, laser irradiation, and time-of-flight experiments are conducted. The top tier is the level where transmission Fourier-transform infrared spectroscopy is conducted. The top tier can be isolated from the rest of the chamber by a gate valve situated between the top and middle tiers. This structure was designed and created by previous graduate students; the arrangement of its components has been adapted for these experiments.

The ports on the stainless-steel chamber have conflat flanges sealed with copper gaskets. All experimentally relevant windows on the chamber are made of CaF_2 . The chamber is evacuated via a turbomolecular pump [Leybold Turbovac 600] on the middle tier (not shown in Fig. 2.3). A roughing pump backs the turbomolecular pump and also directly pumps the θ manipulator to compensate for its less effective

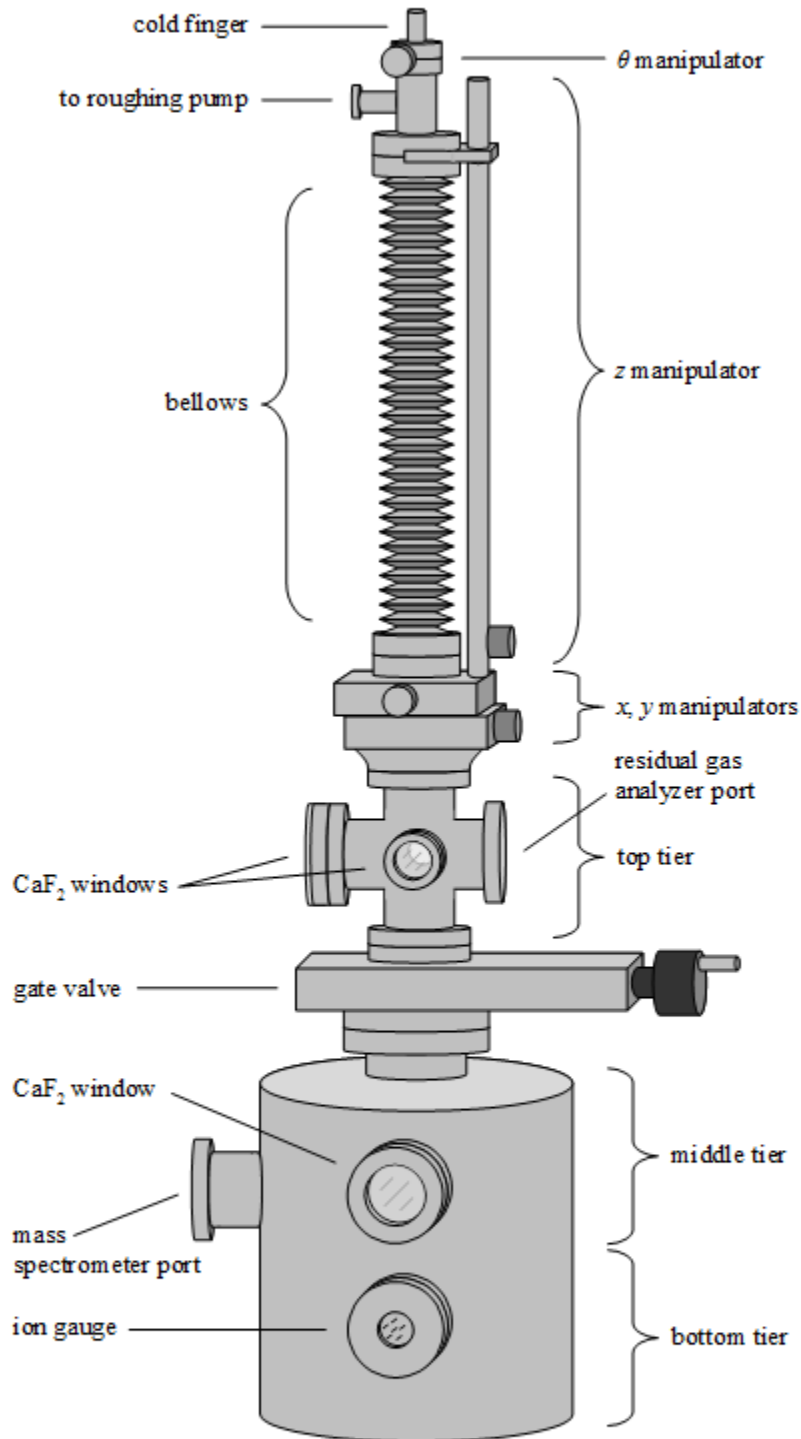


Figure 2.3: An external view of the entire chamber. The small CaF_2 window on the top tier has an identical port on the opposite side of the chamber for transmission of the infrared beam. The gate valve allows separation of the top tier from the middle and bottom tiers. The middle and bottom tiers have no separation between them, and are together referred to as the “main chamber.” For clarity, only some of the ports on the main chamber are shown. The ports shown are intended to aid in visualizing the orientation of the chamber as a whole with respect to cross-section diagrams of the individual tiers.

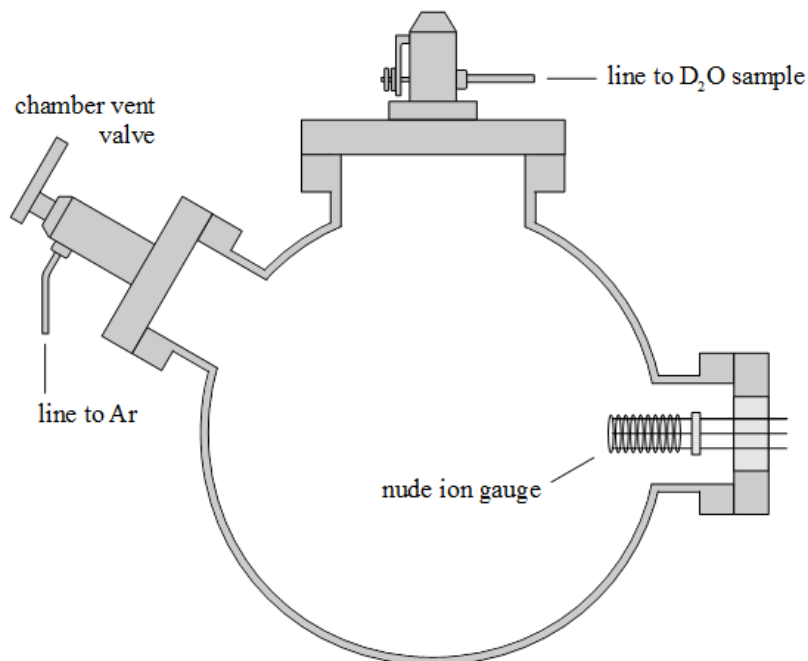


Figure 2.4: A diagram of the bottom tier of the ultra-high vacuum chamber. Ports on the chamber that are not used in this experiment have been omitted. The chamber vent valve is used to bring the chamber to atmospheric pressure with argon gas when the chamber needs to be opened for maintenance. A precision leak valve is connected to a sample of D_2O . The nude ion gauge is used to measure the total pressure of the chamber when fully evacuated or when introducing a set pressure of gas via a precision leak valve.

seal. The chamber is routinely pumped down to pressures on the order of 10^{-10} Torr when the surface is at 100 K. If the base pressure is higher than preferred, such as after opening the chamber for maintenance or after numerous experiments conducted close together, the chamber is heated by either the heat lamp in the middle tier of the chamber (Sec. 2.2.2) or by heating tapes that are wrapped around the chamber.

2.2.1 Bottom tier

The bottom tier of the chamber (Fig. 2.4) houses the chamber vent valve, a precision leak valve, and a nude ion gauge. The vent valve is used to bring the chamber up to atmospheric pressure so that it can be opened for maintenance. The valve separates the body of the chamber from a line connected directly to a tank of argon gas [Gilmore

Liquid Air, 99.999% purity]. When argon is flowing, a pinhole near its connection to the valve provides an outlet to avoid pressurizing the chamber; it also provides a way to ensure that a positive pressure of argon is maintained as the vent valve is slowly opened, preventing air from entering the chamber.

The precision gas leak valve [MDC Vacuum Products, ULV-150] is used to introduce de-gassed D₂O from a glass vial which is adapted to the standard gas line fittings. When not in use, a stopcock closes off the sample from the leak valve and the line to the leak valve is instead opened to a vacuum line; this prevents contamination and reduces the pressure differential across the leak valve.

The nude ion gauge measures the total pressure in the chamber when it is below 10⁻⁴ Torr. The ion gauge is connected, via ultra-high vacuum-rated electrical feed-throughs, to a digital controller [Granville Phillips, 300 Ion Gauge Controller] which provides an input current and displays the pressure reading. The ion gauge is used to set the dosing pressures for gas introduced via the precision leak valves.

2.2.2 Middle tier

The middle tier is used for sample preparation, laser irradiation, and time-of-flight mass spectrometry. A precision leak valve [MDC Vacuum Products, ULV-150] for introducing water is connected to a glass vial in the same manner as on the bottom tier. Another leak valve [Duniway] connects to the NO₂ sample, which is kept in a similar vial. The NO₂ gas, however, cannot be introduced into the chamber just by leaking in the vapor as with the other components. NO₂ is a strong oxidizer and it readily reacts with metal surfaces to produce a metal-oxide coating and NO gas; this process is called passivation. The leak valve and the stainless steel gas line to the NO₂ gas acquire an oxide layer that prevent further reaction. These components are frequently in contact with a relatively large amount of NO₂ gas. The chamber, on the

other hand, has orders of magnitude more exposed surface area than the leak valve and gas line do. It is unfeasible to passivate the entire chamber; however, it is also unacceptable to have much of the introduced gas degrade to NO.

To solve this problem, a directed doser was designed and implemented specifically for these experiments (Fig. 2.6). The doser directs NO₂ towards the cooled MgO surface, instead of allowing multiple collisions with the chamber walls to occur before it is incident on the surface – by which point it will inevitably convert to NO. The doser design allows for introduction of gas by back-filling the chamber and monitoring the pressure, while also minimizes collisions with metal surfaces.

The doser (Fig. 2.6) is constructed from a 23-cm long glass tube with an inner diameter of 7.5 mm that is mounted to the leak valve via a machined metal adapter. The glass tube fits fairly snugly into the adapter, which provides a mode of attachment to the leak valve and some level of support so it will not be as fragile at the connection point. As added insurance, the two pieces are also glued together [Aremco Products, Ceramabond 835-M]. The metal adapter has three untapped holes in its base, and three tapped holes were drilled into the face plate of the leak valve. When the directed doser is mounted to the leak valve, there is no seal between them; because it is not functioning as a “nozzle,” this is of no concern. The MgO surface need only be turned to face the doser. The end of the glass tube is about 4 cm from the surface, which is far enough to prevent an angular distribution of thickness across the sample surface [1]. It does deposit more material than background dosing; the amount of material deposited has been calibrated using Fourier-transform infrared spectroscopy, as detailed in Section 3.2.2.

For time-of-flight mass spectrometry and laser irradiation experiments, the MgO surface is positioned parallel to the time-of-flight mass spectrometer and normal to the laser beam path. The laser pulse enters the chamber through a CaF₂ window and passes between two plates of the time-of-flight mass spectrometer and is then incident

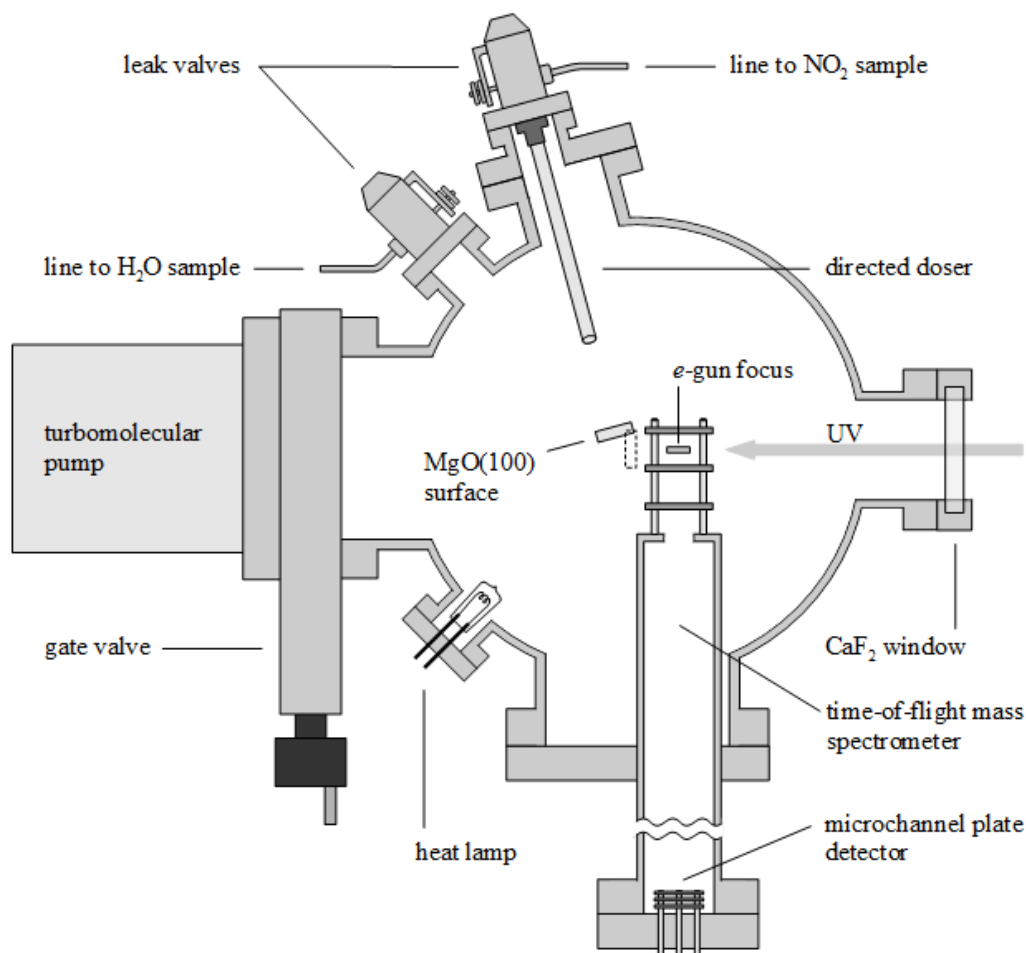


Figure 2.5: A diagram of the middle tier of the ultra-high vacuum chamber. Ports on the chamber that are not used in this experiment are omitted for clarity. The MgO(100) surface is shown in the position used for directed dosing of NO₂; the dashed outline indicates the position of the surface during irradiation and time-of-flight mass spectrometry experiments. The rectangle showing the *e*-gun focus is the ionization region of the time-of-flight mass spectrometer. UV radiation (gray arrow) enters the chamber via the CaF₂ window with normal incidence to both the window and the surface. The time-of-flight mass spectrometer and the microchannel plate detector will be discussed in detail in the following chapter.



Figure 2.6: A diagram of the directed doser. The machined metal adapter (shown in cross-section) is mounted to the opening of the leak valve (see Fig. 2.5) by three screws, fed through untapped holes in the adapter into holes tapped into the valve. The glass dosing tube (23-cm long, 7.5-mm inner diameter) fits snugly into the adapter and is secured with glue.

upon the surface. When the pulsed radiation induces the desorption of a plume of material from the surface, the plume passes through the ionizing region of the time of flight and the resulting ions are accelerated towards the microchannel plate detector. Details of how the time-of-flight mass spectrometer operates is discussed in Section 2.5. Lastly, the middle tier houses both the previously discussed turbomolecular pump, which can be closed off to the chamber via a gate valve, and the heat lamp [OSRAM, 650 W].

2.2.3 Top tier

The top tier of the chamber provides access to the sample holder through the port opposite the residual gas analyzer (Fig. 2.7). When maintenance is necessary, the chamber is filled with argon (described in Sec. 2.2.1) and the gate valve between the top tier and the main chamber is closed. Thus, the smallest possible portion of the chamber is fully exposed to atmosphere. This is considered preferable to providing a positive-pressure flow of argon out of this port because it is often necessary to have the port open for prolonged periods of time.

The top tier houses the residual gas analyzer [Stanford Research Systems, residual gas analyzer 300], which can be used to monitor individual molecular species present in the evacuated chamber, as opposed to the total pressure measured by the ion gauge. It is used to verify the purity of gases introduced via the precision leak valves; for example, to ensure that water vapor introduced into the chamber does not contain a significant amount of air. This provides consistency in sample dosing. A nude ion gauge and a residual gas analyzer will inherently give slightly different pressure readings. As such, the ion gauge is used to determine the pressure of gas introduced into the chamber; the residual gas analyzer is used only diagnostically to check for chamber leaks, to monitor the sample purity, and to calibrate deposition pressures

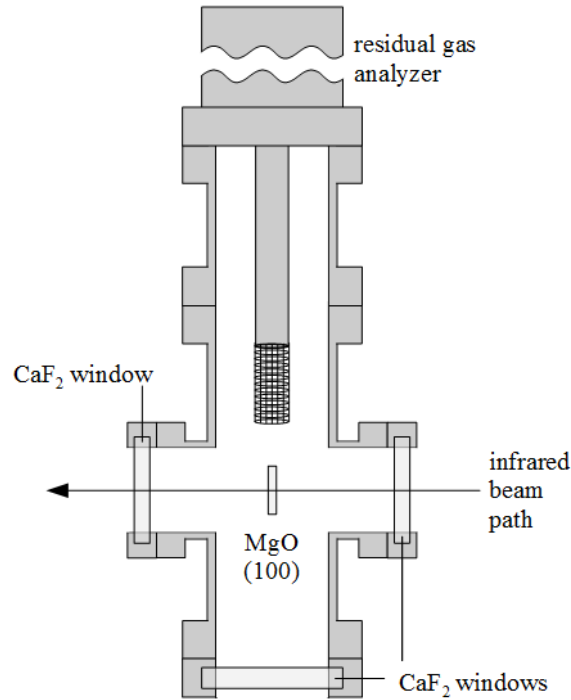


Figure 2.7: A diagram of the top tier of the ultra-high vacuum chamber. The MgO(100) surface is shown in the position used for Fourier-transform infrared spectroscopy experiments, although the Fourier-transform infrared spectrometer and its set-up is omitted. The CaF₂ window at the bottom of the diagram is used for visual inspection of the surface without bringing the chamber to pressure, and is used as the main access port for maintenance and installation of the sample holder. The residual gas analyzer is used to monitor the purity of samples and check for chamber leaks.

(see Sec. 3.2.2). The top tier of the chamber is also used for transmission Fourier-transform infrared spectroscopy; the details concerning its set-up will be given in Section 2.5. In brief, the infrared beam is guided through a CaF₂ window, through the center of the MgO substrate, then out the other side of the chamber and onto an InSb detector.

2.3 Manipulators and Cold Finger

The manipulators and the cold finger together act as the connection between the body of the chamber and the sample holder. The manipulator [VG Sienta, Omniax] is made up of x , y , z , and θ manipulators (Fig. 2.3); the cold finger, designed and manufactured by McAllistar Technical Services, comprises a liquid nitrogen reservoir,

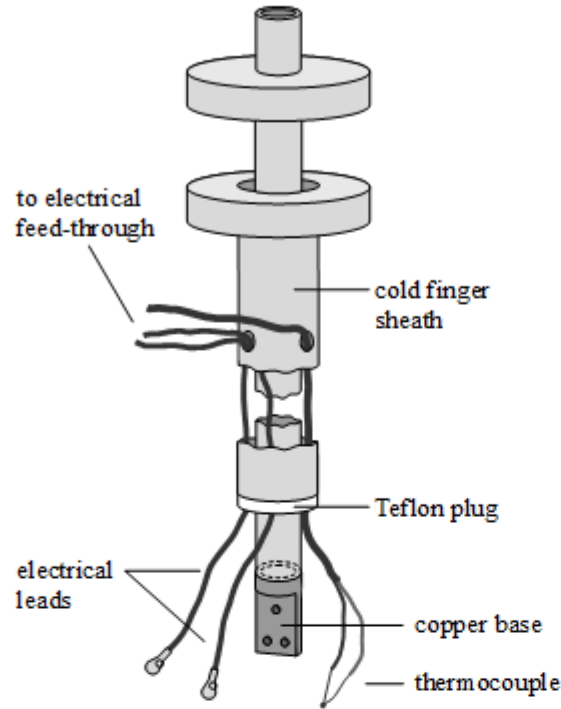


Figure 2.8: A diagram of the cold finger. In this diagram the flange connection of the liquid nitrogen reservoir is pulled away from flange connection of the cold finger sheath, and only the top and bottom of the cold finger are shown. The liquid nitrogen reservoir is capped by a copper base, to which the sample holder is mounted. Wires for a thermocouple and two electrical leads are fed into the space between the sheath and cold finger. A Teflon plug holds wires in position near the base of the cold finger.

the mount for the sample holder, and electrical connections (Fig. 2.8). A bellows connects the ends of the z -manipulator and surrounds the cold finger.

The x and y manipulators are translation stages that move the sample parallel and perpendicular to the laser beam. Both manipulators have a range of ± 12.5 mm from the center of the chamber. The translation stages are moved by a vernier scale micrometer with a precision of 0.005 mm. The z manipulator moves the cold finger up and down along its axis. A small motor is attached to the gears that raise and lower the cold finger to facilitate translation. The θ manipulator, just below where the top of the cold finger is attached, rotates the cold finger around its axis.

The liquid nitrogen-cooled cold finger is a stainless steel tube with a copper base that has been silver brazed to the lower end (Fig. 2.8). The liquid nitrogen is in direct contact with the copper base, which has three untapped holes to mount the sample

holder to it. Wires for a K-type thermocouple and two electrical leads are fed into the space between the cold finger and its sheath, which protects the wires from catching on chamber components. A Teflon plug holds wires in position near the base of the cold finger, preventing the wires from tangling. It also helps stabilize the reservoir so it does not wobble inside the sheath. The cold finger and its connections were designed and created by previous graduate students.

2.4 Sample Holder

The sample holder is made up of two copper blocks, a resistive heater, and the substrate holder (Fig. 2.9 and 2.10). It is mounted to the cold finger base by three screws, which fit through the untapped holes in the cold finger base and the sample holder's copper blocks. The screws have a ceramic hat washer [McAllister Technical Services, size 4-40] on each end to electrically isolate them from the cold finger base and the sample holder. The two copper blocks are electrically isolated from one another by a ceramic spacer [USC machine shop, dimensions in reference [2]].

A 1-mm thick sapphire disk [ESCO Products] is placed between the cold finger base and the copper blocks of the sample holder. This electrically isolates the sample holder from the cold finger base without isolating it thermally. Sapphire can act as a thermal "switch" because it has a high thermal conductivity at low temperatures (~ 10 W/m·K at 100 K) but is a poor thermal conductor at high temperatures (~ 0.3 W/m·K at 400 K) [3].

2.4.1 Substrate holder

The substrate holder secures the MgO surface and provides thermal contact between the surface and the copper blocks of the sample holder. It is constructed

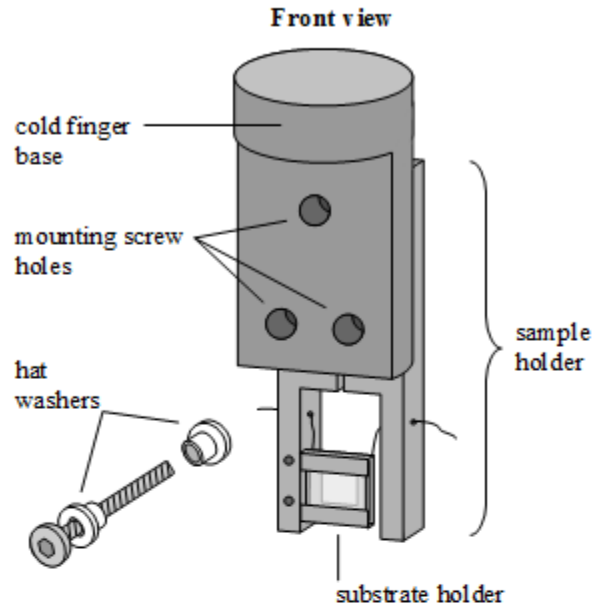


Figure 2.9: A front view of the sample holder, in the position in which it is mounted to the cold finger base. The mounting screws have a ceramic hat washer on each end to electrically isolate them from the unthreaded mounting screw holes on the cold finger base and on the sample holder. The term “sample holder” encompasses the entire entity mounted on the cold finger base, including the substrate holder.

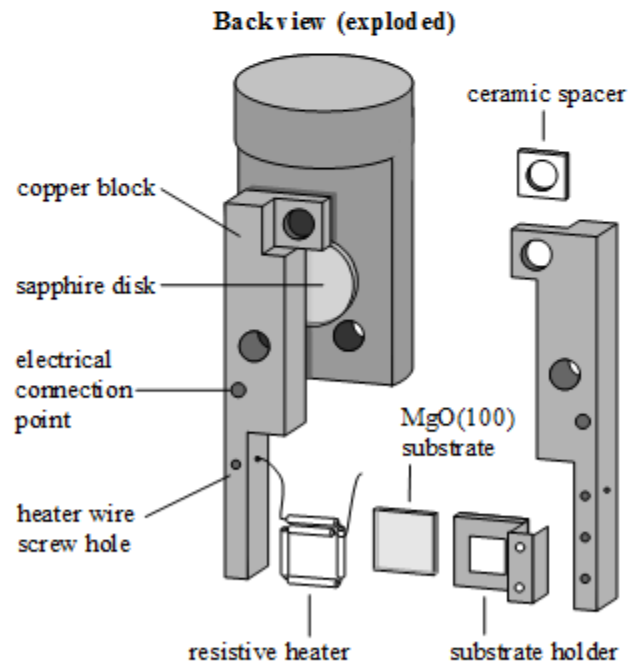


Figure 2.10: An exploded diagram of the sample holder, viewed from the back. The two copper blocks are electrically isolated from one another by a ceramic spacer. The sapphire disk electrically, but not thermally, isolates the sample holder from the cold finger base. The substrate holder clamps around the substrate; the resistive heater is glued to the back of it. The heater wires feed through holes in the copper blocks; the screw holes perpendicular to the wire holes secure the wires. Electrical leads are screwed into the electrical connection points to provide voltage to the heater.

from 0.010”-thick copper foil [ESPI Metals, 3N purity], cut from a single piece of foil. The substrate is centered over a square (6×6 mm) aperture in the foil to accommodate transmission Fourier-transform infrared spectroscopy. Tabs at the top and bottom are folded over the edges of the substrate and crimped snugly to the surface. A longer tab of foil to the side of the substrate folds back and around the lower portion of the sample holder. This tab also fits snugly, and two holes allow the surface holder to be mounted to the sample holder using screws.

The substrate holder is only in thermal contact with one of the copper blocks. Care must be taken to ensure that a temperature gradient does not exist across the MgO surface – a problem that has occurred in the past. At the time, the arm that attaches to the sample holder’s copper block was narrower (5 mm). Widening the arm to 1 cm helped maximize the thermal contact on the left (attached) side of the MgO substrate. Evenly and firmly crimping the surface into its holder is essential. The temperature of the surface is monitored by a K-type thermocouple, which is glued [Aremco Products, Ceramabond 835-M] to the surface of the MgO.

2.4.2 Resistive heater

The resistive heater is constructed from tantalum wire [ESPI Metals, 0.015” diameter, 3N8 purity]. The wire is threaded through segments of ceramic tube [Omega, ORX-020132] and bent to form a square loop which fits on the back of the substrate holder and around the aperture. The heater is then glued [Aremco Products, Ceramabond 835-M] to the copper substrate holder, making sure that bare wire does not make contact with the surface or short itself at the crossing point of the loop. The ends of the wires are fed through holes in each of the copper blocks and secured with screws. The only electrical connection between the two copper blocks, then, is through the resistive heater. The two electrical leads, which are fed

from an external connection point and through the cold finger sheath, are screwed onto the two copper blocks to supply a current to the resistive heater. Using the resistive heater, the substrate may be heated in excess of 600 K.

2.4.3 Substrate

MgO(100) is a cubic crystal formed by the ionic bonding of Mg^{2+} and O^{2-} . It can be easily cleaved along the (100) plane. Doing so is preferable to acquiring pre-cut, polished substrates because it avoids contamination from the residues of polishing compounds [4]. MgO has an Mg–Mg distance of 2.98 Å; this may aid in the formation of the first monolayer of water, which has been shown to have an O–O distance between neighboring molecules of 2.90 Å, close to the O–O distance in cubic ice (2.75 Å) [4].

Single-crystal MgO has high thermal conductivity at low temperatures: about 250 W/m·K at 100 K [5, 6]. This is necessary to achieve sufficiently low temperatures to condense water vapor onto the surface at 10^{-10} Torr and to ensure that it forms amorphous, rather than crystalline, ice. One of the most important properties of MgO is that it is transparent to infrared, visible, and ultraviolet radiation. It is essential that the substrate does not absorb the 266-nm laser pulse, and useful that it is also transparent to other Nd:YAG harmonic frequencies (355 nm, 532 nm, and 1064 nm). Most important, however, is that transmission Fourier-transform infrared spectroscopic measurements may be carried out using an MgO substrate because it is transparent in the infrared.

The MgO(100) substrate is cleaved in our lab from an unpolished, $1 \times 1 \times 3$ -cm crystal [MTI Corporation]. Cleaving is done under nitrogen to reduce contamination and prevent moisture from interacting with the surface. Cleaving in this manner produces a clean, macroscopically flat surface that primarily has step defects and

oxygen vacancies [4, 7]. The surface is cleaved to a thickness of 1 mm and crimped into the substrate holder. After the resistive heater has been glued and the glue has dried for >1 hr, the entire sample holder is removed from the dry nitrogen environment and mounted to the end of the cold finger as quickly as possible. After the thermocouple is glued to the edge of the MgO surface, the chamber is closed and evacuated.

Once the chamber is evacuated it is heated by the heat lamp or by external heating tapes until it reaches room-temperature pressures on the order of 10^{-9} Torr. The chamber is then filled with oxygen to a pressure of 10^{-7} Torr, and the resistive heater is used to heat the substrate to at least 600 K for one hour. This has been shown to fill the oxygen vacancies left in the MgO from the cleaving process [7, 8]. It also cures the glue used to secure the resistive heater and the thermocouple.

2.5 Instruments Connected to the Chamber

The chamber is set up to accommodate several instruments in different configurations, but the two instruments currently used are the time-of-flight mass spectrometer and the Fourier-transform infrared spectrometer. While the residual gas analyzer is used diagnostically to monitor molecular components present in the chamber and for calibrating deposition pressures, it is not used for experiments that probe our system. The commercial Fourier-transform infrared spectrometer is used in the top tier of the chamber to probe the morphology of the samples. The bulk of the experiments presented herein utilize the custom time-of-flight mass spectrometer located on the middle tier of the chamber.

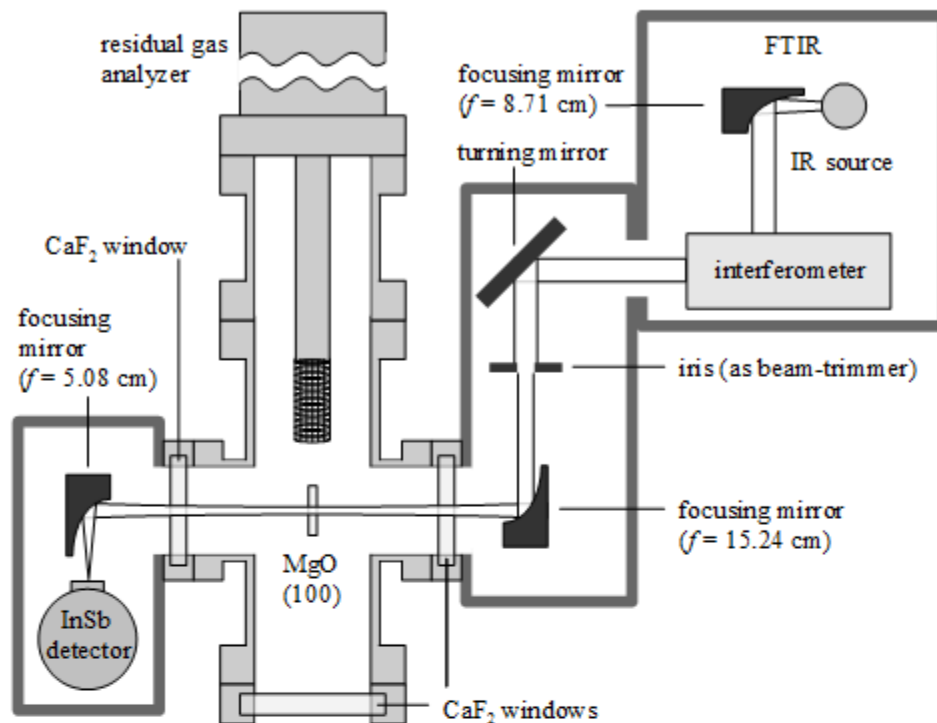


Figure 2.11: A diagram of the top tier of the ultra-high vacuum chamber, with the Fourier-transform infrared spectrometer included. The infrared source is collimated by a focusing mirror and directed into an interferometer. Upon exiting the commercial spectrometer, a flat turning mirror directs the beam through a beam-trimmer and onto a parabolic mirror which focuses the infrared beam onto the MgO surface. Another parabolic mirror turns and focuses the beam onto a liquid nitrogen-cooled InSb detector. The entire spectrometer set-up is purged with dry, CO₂-free air.

2.5.1 Fourier-transform infrared spectroscopy

The Fourier-transform infrared spectrometer [Nicolet Protégé 460] includes an infrared source, a parabolic mirror, and an interferometer. The housing for the broadband infrared source has an aperture that allows uncollimated infrared light to exit; a parabolic turning mirror ($f = 8.71$ cm) turns the beam and also collimates it by matching the divergence of the beam as it exits the infrared light source housing. The mirror directs it into the interferometer, from which it exits the commercial spectrometer.

An airtight dry box fits between the spectrometer and the window into the top tier of the chamber and is sealed at these connections so that the entire beam path

from the spectrometer to the chamber may be purged with dry, CO₂-free air from a purge gas generator [Whatman, model 75-62]. Within this drybox, a flat turning mirror passes the collimated infrared beam through an iris, which is used as a beam-trimmer, and onto another parabolic turning mirror ($f = 15.24$ cm), which focuses the beam on the substrate. The beam then passes through the aperture in the substrate holder, and exits the chamber through the second CaF₂ window. The aperture is about 6×6 mm, and for Fourier-transform infrared spectroscopy experiments that include irradiation the Nd:YAG laser beam diameter is ~ 3 mm. To ensure that the infrared beam passes only through an irradiated area, the beam is reduced to ~ 2 mm by the iris before it is focused onto the surface.

After transmission through the top tier of the chamber, the infrared beam passes into another drybox. The drybox is connected to the flange of the chamber window and sealed so that it can be purged with dry nitrogen from the purge gas generator. A final parabolic turning mirror ($f = 5.08$ cm) focuses the transmitted infrared beam onto a cooled InSb detector. The detector is cooled with liquid nitrogen; once the detector's dewar is full it remains cold enough to acquire signal for several hours.

2.5.2 *Time-of-flight mass spectrometry*

The time-of-flight mass spectrometer is custom built by Jordan TOF Products, Inc. The time-of-flight mass spectrometer is located on the middle tier, with its 48-cm field-free drift region oriented perpendicular to the laser beam path. When the 266-nm laser beam is incident on the substrate containing a sample of N₂O₄, a plume of material is ejected normal to the substrate and perpendicular to the drift region. The plume expands into the ionizing region of the time-of-flight mass spectrometer. An electron gun produces a continuous stream (4.5 A) of 70-eV electrons, which is focused to a rectangle in the x - y plane with an area of 3.175×12.5 mm. If the plume

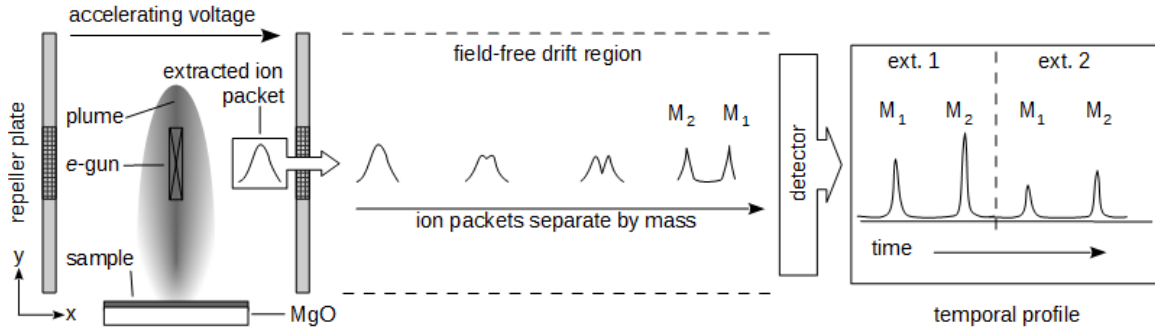


Figure 2.12: Acquisition of a temporal profile via pulsed time-of-flight mass spectrometry. After laser irradiation, a plume of material is ejected normal to the surface, with its axis coincident with the laser path and in the focal plane of the e -gun, which ionizes the plume material. A voltage drop on the extractor plate provides an accelerating voltage gradient which deflects the ionizing e -beam and accelerates a packet of ionized material into the field-free drift region. Continued pulsing of the plate voltage creates a train of ion packets, each of which represents a cross-section of the expanding plume. Each ion packet separates out by mass in the drift region. The series of extracted ion packets are recorded as individual mass spectra, and together make up a temporal profile.

is represented as an ellipsoid expanding from the point of irradiation on the surface, the principal axis of the ellipsoid will lie in the focal plane of the electron beam, assuming optimal alignment of all components [9].

The ionization of plume material and subsequent extraction of ions is triggered by a pulse generator at a rate of 100 kHz, i.e., one extraction and ionization every 10 μ s. A laser pulse at $t = 0$ is followed by 3 μ s of the extraction phase, during which the voltage of the repeller plate is 1800 V and the extractor plate is set to 1550 V. This is followed by a 7 μ s ionization phase: both the repeller and extractor plates are held at 1800 V, and the electron beam ionizes plume material that has reached the ionization region. The plume reaches the ionizing region during this first 7- μ s ionization phase. Extraction of the ionized plume material then begins at $t = 10 \mu$ s, when the voltage on the extractor plate once again drops to 1550 V.

This cycle repeats every 10 μ s, each time giving a full mass spectrum of material that has been ionized during the last 7 μ s of each 10- μ s cycle. Typically, 30 extraction cycles are recorded after each laser pulse to yield a 300- μ s temporal profile, consisting of 30 individual mass spectra representing cross-sections of the plume as it expands into the ionizing region (Fig. 2.12). Occasionally, 60 or 120 extractions are recorded to

provide temporal profiles spanning 600 and 1200 μs , respectively. All of the electronic settings for the time-of-flight mass spectrometer, aside from the repetition rate, are controlled by units supplied by Jordan TOF Products, Inc.

The ions of different masses, all given identical kinetic energy by the electron gun, separate out by mass in the field-free drift region and are incident upon the microchannel plate detector. The signal is then passed through an amplifier [SRS DC-300 MHz], which amplifies the signal $125\times$ before it is relayed to a data acquisition card [GaGe CS8500].

2.6 Chapter 2 References

- [1] Campbell, C. T.; Valone, S. M. *J. Vac. Sci. Technol. A* **1985**, *3*, 408–411.
- [2] Suchan, M. M.; Ph. D. thesis; University of Southern California; 2001.
- [3] Yates, Jr., J. T. *Experimental Innovations in Surface Science*; AIP Press Springer-Verlag: New York, 1998.
- [4] Hawkins, S.; Kumi, G.; Malyk, S.; Reisler, H.; Wittig, C. *Chem. Phys. Lett.* **2005**, *404*, 19–24.
- [5] Makarounis, O.; Jenkins, R. J.; *Thermal diffusivity and heat capacity measurements at low temperatures by the flash method*; Tech. Rep.; U.S. Naval Radiological Defense Laboratory; San Francisco; 1962.
- [6] Slack, G. A. *Phys. Rev.* **1962**, *126*, 427–441.
- [7] Korolik, M.; Suchan, M. M.; Johnson, M. J.; Arnold, D. W.; Reisler, H.; Wittig, C. *Chem. Phys. Lett.* **2000**, *326*, 11–21.
- [8] Heinrich, V. E.; Cox, P. A. *The Surface Science of Metal Oxides*; Cambridge University Press: Cambridge, 1994.
- [9] Anisimov, S. I.; Bäuerle, D.; Luk'Yanchuk, B. S. *Phys. Rev. B* **1993**, *48*, 12076–12081.

CHAPTER 3: EXPERIMENTAL METHODS

This chapter describes the experimental methods in detail. The materials used and the routine experimental preparations that precede all experiments are considered first. The procedure by which samples are deposited on the substrate and subsequently desorbed is described, as well as calibration necessary to determine the quantities of the deposited material. The acquisition and data processing for time-of-flight mass spectrometry and Fourier-transform infrared spectroscopy experiments are detailed, including the alterations to the general procedure that are made for experiments that include Fourier-transform infrared spectroscopy. Lastly, the computational program COMSOL Multiphysics[®] is discussed in terms of its modeling capabilities, and the chosen modeling parameters are justified.

3.1 Materials and Experimental Preparation

Some steps necessary to prepare for experiments, such as the filling of oxygen vacancies in the MgO substrate, must be conducted only periodically and have thus been considered to be part of the process of setting up the experimental apparatus. Others are preparatory processes, which are conducted for each set of experiments. These are instead considered to be essential parts of the process of conducting an experiment and preparing or monitoring the gases used, and are the focus of this chapter.

3.1.1 Materials

Samples of pure H_2O [Macron] are held in a glass vial. When a new sample is used, the vial and dosing line are briefly evacuated. The vial is submerged in a dewar of liquid nitrogen to freeze the sample. Once the sample is frozen, the dosing line is periodically opened to the vacuum system again, and pumped on as the sample thaws and releases trapped air from the solution. This process is repeated at least three times to expel all gases. Water vapor is then leaked into the chamber using the designated precision leak valve, and the residual gas analyzer is used to ensure that the sample does not contain any residual air. The residual gas analyzer is routinely used to check sample purity. If it is not pure, then the freeze-pump-thaw cycle is repeated until the residual gas analyzer shows only water vapor.

The D_2O sample [Cambridge Isotope Laboratories, Inc., 99.9% purity] is housed in an identical vial. The sample is poured into the vial under a dry nitrogen atmosphere to prevent contamination with H_2O . Degassing of the D_2O sample follows the same procedure as for H_2O , as does purity monitoring, though the D_2O is additionally checked for isotopic purity. If the sample is no longer isotopically pure, it is discarded and the vial is refilled. If the new sample is also isotopically impure, then a new, sealed bottle of D_2O is used.

A mixture of NO_2 and N_2O_4 gas from a lecture bottle [Aldrich, $\geq 99.5\%$ purity] is condensed into the sample vial using liquid nitrogen. The frozen sample sometimes shows bright blue N_2O_3 contamination. To remedy this, $\text{O}_2(\text{g})$ is introduced into the vial. After several hours, the sample is frozen in liquid nitrogen once again, and the excess oxygen is pumped out through the vacuum line [1]. Once the sample is prepared, and freezing the sample produces no visible tinge of blue N_2O_3 , the sample is leaked into the chamber and its purity is checked by the residual gas analyzer.

3.1.2 Chamber

Liquid nitrogen is poured into the reservoir of the cold finger while the temperature of the MgO substrate is monitored. When the surface has reached 100 K and the reservoir is full, the pressure in the chamber drops because residual gases have condensed on the cold finger and on the surface. The resistive heater is then turned on to desorb the gases from the surface; the surface is heated to a minimum of 200 K, which is sufficient to desorb all but the first monolayer of condensed water [2].

As discussed in Section 2.2.2, NO_2 cannot be deposited by simply backfilling the chamber because it reacts with the metal walls, degrading to NO. The directed doser (Fig. 2.6) essentially backfills the chamber, but increases the likelihood that a NO_2 molecule impinges on the surface rather than the walls; this will be discussed further in the next section. The x , y , and θ manipulators are used to move the surface away from the body of the time-of-flight mass spectrometer and towards the doser, then turn it so it faces the end of the glass tube. This is the position used for depositing all gases.

3.2 Sample Deposition

For a surface at 100 K, the sticking coefficient of both water and N_2O_4 is unity [3–8]. This means that every molecule incident on the MgO surface subsequently sticks to that surface. We therefore can relate the pressure of a gas to the number of molecules that adsorb in a given amount of time.

Water coverage to form amorphous solid water is often described in monolayers (ML) because this allows one to conceptualize the thickness of a layer without

considering differences in density due to experimental variations. To do this, however, one needs to be able to calibrate to a known number of monolayers. This has been done previously with this experimental apparatus, although it was with a different arrangement of components inside the chamber [2, 9].

When NO_2 is deposited on a surface it dimerizes to form N_2O_4 , with the N–N bond almost normal to the surface on which it is adsorbed [10]. It could thus be thought of as 2 ML of NO_2 , which then dimerize to form a single monolayer of N_2O_4 . However, at 100 K, the bulk vapor-deposited N_2O_4 forms a body-centered cubic crystal with six molecules per unit cell [11, 12]. The bulk does not form what one might conceptualize as monolayers; it is thus more useful to express the amount of N_2O_4 in units of exposure, Langmuirs (L). This unit relates the pressure of the gas and the duration of exposure at this pressure, where $1 \text{ L} = 1 \times 10^{-6} \text{ Torr}\cdot\text{s}$.

For continuity, depositions of both $\text{NO}_2/\text{N}_2\text{O}_4$ and H_2O are expressed in Langmuirs so the relative quantities are easily interpreted. A switch to approximate monolayer quantities and absolute thicknesses is reserved for heat-transfer calculations, for which well-defined values are necessary.

3.2.1 Dosing pressures and times

Temperature-programmed desorption was used to verify that $\text{H}_2\text{O}(\text{g})$ exposure correlated linearly with the amount of $\text{H}_2\text{O}(\text{as})$ adsorbed to the surface. The temperature-programmed desorption traces acquired with the residual gas analyzer (Fig. 3.1) are significantly broader than those previously obtained on this experimental apparatus because of heating inhomogeneities and spatial constraints that did not exist in the previous chamber configurations [2]. However, despite this, it was found that the peak areas do indeed have a relationship that is well fit with a line of the form $y = bx + 0$ (Fig. 3.2). Because of the broad desorption peaks, the

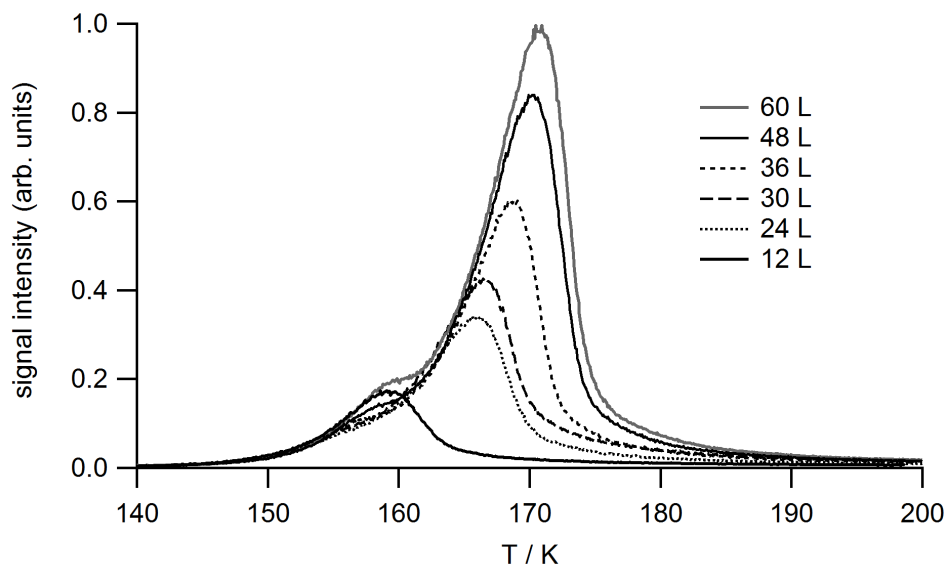


Figure 3.1: Temperature-programmed desorption traces for 12 to 60 Langmuirs of H_2O exposure. Desorption of the first monolayer of H_2O bound to the surface is usually seen around 240 K [2]. The monolayer peak was not detected, and so exposure cannot be quantitatively related to the number of monolayers deposited.

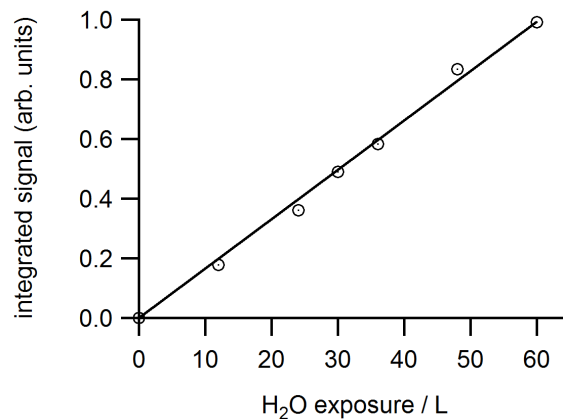


Figure 3.2: Integrated signals from Figure 3.1 as a function of exposure. The amount of material deposited scales linearly with H_2O exposure. Below 12 L the desorption signal is inconsistent and considered to be outside the range of dosing precision. The best fit line, of the form $y = bx + 0$, is shown only as an aid to visualize the linearity of the data and has no quantitative significance.

small amount of monolayer desorption at 240 K was not observed and so the relationship between Langmuirs of exposure and adsorbed monolayers could not be determined [2].

To determine the relationship between the background pressure as measured by the ion gauge, water was dosed through the directed doser and detected using Fourier-transform infrared spectroscopy. 60 L of water was first deposited by exposing the surface to 2×10^{-7} Torr of water vapor for 5 min; a Fourier-transform infrared spectrum was then taken. This spectrum represents water deposited on both faces of the MgO substrate, and so its intensity must be divided by two. Next, water vapor was introduced through the directed doser at the same pressure and for the same amount of time. This spectrum represents 60 L of water that has been background dosed on the back face of the MgO substrate, with a higher deposition rate on the side of the MgO facing the directed doser. The half of the background-dosed spectrum is then subtracted from the direct-dosed spectrum to compare only “front-side” deposition, as we do not expect N_2O_4 to appreciably condense on the back. These spectra are shown in Figure 3.3, and demonstrate that the directed doser deposits $\times 1.67$ the amount of material as background exposure will for the same nominal pressure and time. Our typical N_2O_4 layer is formed using a measured pressure of 2×10^{-7} Torr for a duration of 4 min. This would typically correspond to an exposure of 48 L, but using the directed doser this corresponds to a *local* NO_2 exposure of 80 L, or 40 L of N_2O_4 .

3.2.2 Dosing procedure

When the desired dosing pressure is reached, the time is recorded to the nearest 10 s. Both the pressure reading and the digital clock are visible from the position where one stands while adjusting the leak valves. The pressure reading from the ion

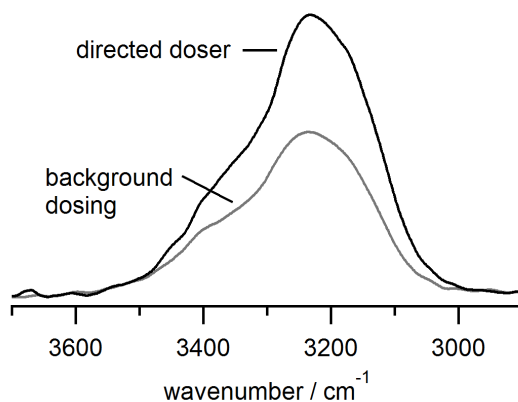


Figure 3.3: Calibration of the directed doser using H₂O. When background dosing H₂O, a pressure of 2×10^{-7} for 5 min will deposit 60 L of H₂O. Using the directed doser, the same pressure and time will deposit $\times 1.67$ as much H₂O, which is equivalent to 100 L.

gauge is monitored during dosing and if the pressure fluctuates (usually only an issue during dosing times >5 min) then the precision leak valve is adjusted accordingly. While dosing gases, the residual gas analyzer is used to monitor the sample purity; however, the pressure reading used for measurement is only taken from the ion gauge. The leak valve is quickly closed when the desired dosing time has elapsed. Between dosing a layer of different material, the total chamber pressure is allowed to at least 5×10^{-9} Torr before another gas is introduced.

3.3 Sample Irradiation

After a sample has been deposited on the substrate, it is moved to face normal to the path of the laser beam. The x , y , z , and θ manipulators are brought to the same coordinates for every experiment. The pulser plates, e -gun, and microchannel plate detector of the time-of-flight mass spectrometer are turned on immediately before an irradiation experiment is to commence. Meanwhile, the laser power is measured (at 10 Hz) and adjusted using the polarizer to attenuate the beam (see Fig. 2.2). For experiments that do not involve Fourier-transform infrared spectroscopy, the laser

power is usually adjusted to $0.5\text{--}4.0\pm 0.2$ mJ per pulse. Once the power has been adjusted, the chopper wheel is started to reduce the repetition rate to 1 Hz. The laser is shuttered using a card.

Often, only the data from the first laser pulse is of interest: subsequent laser pulses are no longer incident upon a known entity, as the first laser pulse induces desorption of material and mixing of layer components. However, multiple pulses in some conditions can yield additional insight. Usually, at least 3 or 4 pulses are allowed to impinge upon a single location on the substrate so that data for multiple laser shots are available if needed later.

One of the improvements made over previous experimental designs was the institution of a signal-averaging protocol. When focused on the substrate, the 266-nm beam is about 0.5 mm in diameter, whereas the area available for irradiation (*i.e.*, the area of the aperture in the substrate holder) is 6×6 mm. The current standard protocol is to irradiate 9 separate locations in a 3×3 grid, each 1 mm apart from the other, by translating the substrate in the x and z directions. This allows for 9 samplings of *the same film*. The diameter of the irradiated area is orders of magnitude larger than the depth of even the thickest samples, and any inhomogeneities inherent to the morphology of porous amorphous solid water are negligible on this scale. The greatest variability in this experimental set-up is fluctuations in the energy of single laser pulses. When the laser power is measured, the power meter averages 10 pulses over one second. Averaging the signals from the first laser shots in 9 different locations on the same sample reduces the signal variation to approximately the variation in pulse-to-pulse laser power.

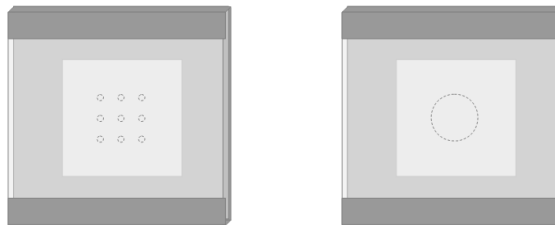


Figure 3.4: Nine-spot irradiation scheme, left, and Fourier-transform infrared spectroscopy irradiation scheme.

3.4 Time-of-Flight Mass Spectrometry

Immediately before irradiation experiments are commenced, the pulser plate, MCP detector, and e -gun are turned on. As described above, the plume of desorbed material enters the ionizing region and, once the desorbed molecules are ionized, the cations are accelerated towards the MCP detector. The particles separate out by mass while in the field-free drift region and impinge upon the MCP detector; the signal from the detector is amplified and then transferred to the data card in the computer system.

3.4.1 Data acquisition and processing

Data acquisition is controlled by a custom LabVIEW program, and settings are dictated by the capabilities of the data card. 150,000 single-value data points of signal intensity can be collected every second. Most frequently, a data point is collected every 2 ns for a duration of 300 μ s. When the data collection is extended to 600 μ s and 1200 μ s, the time between data points increases to every 4 ns and 8 ns, respectively. Given that the broadest mass spectrum peak widths are \sim 50 ns (full-width, half maximum), this does not appreciably affect the resolution of the data.

Although the signal-to-noise in these time-of-flight mass spectrometry experiments is generally very good, two small peaks of noise occur every 10 μ s, which arise from switching the accelerator plates between 1550 V and 1800 V. In an effort to remove

these, and to further improve the quality of the baseline, a typical baseline signal with no material present was Fourier-transformed. It showed large peaks at frequencies of 125, 250, 325, and 500 MHz. At the locations of these peaks, the signal intensity is changed to equal zero; the Fourier transform is then reversed to give a typical signal, but with the amplifier noise greatly reduced.

Signals from the irradiation of all 9 spots are averaged. Mass spectra are created from the temporal profiles by either selecting a single 10 μs time-of-flight spectrum from the temporal profile or by averaging together several consecutive 10 μs spectra and converting their time-of-flight values to mass/charge. The relationship between time and mass in a time-of-flight spectrum is given by Equation 3.1, where t is the time of flight of a particle of mass m with a charge z (one, unless a particle has been doubly ionized), and k is a conversion constant.

$$t = k\sqrt{\frac{m}{z}} \quad (3.1)$$

The conversion is done by selecting peaks which correspond to known fragments and creating a best-fit curve of the form $m = At^2 + Bt + C$ to put these at their correct mass values. The resulting equation is then applied to the time (x) axis of the signal. The Jacobian is used to adjust the signal intensity (y) for each data point to preserve the area of the peaks: the new signal intensity, Y , is given by Equation 3.2.

$$Y = y/(2At + B) \quad (3.2)$$

3.5 Fourier-Transform Infrared Spectroscopy

Experiments that include Fourier-transform infrared spectroscopy are conducted to probe the morphology of the thin films, whether amorphous or crystalline. These experiments require alterations in some of the procedures and also the addition of a few steps. The spectrometer and beam path require preparatory procedures, and then the processes of dosing a sample and irradiating the material are punctuated by steps required for the acquisition of spectra.

3.5.1 *Procedural variations for Fourier-transform infrared spectroscopy*

When Fourier-transform infrared spectroscopy experiments are conducted, a flow of dry nitrogen purges both of the dry boxes external to the spectrometer (see Fig. 2.11). After purging for at least an hour, liquid nitrogen is used to cool the InSb detector, which, once cooled, will maintain constant temperature for several hours. The z manipulator is used to raise the surface into the top tier, to the position where the infrared beam passes through the aperture in the surface holder. The surface is then heated to at least 200 K to desorb water and allowed to cool back to 100 K before a background spectrum is taken. If the background spectrum shows a significant amount of CO₂ or water vapor, the dry boxes continue to be purged until this has been resolved; the surface is then heated again and a new background spectrum is taken.

Once a clean background spectrum is acquired the surface is lowered back to the middle tier of the chamber and into the standard dosing position. After the sample has been deposited on the substrate it is once again moved up to the top tier and an initial spectrum of the un-irradiated sample is taken; it is then moved down to the

middle tier and into position for the irradiation experiments.

For these experiments, the focusing lens is removed so that the laser beam is incident upon a large enough area of the surface, and transmission Fourier-transform infrared spectroscopy can be done mostly on the portion of the sample which has been irradiated (see Figs. 2.2 and 3.4). Because the laser beam is larger than in typical irradiation experiments, the power must be increased to maintain the same fluence. When focused, the spot size of the laser pulse is about 0.5 mm in diameter. The unfocused beam has a diameter of about 3 mm; to maintain fluence the laser power must be increased by a factor of 36 (Eq. 3.3). Usually this increase in power can be attained by removing the polarizer (used only to attenuate the beam) and, if necessary, increasing the amplifier voltage on the laser.

$$P_2 = P_1 \left(\frac{r_2}{r_1} \right)^2 \quad (3.3)$$

3.5.2 Data acquisition and processing

An InSb detector [Nicolet] is used with the Fourier-transform infrared spectrometer, and a commercial program, OMNIC 8, is used to control the spectrometer and detector. 250 scans are taken during the collection of one spectrum; one data point is acquired per 0.964 cm^{-1} in the full range of the detector ($1850\text{--}7400 \text{ cm}^{-1}$). It takes about 25 min to translate the substrate between the irradiation position and the position for Fourier-transform infrared spectroscopy measurements and 6 minutes to accumulate 200 scans with the spectrometer. By the time a spectrum is acquired after irradiation, >1 hr has elapsed from the time of the background spectrum was taken. If, after the final spectrum is taken, there appears to have been a change in the amount of water vapor or CO_2 in the

spectrum, the sample is desorbed and once the chamber pressure has returned to $\sim 10^{-9}$ Torr a new background spectrum is taken. If the new background spectrum better represents the extraneous signal in the final spectrum, this background is used instead.

As discussed, water will condense on both sides of the substrate, while NO_2 will only condense on the front. Therefore, N_2O_4 can absorb radiation only on the front side, and this is where the amorphous solid water can undergo changes as well. The initial spectrum of the unirradiated sample shows signal corresponding to, for example, 60 L of water condensed on the front of the surface plus 60 L condensed on the back side. To quantify how the amorphous solid water has changed in response to irradiation, a signal acquired after irradiation must have half of the initial spectrum subtracted from the final spectrum. The areas of the spectral peaks are fitted with Gaussian peaks, then integrated to determine the total area of the spectrum, as well as the areas and locations of the specific peaks.

3.6 Simulating Heat Transfer Behaviors in COMSOL

COMSOL Multiphysics[®] is a computational program that allows one to graphically construct a system, input material properties, and select desired physical processes for the system to undergo. It allows a user to easily simulate heat transfer phenomena and to change the conditions, the functions that describe variables, and the included physical processes without having to manually alter any actual program scripts. For these calculations, COMSOL uses classical equations to model heat transfer. We use the Heat Transfer Module add-on program to model heat transfer in the system, but this does not allow for simulations of material flow into vacuum.

Heat transfer phenomena depend on the geometry of the system and on the physical properties of its component materials. To model a system such as this, one

needs to obtain numerical values for the materials of the system and to consider which thermodynamic processes are relevant.

The physical properties of the materials used in the experiments have been carefully selected from many sources. The properties of amorphous solid water have been extensively studied, but, as noted, their dependence on the method of preparation complicates things. It has thus been essential to ensure that the quantitative values come from quality research and are specific to amorphous solid water that has been vapor-deposited at 100 K. Fortunately, since the $\text{NO}_2/\text{N}_2\text{O}_4$ system has long been of interest because of its dimerization equilibrium, many of its physical properties have been quantified for all phases. $\text{MgO}(100)$ also has well-quantified properties and, due to its very high thermal conductivity at 100 K and large thickness (1 mm) relative to the sample films, the substrate can be considered to maintain a constant temperature of 100 K.

3.6.1 Modeling MgO

MgO properties are the easiest to define for these calculations for two reasons. One is that our MgO substrate is pure and has a known crystal structure. Additionally, it can be considered to remain at 100 K because it is a good thermal conductor; its properties do not need to be considered temperature-dependent other than using temperature-dependence as a means to interpolate the 100-K values.

Slack (1962) and Makarounis and Jenkins (1962) both present graphs of the measured thermal conductivity of $\text{MgO}(100)$ over a range of temperatures. Their data are consistent with one another, and give a thermal conductivity of about $0.6 \text{ cal/cm}\cdot\text{s}\cdot\text{K}$, or $250 \text{ W/m}\cdot\text{K}$, at 100 K [13, 14]. Barron et al. (1959) measured the heat capacity of single-crystal $\text{MgO}(100)$ from 3 K to 270 K. The heat capacity, interpolated from explicitly given numerical values, is $193.7 \text{ J/kg}\cdot\text{K}$ at 100 K.

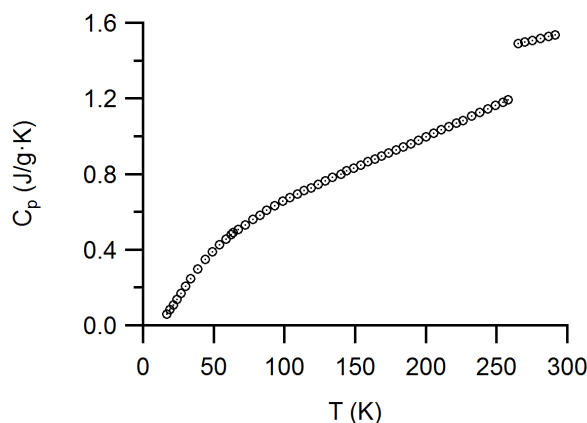


Figure 3.5: Heat capacity of solid N_2O_4 as a function of temperature, as measured by Giauque and Kemp (1938) [16]. Above 100 K the heat capacity is exceptionally linear; a best fit line of their data between 90 and 260 K is used to represent the temperature-dependent heat capacity of solid N_2O_4 .

Additionally, Barron et al. give a density of 3.591 g/cm^3 for single-crystal $\text{MgO}(100)$ at 100 K [15].

3.6.2 Modeling N_2O_4

When solid N_2O_4 is formed from condensed vapor it takes on a cubic crystal structure with a density of 1.966 g/cm^3 [11]. Careful measurements of the heat capacity of solid N_2O_4 were made by Giauque and Kemp in 1938 from 16 K to its melting point (261.9 K) in increments of about 3 K [16]. Above 100 K the heat capacity is exceptionally linear; a best fit line of their data between 90 and 260 K is used to represent the temperature-dependent heat capacity of solid N_2O_4 (Fig. 3.5).

While quality data exist regarding the density and heat capacity of solid N_2O_4 , defining its thermal conductivity at 100 K is a different story, much less defining its temperature dependence. No such measurements have been found, and we are forced to instead look to molecular analogues for an approximate value.

The thermal conductivity of solid hydrazine, N_2H_4 , is $1.57 \text{ W/m}\cdot\text{K}$ for a sample brought into thermal contact with a reservoir at 253.15 K at one end and 261.15 K

at the other [17]. At 100 K, solid, polycrystalline ammonia (NH_3) has a thermal conductivity of 1.76 W/m·K [18]. Considering the large uncertainty, we only know the order of magnitude, and settle for a thermal conductivity of 1 W/m·K.

3.6.3 Modeling amorphous solid water

Giauque and Stout (1936) measured the heat capacity of hexagonal ice from 16–268 K, and Handa and Klug (1988) measured the heat capacities of pressure-amorphized, low-density amorphous ice samples that had been annealed to temperatures at or below 130 K, then allowed to transition to cubic ice, starting at about 135 K [16, 19]. The heat capacities of crystalline versus amorphous ice are not expected to differ much, and this can indeed be seen by comparing the measured heat capacities of low-density amorphous ice, I_c , and I_h as in Figure 3.6 [20]. A continuous function is needed for input into COMSOL. Because the measured heat capacities of the three polymorphs do not vary by much, the temperature-dependent heat capacity of ice I_h is used.

The intrinsic density of all forms of low-density amorphous ice is well established: 0.94 g/cm³ [21–24]. Vapor deposition at 100 K results in porous amorphous solid water with a bulk density of 0.82 g/cm³ and a fractional porosity (V_{pore}/V_{total}) of 0.13 ± 0.01 ; this corresponds to a pore volume of 0.16 cm³/g [5, 23–25]. For the purposes of COMSOL calculations, the density of amorphous solid water is not considered temperature dependent.

There are many purported values for the thermal conductivity of amorphous ice, and they span an incredible three orders of magnitude [26]. For the purposes of these calculations, this quantity is perhaps the most critical — as the only non-crystalline solid in our system, the thermal conductivity of amorphous solid water is the limiting factor in heat transfer because it has the lowest value. It is used as a thermal buffer

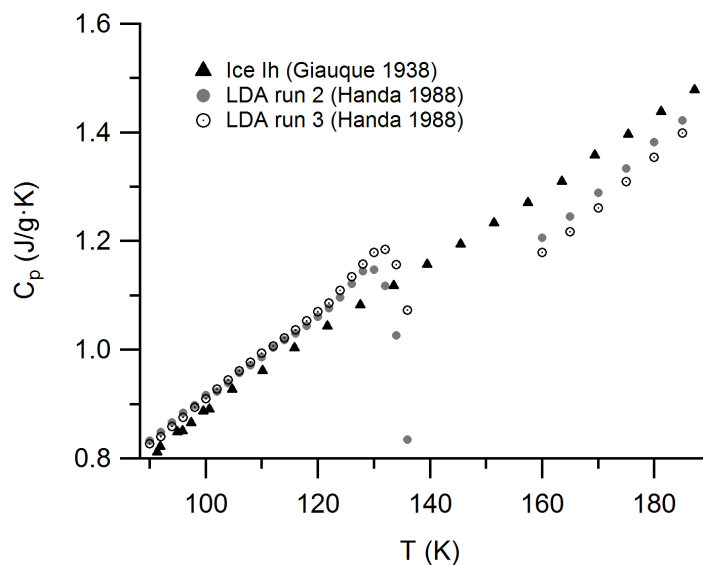


Figure 3.6: Heat capacities of ice I_h [16] and pressure-amorphized low-density amorphous ice [19]. Around 135 K the heat capacity of low-density amorphous ice changes rapidly as it undergoes a phase transition to ice I_c ; in the data presented here from Handa et al. this transformation is completed by 160 K .

between the N_2O_4 and MgO substrate specifically because it reduces the rate of cooling by the MgO. Picking apart which values are reliable is no trivial task, in part because porosity greatly affects thermal conductivity. We must start with the thermal conductivity of non-porous low-density amorphous ice and then consider the effects of porosity.

One of the most frequently cited thermal conductivity values is an estimate by Klinger in 1980. Klinger asserts that the conductivity of an amorphous ice is at least ten times smaller than for hexagonal ice [27]. At 100 K, the thermal conductivity of hexagonal ice is 6.5 W/m·K, giving an upper limit of 0.65 W/m·K for amorphous ice [28]. Klinger uses a classical equation for thermal conductivity,

$$\kappa = \frac{1}{4}cv\lambda\rho \quad (3.4)$$

in which c is the heat capacity per unit mass, v is the speed of sound in the

material, λ is the phonon mean free path, and ρ is the density. Klinger uses the values for hexagonal ice for all except the phonon mean free path, which he reduces to 5 Å— about the size of a generic unit cell. This results in an estimated thermal conductivity for amorphous ice of about 0.25 W/m·K at 100 K. Yu and Leitner (2005) used molecular dynamics simulations to calculate the thermal conductivity of low-density amorphous ice by quenching liquid water that was given the same density as low-density amorphous ice, and by perturbing cubic ice. Both simulations yielded thermal conductivities of about 0.2 W/m·K [29].

Another oft-cited value is 0.6 W/m·K for low-density amorphous ice at 100 K, reported in 1994 by Anderson et al. [30]. However, in a 2002 paper they correct this value, stating that this was in fact the measured thermal conductivity for high-density amorphous ice [31]. Their 2005 paper measured a thermal conductivity of 1.4 W/m·K at 100 K, decreasing to 1.1 W/m·K at 125 K [32]. Employing equilibrium molecular dynamics simulations and experimentally measured values, English et al. found a thermal conductivity for low-density amorphous ice of about 1.1 W/m·K at 100 K, decreasing to 1.0 W/m·K at 180 K [33, 34]. Although these values may intuitively seem too high for an amorphous solid, the work of Andersson et al. and English et al. are the most thorough, the most consistent, and present both experiments and simulations with solid interpretation. Amorphous solid water has a relatively high degree of order for an amorphous solid, and these are thus the preferred values.

The porosity of vapor-deposited ice must now be taken into account, to consider how much it will affect the conductivity. The porosity of vapor-deposited amorphous solid water is expected to have a maximum effect on the conductivity when the pores and the solid are both interconnected, rather than having the pores isolated from one another. This can be modeled using the Effective Medium Theory, which allows for an “intruding” material to occupy the pore space [35]:

$$\frac{v_1(\kappa_1 - \kappa_{eff})}{\kappa_1 + 2\kappa_{eff}} + \frac{v_2(\kappa_2 - \kappa_{eff})}{\kappa_2 + 2\kappa_{eff}} = 0 \quad (3.5)$$

The effective thermal conductivity, κ_{eff} , is a function of the thermal conductivities of the two continuous media, κ_1 and κ_2 , and the fractional volume of the intruding phase, v_2 . By definition, the the intruding phase is the phase of smaller fractional volume, *i.e.*, $v_1 > v_2$. With empty pores (*i.e.*, $\kappa_2 = 0$), this can be rewritten for amorphous solid water as:

$$\kappa_{eff} = \left(1 - \frac{3v_{pore}}{2}\right) \kappa_{ASW} \quad (3.6)$$

where κ_{ASW} is the thermal conductivity of non-porous amorphous solid water and v_{pore} is the fractional porosity of the film. For the expected fractional porosity of 0.13, $\kappa_{eff} = 0.8\kappa_{ASW}$. We conclude that, given that the measured non-porous conductivities of 1.4 W/m·K by Andersson et al. (2005) and 1.1 W/m·K by English et al. (2010, 2011) results in effective thermal conductivities of 0.9 and 1.1 W/m·K, respectively, that vapor-deposited amorphous solid water will be well modeled by a thermal conductivity of 1 W/m·K [32–34]. Given how little their measured conductivities change with respect to temperature, the thermal conductivity it held constant for all temperatures. Table 3.1 summarizes the values used for all three materials at 100 K.

3.6.4 Modeling heat transfer in a multi-layer film

The typical N₂O₄ layer used in these experiments is formed from the deposition of 80 L of NO₂, deposited over 180 L of H₂O(as). As discussed in Section 3.2.1,

Table 3.1: Values used for heat capacity (C_p , J/kg·K), thermal conductivity (κ , W/m·K), and density (ρ , g/cm³) of MgO(100), N₂O₄, and H₂O(as) at 100 K. †Value is allowed temperature dependence

	C_p	κ	ρ	Sources
MgO(100)	193.7	250	3.591	[13–15]
N ₂ O ₄	665 †	1	1.966	[11, 16–18]
H ₂ O(as)	889 †	1	0.82	[5, 32–36]

we rely on previously conducted calibrations relating gas exposure to the formation of monolayers of H₂O(as): 0.6 L H₂O = 1 monolayer. A monolayer of water has 1.06×10^{15} molecules/cm²; taking dimerization and into account, 80 L of NO₂ should thus deposit a total of 6.6×10^{16} molecules/cm². Using a density of 1.966 g/cm³, this corresponds to a N₂O₄ layer with a thickness of ~ 50 nm. Similarly, using the porous amorphous solid water density of 0.82 g/cm³, our typical 180 L H₂O(as) bottom-layer thickness is ~ 115 nm. Because the system is symmetric in the plane of the 1-mm thick MgO substrate, we may choose any dimensions in this direction. A typical film is shown in Figure 3.7.

The lower boundary of the film is designated a “highly conductive layer” with a 1-mm thickness. This boundary is given a constant temperature of 100 K. Heat transfer across the boundary is calculated using the equation

$$-\mathbf{n} \cdot (-k\nabla T) = d_s \left(Q_s - \rho_s C_s \frac{\partial T}{\partial t} \right) - \nabla_t \cdot (-d_s k_s \nabla_t T) \quad (3.7)$$

where \mathbf{n} is the normal vector on the boundary, k is the thermal conductivity, T is the temperature, d is the layer thickness, Q represents heat sources within the layer, ρ is the material density, C is the heat capacity, and t is time. The subscript s indicates that the value is a property specific to the material of the highly conductive layer. Note that k is an input value (constant for all materials used here) and T is a variable;

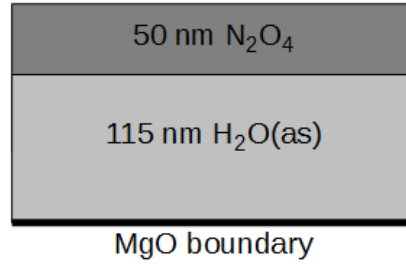


Figure 3.7: Geometry of a $\text{H}_2\text{O}(\text{as})/\text{N}_2\text{O}_4$ film, as used in COMSOL. These dimensions correspond to N_2O_4 formed from 80 L NO_2 , over 180 L $\text{H}_2\text{O}(\text{as})$. The MgO is not explicitly drawn, but is designated as a highly conductive boundary with a thickness of 1 mm.

$k\nabla T$ is the heat flux, and is proportional to the temperature gradient [37].

In all calculations presented herein, $Q = 0$ for the highly conductive layer. Additionally, because the temperature of the boundary is held constant, $\partial T/\partial t = 0$; Equation 3.7 reduces to Equation 3.8.

$$\mathbf{n} \cdot (-k\nabla T) = \nabla_t \cdot (-d_s k_s \nabla_t T) \quad (3.8)$$

The boundary between N_2O_4 and $\text{H}_2\text{O}(\text{as})$ is considered to have ideal thermal contact, and the boundary only signifies a change in physical properties. At the left and right boundaries, as well as the surface-vacuum interface, we create a thermally insulated barrier by requiring that the heat flux across the boundary is zero:

$$-\mathbf{n} \cdot (k\nabla T) = 0 \quad (3.9)$$

In the rest of the film, heat conduction is calculated using a more general equation for heat transfer in solids:

$$\rho C_p \frac{\partial T}{\partial t} = \nabla \cdot (k\nabla T) \quad (3.10)$$

Films of varying thicknesses are modeled. The $\text{H}_2\text{O}(\text{as})$ layers are given an initial temperature of 100 K, and the N_2O_4 layer is initially at some higher temperature. The system is then allowed to evolve over time. Desorption and phase changes are neglected.

3.7 Chapter 3 References

- [1] Agnew, S. F.; Swanson, B. I.; Jones, L. H.; Mills, R. L.; Schiferl, D. *J. Phys. Chem.* **1983**, *87*, 5065–5068.
- [2] Hawkins, S.; Kumi, G.; Malyk, S.; Reisler, H.; Wittig, C. *Chem. Phys. Lett.* **2005**, *404*, 19–24.
- [3] Batista, E. R.; Ayotte, P.; Bilić, A.; Kay, B. D.; Jónsson, H. *Phys. Rev. Lett.* **2005**, *95*, 223201(4).
- [4] Speedy, R. J.; Debenedetti, P. G.; Smith, R. S.; Huang, C.; Kay, B. D. *J. Chem. Phys.* **1996**, *105*, 240–244.
- [5] Brown, D. E.; George, S. M.; Huang, C.; Wong, E. K. L.; Rider, K. B.; Smith, R. S.; Kay, B. D. *J. Phys. Chem.* **1996**, *100*, 4988–4995.
- [6] Dixon-Warren, S. J.; Jackson, R. C.; Polanyi, J. C.; Rieley, H.; Shapter, J. G.; Weiss, H. *J. Phys. Chem.* **1992**, *96*, 10983–10994.
- [7] Bartram, M. E.; Koel, B. E. *Surf. Sci.* **1989**, *213*, 137–156.
- [8] Sato, S.; Senga, T.; Kawasaki, M. *J. Phys. Chem. B* **1999**, *103*, 5063–5069.
- [9] Kumi, G.; Ph. D. thesis; University of Southern California; 2007.
- [10] Rieley, H.; Colby, D. J.; McMurray, D. P.; Reeman, S. M. *Surf. Sci.* **1997**, *390*, 243–249.
- [11] Kvick, A.; McMullan, R. K.; Newton, M. D. *J. Chem. Phys.* **1982**, *76*, 3754–3761.
- [12] Campbell, M. J.; Liesegang, J.; Riley, J. D.; Jenkin, J. G. *J. Phys. C* **1982**, *15*, 2549–2558.
- [13] Slack, G. A. *Phys. Rev.* **1962**, *126*, 427–441.
- [14] Makarounis, O.; Jenkins, R. J.; *Thermal diffusivity and heat capacity measurements at low temperatures by the flash method*; Tech. Rep.; U.S. Naval Radiological Defense Laboratory; San Francisco; 1962.
- [15] Barron, T. H. K.; Berg, W. T.; Morrison, J. A. *Proc. R. Soc. London A* **1959**, *250*, 70–83.
- [16] Giauque, W. F.; Kemp, J. D. *J. Chem. Phys.* **1938**, *6*, 40–51.
- [17] Chang, E. T.; Poston, T. M.; Gokcen, N. A.; *Density, Compressibility, Thermal Conductivity, and Mechanical Movement of Solid Hydrazine*; Tech. Rep.; The Aerospace Corporation; El Segundo; 1976.

- [18] Krupskii, I. N.; Manzhely, V. G.; Koloskova, L. A. *Phys. Status Solidi* **1968**, *27*, 263–268.
- [19] Handa, Y. P.; Klug, D. D. *J. Phys. Chem.* **1988**, *92*, 3323–3325.
- [20] Shulman, L. M. *Astron. Astrophys.* **2004**, *416*, 187–190.
- [21] Narten, A. H.; Venkatesh, C. G.; Rice, S. A. *J. Chem. Phys.* **1976**, *64*, 1106–1121.
- [22] Ghormley, J. A.; Hochanadel, C. J. *Science* **1971**, *171*, 62–64.
- [23] Dohnálek, Z.; Kimmel, G. A.; Ayotte, P.; Smith, R. S.; Kay, B. D. *J. Chem. Phys.* **2003**, *118*, 364–372.
- [24] Westley, M. S.; Baratta, G. A.; Baragiola, R. A. *J. Chem. Phys.* **1998**, *108*, 3321–3326.
- [25] Seiber, B. A.; Wood, B. E.; Smith, A. M.; Müller, P. R.; Delsemme, A. H.; Wenger, A. *Science* **1970**, *170*, 652–654.
- [26] Hessinger, J.; White, Jr., B. E.; Pohl, R. O. *Planet. Space Sci.* **1996**, *44*, 937–944.
- [27] Klinger, J. *Science* **1980**, *209*, 271–272.
- [28] Slack, G. A. *Phys. Rev. B* **1980**, *22*, 3065–3071.
- [29] Yu, X.; Leitner, D. M. *J. Chem. Phys.* **2005**, *123*, 104503(10).
- [30] Andersson, O.; Suga, H. *Solid State Commun.* **1994**, *91*, 985–988.
- [31] Andersson, O.; Suga, H. *Phys. Rev. B* **2002**, *65*, 140201(4).
- [32] Andersson, O.; Inaba, A. *Phys. Chem. Chem. Phys.* **2005**, *7*, 1441–1449.
- [33] English, N. J.; Tse, J. S.; Gallagher, R. *Phys. Rev. B* **2010**, *82*, 092201(4).
- [34] English, N. J.; Tse, J. S. *Phys. Rev. B* **2011**, *83*, 184114(9).
- [35] Carson, J. K.; Lovatt, S. J.; Tanner, D. J.; Cleland, A. C. *Int. J. Heat Mass Transf.* **2005**, *48*, 2150–2158.
- [36] Giaque, W. F.; Stout, J. W. *J. Am. Chem. Soc.* **1936**, *58*, 1144–1150.
- [37] Incropera, F. P.; DeWitt, D. P.; Bergman, T. L.; Lavine, A. S. *Fundamentals of Heat and Mass Transfer*, 6th ed.; John Wiley & Sons, 2006.

CHAPTER 4: RESULTS AND DISCUSSION

Time-of-flight mass spectra and temporal profiles were recorded for molecules that enter the gas phase following 266-nm irradiation using the sandwich arrangement indicated in Figure 4.1. To interpret these spectra, it was necessary to obtain individual spectra of the stable molecules that arise in the experiments: N_2O_4 , NO_2 , NO , and H_2O . It is noteworthy that N_2O_4 yields no ions more massive than NO_2^+ in its mass spectrum, which complicates distinguishing N_2O_4 from NO_2 ; these results are presented in Section 4.1. Section 4.1 also demonstrates the changes in Fourier-transform infrared spectroscopic signatures in response to morphological changes in amorphous solid water layers. In addition, temporal profiles and their individual mass spectra were recorded for material released into vacuum following the 266-nm irradiation of exposed N_2O_4 . These data are presented in Section 4.2.

In Section 4.3, mass spectra and temporal profiles are presented for the first laser pulse to interact with freshly prepared samples such as the one indicated in Figure 1. The time-of-flight mass spectra provide excellent single-shot signal-to-noise. Results for the second, third, etc. pulses incident on the same spot are presented in Section 4.8.3. No signal averaging is carried out between time-of-flight mass spectrometry results from successive pulses that fall incident on

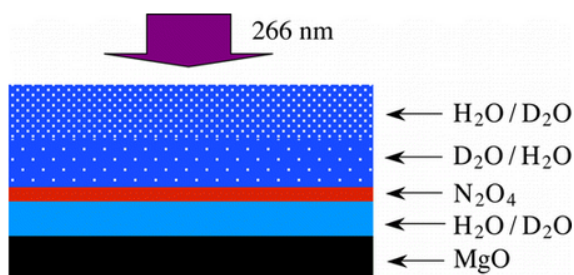


Figure 4.1: Schematic drawing indicating the structure of the films used in the present study. The black layer is the MgO substrate. Solid blue is an amorphous solid water layer that insulates the (red) N_2O_4 layer from the MgO, which has high thermal conductivity. The upper amorphous solid water layer can be H_2O , D_2O , or a combination.

the same spot. In other words, effects due to the first, second, third, etc. pulses are isolated from one another. In Section 4.5, it is shown that material ejection takes place through fissures that originate at the laser-heated region. At low fluence, the progress of the N_2O_4 -rich material toward vacuum stops short of ejecting material. A second (or third) pulse acts on the trapped material in the incipient fissure, enabling it to enter vacuum. Experimental results obtained using layers of $\text{D}_2\text{O}(\text{as})$ and $\text{H}_2\text{O}(\text{as})$ in the upper layer are presented in Section 4.6, demonstrating that water that enters vacuum comes from the fissure walls. Results obtained using Fourier-transform infrared spectroscopy are presented in Section 4.7.

4.1 Single-Species Mass Spectra and Infrared Spectra of Ice

Because we are probing a multi-component system with inherently complex behavior, it is necessary to have a sound knowledge of the time-of-flight mass spectrometry signals that would arise from the most likely system components. This study makes use of comparing the intensities of peaks arising from individual daughter ions, and it is essential to establish the cracking patterns of each possible parent ion: aside from water, we look to the cracking patterns of NO_2 , N_2O_4 , and NO . For Fourier-transform infrared spectroscopy comparisons, we establish the signature of pure, fully amorphous ice and compare it to films that have been heated to induce morphological changes.

4.1.1 Mass Spectra of NO_2 , N_2O_4 , NO , and H_2O

Mass spectra of NO_2 , N_2O_4 , NO , and H_2O were recorded using our apparatus, as opposed to relying on spectra taken from the literature. This obviates the need to account for differences due to experimental arrangements, *e.g.*, time-of-flight versus

quadrupole. Relevant mass spectra are shown in Figure 4.3. Those for NO_2 , NO , and H_2O can be found in the literature, but we find that our cracking patterns differ slightly from those reported in the NIST database [1]. The mass spectrum of gaseous N_2O_4 was not available in the literature. Its acquisition was more challenging, as discussed below.

Mass spectra of pure H_2O , NO , and NO_2 were obtained by backfilling the chamber while the time-of-flight mass spectrometer acquired signal. We have discussed the issues of NO_2 decomposing on contact with metal surfaces and the use of a directed doser which points towards the substrate (see Sec. 2.2.2); however, gas exits the doser very close to the ionizing region of the time-of-flight mass spectrometer (Fig. 2.5), and we make the assumption that any NO_2 which enters the ionizing region does so with negligible degradation. Nitrogen oxide produces a signal that is distinct from NO_2 in that it shows a small signal at $m/q = 15$ due to NO^{2+} [1]. Additionally, when NO^+ breaks apart the nitrogen preferentially carries the charge, as seen in Figure 4.3.

Mass spectra of gaseous N_2O_4 were obtained by thermal desorption of a N_2O_4 film from the MgO substrate. The substrate was heated to about 155 K, where the N_2O_4 film began to sublime. The dissociation $\text{N}_2\text{O}_4 \rightarrow 2\text{NO}_2$ is endoergic by 4440 cm^{-1} [2], whereas the binding energy of a N_2O_4 molecule to its solid is 3800 cm^{-1} [3]. For NO_2 to enter the gas phase during sublimation, it would be necessary to break the N–N bond in N_2O_4 and then desorb NO_2 . The difference between the energies required to enter the gas phase for N_2O_4 versus NO_2 implies that only a small percentage of NO_2 leaves the film. Additionally, it is notable that neither N_2O_4^+ nor N_2O_3^+ is observed; N_2O_3^+ has been cited as a stable daughter ion, but this ion has only been reported once experimentally [4].

If the N_2O_4 that sublimates from its solid around 155 K strikes a nearby (300 K) metal surface, it can stick and dissociate, yielding two surface-bound NO_2 molecules. In turn, NO_2 may be released into the gas phase. This would yield a

Table 4.1: A summary of the relative amounts of each daughter ion for pure NO, NO₂, and N₂O₄.

	N ⁺ /NO ₂ ⁺	O ⁺ /NO ₂ ⁺	NO ⁺ /NO ₂ ⁺	N ⁺ /NO ⁺	O ⁺ /NO ⁺
NO				0.06	0.01
NO ₂	0.19	0.58	3.18	0.06	0.18
N ₂ O ₄	0.02	0.1	0.9	0.02	0.11

N₂O₄ spectrum that is contaminated by NO₂. This was checked by constructing a new accelerating plate that placed an aperture in front of the substrate to collimate the desorbing material, reducing the likelihood that it enters the ionizing region after impinging upon the accelerating or extracting plate of the time-of-flight mass spectrometer (Fig. 4.2). The first iteration of this new plate was symmetric, and had equal apertures on either side to allow the un-ionized portion of the plume to pass out of the time-of-flight mass spectrometer; it was necessary to keep the plate approximately symmetric to prevent distortion of the electric field. However, this placed a significant amount of metal opposite the sample, as indicated in Figure 4.2a, and the measured NO⁺/NO₂⁺ ratio increased to ~1.0. This indicates that the presence of NO₂ was brought about through collisions of N₂O₄ with the metal surface facing the plume. However, by greatly increasing the size of the aperture opposite the plume (Fig. 4.2b), the spectra gave the same signature as those acquired with no plate modifications, indicating that collisions with the time-of-flight mass spectrometer plates are not an issue for thermally desorbed samples. We conclude from these experiments that the NO⁺/NO₂⁺ ratio is 0.9 for N₂O₄ subliming at 155 K. To the best of our knowledge, this is the first report of a direct measurement of the cracking pattern of this molecule.

The amount of NO⁺ relative to NO₂⁺ is denoted NO⁺/NO₂⁺, where NO⁺ and NO₂⁺ are the areas of the respective signals, and likewise for O⁺/NO₂⁺ and N⁺/NO₂⁺. A summary of the daughter ion ratios for pure NO, NO₂, and N₂O₄ is given in

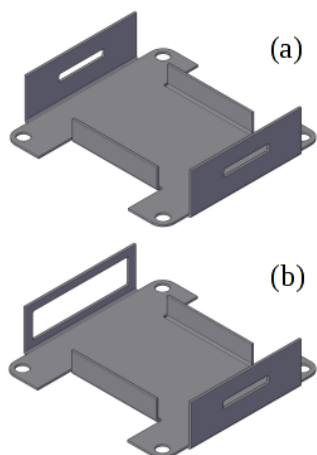


Figure 4.2: Apertured time-of-flight mass spectrometer accelerating plates used to acquire a pure N_2O_4 signal. (a) first design (b) second design.

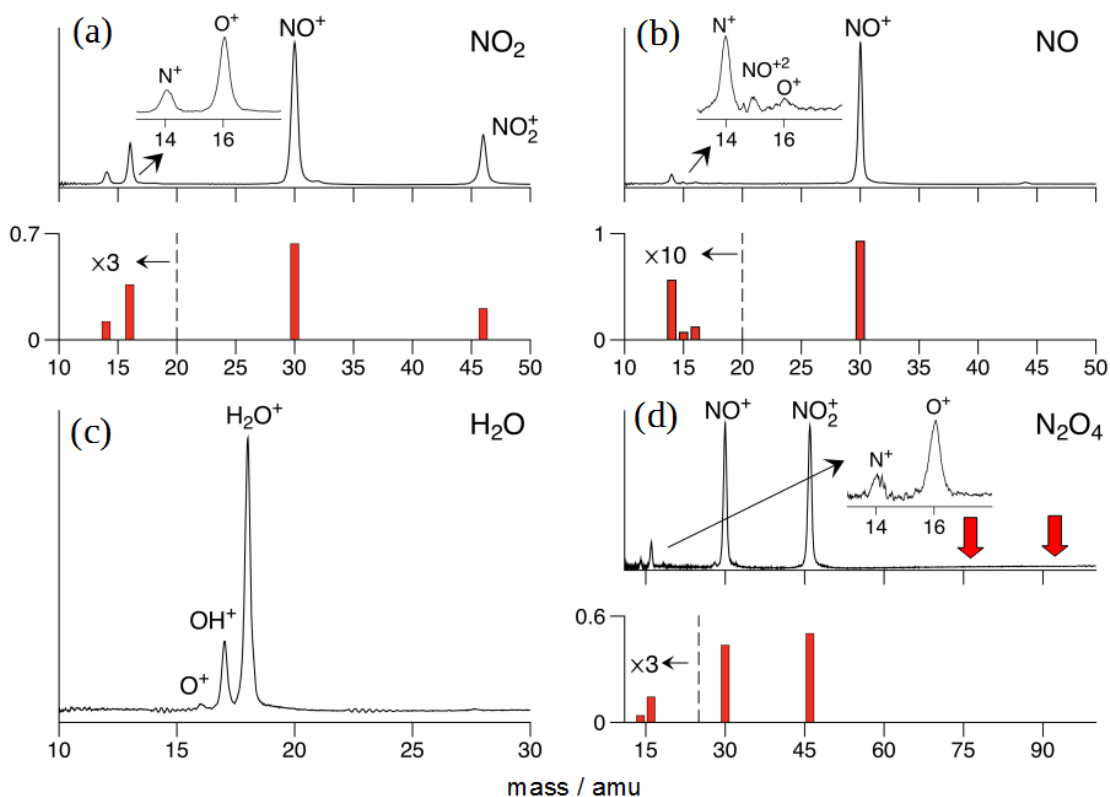


Figure 4.3: Mass spectra of (a) NO_2 at 300 K; (b) NO at 300 K, (c) H_2O at 300 K, and (d) solid N_2O_4 that has been sublimed at 155 K. Note the absence of signal at 76 and 92 amu (N_2O_3^+ and N_2O_4^+). The red bars represent the integrated areas of the peaks to aid in visualization. The ratios of the peak areas for NO , NO_2 , and N_2O_4 are summarized in Table 4.1.

Table 4.2: 70-eV ionization cross-sections ($\sigma \times 10^{-16} \text{ cm}^2$). Values are from the NIST database [1], except for N_2O_4 , which was computed [5].

species	σ	species	σ
N_2O_4	7.34	NO_2	3.53
NO	2.81	O_2	2.41
N_2	2.51	H_2O	2.28
O	1.36		

Table 4.1. The large difference in $\text{NO}^+/\text{NO}_2^+$ values for NO_2 and N_2O_4 facilitates analyses. Neutral species, *e.g.*, $\text{NO}_2/\text{N}_2\text{O}_4$, are denoted similarly. These latter ratios take into account the 70-eV ionization cross sections for N_2O_4 , NO_2 , NO , and O (Table 4.2), and will be discussed in the next section.

4.1.2 The $\text{NO}_2/\text{N}_2\text{O}_4$ ratio

An expression is derived for the ratio of the NO_2 and N_2O_4 concentrations that reach the ionization region of the mass spectrometer. It is in terms of ionization cross-sections, parent ion fragmentation patterns, and relative ion signals. For example, use is made of measured quantities such as $\text{NO}^+/\text{NO}_2^+$, where NO^+ and NO_2^+ denote the areas of the respective ion signals. It is assumed that the microchannel plate detector has equal sensitivity for each ion. To begin, expressions for the amounts (concentrations) of NO_2^+ , NO^+ , and O^+ are written

$$\text{NO}_2^+ = \sigma_{\text{N}_2\text{O}_4}^{\text{ion}} F_{\text{N}_2\text{O}_4^+}^{\text{NO}_2^+} \text{N}_2\text{O}_4 + \sigma_{\text{NO}_2}^{\text{ion}} F_{\text{NO}_2^+}^{\text{NO}_2^+} \text{NO}_2 \quad (4.1)$$

$$\text{NO}^+ = \sigma_{\text{N}_2\text{O}_4}^{\text{ion}} F_{\text{N}_2\text{O}_4^+}^{\text{NO}^+} \text{N}_2\text{O}_4 + \sigma_{\text{NO}_2}^{\text{ion}} F_{\text{NO}_2^+}^{\text{NO}^+} \text{NO}_2 + \sigma_{\text{NO}}^{\text{ion}} F_{\text{NO}^+}^{\text{NO}^+} \text{NO} \quad (4.2)$$

$$\text{O}^+ = \sigma_{\text{N}_2\text{O}_4}^{\text{ion}} F_{\text{N}_2\text{O}_4^+}^{\text{O}^+} \text{N}_2\text{O}_4 + \sigma_{\text{NO}_2}^{\text{ion}} F_{\text{NO}_2^+}^{\text{O}^+} \text{NO}_2 + \sigma_{\text{H}_2\text{O}}^{\text{ion}} F_{\text{H}_2\text{O}^+}^{\text{O}^+} + \sigma_{\text{NO}}^{\text{ion}} F_{\text{NO}^+}^{\text{O}^+} \text{NO} + \sigma_{\text{O}}^{\text{ion}} \text{O} \quad (4.3)$$

where σ_X^{ion} is the 70 eV ionization cross section for the neutral species X , and $F_{X^+}^{Y^+}$ is the fraction of daughter ion Y^+ that arises from fragmentation of the parent ion X^+ .

The use of equals signs rather than proportionality constants in Equations 4.1 – 4.3 is in anticipation of the fact that these constants would cancel (see below) were they carried along. The relatively small amount of O_2^+ that appears in spectra shall be ignored. Likewise, it is assumed that the NO and O concentrations are negligible. This is a safe assumption for long arrival times at the ionization region, though less so for short arrival times. Therefore, the last term in Equation 4.2 and the last two terms in Equation 4.3 are dropped, in which case Equation 4.3 is decoupled from Equations 4.1 and 4.2. Considering Equation 4.2, the relationship $\text{NO}^+ = (\text{NO}^+/\text{NO}_2^+)\text{NO}_2^+$ is introduced. Combining Equations 4.1 and 4.2 then yields

$$\left(\frac{\text{NO}^+}{\text{NO}_2^+}\right) \left(\sigma_{\text{N}_2\text{O}_4}^{\text{ion}} F_{\text{N}_2\text{O}_4^+}^{\text{NO}_2^+} \text{N}_2\text{O}_4 + \sigma_{\text{NO}_2}^{\text{ion}} F_{\text{NO}_2^+}^{\text{NO}_2^+} \text{NO}_2\right) = \sigma_{\text{N}_2\text{O}_4}^{\text{ion}} F_{\text{N}_2\text{O}_4^+}^{\text{NO}^+} \text{N}_2\text{O}_4 + \sigma_{\text{NO}_2}^{\text{ion}} F_{\text{NO}_2^+}^{\text{NO}^+} \text{NO}_2 \quad (4.4)$$

Separating this equation into separate terms for NO_2 and N_2O_4 gives

$$\text{NO}_2 \sigma_{\text{NO}_2}^{\text{ion}} \left(\left(\frac{\text{NO}^+}{\text{NO}_2^+}\right) F_{\text{NO}_2^+}^{\text{NO}_2^+} - F_{\text{NO}_2^+}^{\text{NO}^+} \right) = \text{N}_2\text{O}_4 \sigma_{\text{N}_2\text{O}_4}^{\text{ion}} \left(F_{\text{N}_2\text{O}_4^+}^{\text{NO}^+} - \left(\frac{\text{NO}^+}{\text{NO}_2^+}\right) F_{\text{N}_2\text{O}_4^+}^{\text{NO}_2^+} \right) \quad (4.5)$$

Further rearrangement yields the desired ratio

$$\frac{\text{NO}_2}{\text{N}_2\text{O}_4} = 2.08 \frac{(\text{NO}^+/\text{NO}_2^+) F_{\text{N}_2\text{O}_4^+}^{\text{NO}_2^+} - F_{\text{N}_2\text{O}_4^+}^{\text{NO}^+}}{F_{\text{NO}_2^+}^{\text{NO}^+} - (\text{NO}^+/\text{NO}_2^+) F_{\text{NO}_2^+}^{\text{NO}_2^+}} \quad (4.6)$$

where $\sigma_{\text{N}_2\text{O}_4}^{\text{ion}}/\sigma_{\text{NO}_2}^{\text{ion}} = 2.08$ has been used (Table 4.2). Equation 4.6 can be used to obtain relative NO_2 and N_2O_4 concentrations when NO and O are in low enough concentration to justify ignoring them.

The single-species mass spectra presented in Figures 4.3a and 4.3d were used to obtain values for the four F -factors in Equation 4.6. Values of $\text{NO}^+/\text{NO}_2^+$ vary slightly at late times from one extraction to the next; their average value is 0.95. When these numbers are used with Equation 4.6, it is found that late times in the temporal profiles are dominated by N_2O_4 . The $\text{NO}_2/\text{N}_2\text{O}_4$ ratios obtained using Equation 4.6 fluctuate around 0.2. This result is robust from one profile to the next, including later extraction times than the longest times in Figure 4.7a. This trend is also evident from visual inspection of the temporal profiles.

4.1.3 Fourier-transform infrared spectra of amorphous and crystalline ice

To detect morphological changes in amorphous solid water due to thermal processing, 720 L of water was deposited on the substrate and a Fourier-transform infrared spectrum was acquired (Fig. 4.4). The spectrum is consistent with others reported for vapor-deposited amorphous solid water [6–8]. The film was then heated to 140 K for 10 minutes; this showed no change in the Fourier-transform infrared spectrum. Mitterdorfer et al. (2014) used neutron scattering studies to show that heating amorphous solid water to 120–140 K causes the micropores to collapse to lamellae [9]. Given that no change was seen in the Fourier-transform infrared spectrum despite sufficient heating to collapse the pores, we conclude that any

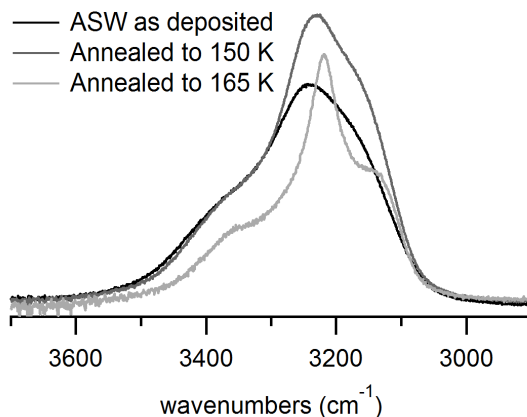


Figure 4.4: Transmission Fourier-transform infrared spectra of a 720-L film of amorphous solid water at 100 K; the same film heated to 150 K and recooled to 100 K; and the same film heated to 165 K and held at that temperature for 10 min, then recooled to 100 K. In both heating cycles some water desorbed, thus the spectra do not represent equivalent quantities of amorphous solid water.

changes seen in Fourier-transform infrared spectra of thermally processed amorphous solid water films are due solely to the nucleation of crystallites in the film, not due to pore collapse.

Using differential scanning calorimetry, Hallbrucker et al. (1989) found that an annealed, vapor-deposited amorphous solid water film heated at a rate of 30 K/min had a crystallization onset temperature of 150 K, with the exotherm centered at 165 K [10]. This is consistent with our results. The film was heated to 150 K and held at that temperature for 10 min; it was then recooled to 100 K and probed using Fourier-transform infrared spectroscopy. The Fourier-transform infrared spectrum showed an increase in signal (Fig. 4.4). Some material desorbed during this heating cycle, seen as an increase in the chamber pressure during heating. Although the shoulder around 3400 cm^{-1} overlaps exactly for the annealed and as-deposited films, the overlap is likely coincidental with regards to intensity, but indicates little to no change in this mode as a result of morphological change. Regardless, it is readily obvious that the profile of the peak as a whole undergoes substantial change.

Further heating of the same film to 165 K for 10 min desorbed a larger amount of material. The spectrum profile changes to a much sharper maximum peak, and two

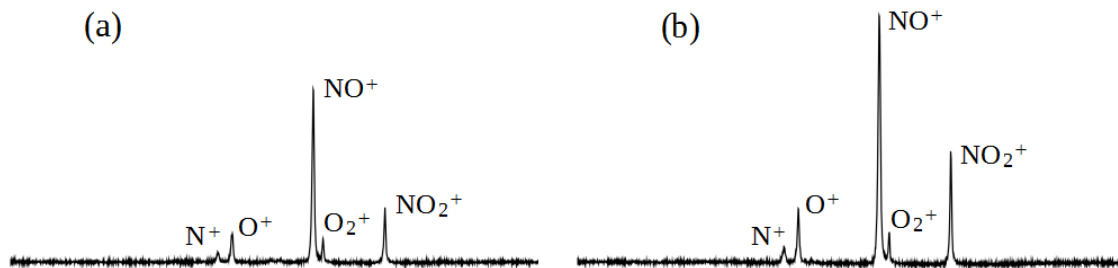


Figure 4.5: Mass spectra of exposed N_2O_4 subjected to focused 266-nm radiation (1 mJ); (a) no spacer between 80 L of N_2O_4 and MgO; (b) spacer of 180 L of $\text{H}_2\text{O}(\text{as})$ (see Fig. 4.7, upper left). Thermal insulation increased signal intensity.

shoulders have become quite pronounced (Fig. 4.4). The shoulder around 3400 cm^{-1} does not overlay the other two spectra, even when scaled accordingly. Further heating at 165 K desorbed more material, but did not change the profile of the spectrum. We can conclude that this spectrum represents a fully crystallized film, while the spectrum after heating to 150 K represents a partially crystallized film. Overall, the Fourier-transform infrared spectra show that we are indeed forming amorphous solid water, that pore collapse is not a detectable morphological change using Fourier-transform infrared spectroscopy, and that morphological changes with regards to crystallinity can be readily detected.

4.2 Irradiation of Exposed N_2O_4

Exposed layers of N_2O_4 , *i.e.*, where N_2O_4 is the topmost layer of the sample, were irradiated with varied amounts of amorphous solid water deposited beneath. The presence of a layer separating the N_2O_4 from the MgO substrate increases the resulting time-of-flight signal. Figure 4.5 illustrates the role of the water spacer between MgO and N_2O_4 insofar as increasing signal intensity.

To gain insight to this result, heat transfer calculations were done in COMSOL. A model was constructed with dimensions equivalent to a layer of 80 L of NO_2 deposited directly atop the MgO substrate or with an $\text{H}_2\text{O}(\text{as})$ spacer between them. The

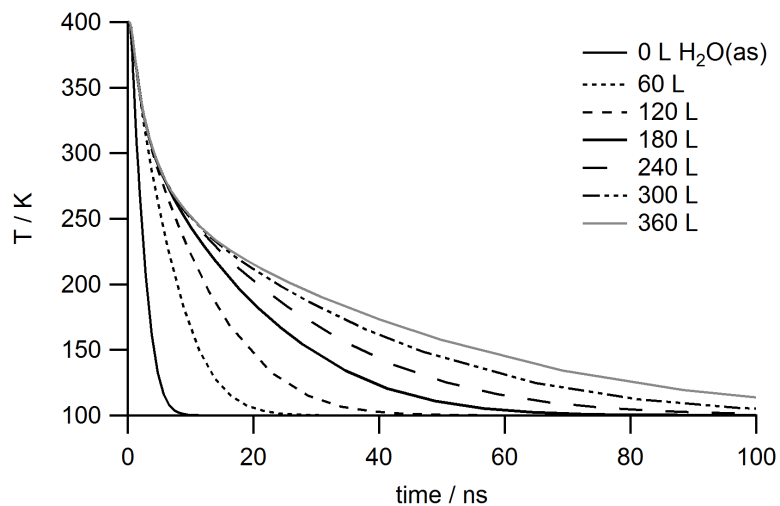


Figure 4.6: Evolution over time of the maximum temperature of a 50-nm film of N_2O_4 atop 0–360 L of $\text{H}_2\text{O}(\text{as})$ on a MgO substrate. At $t = 0$, the MgO and $\text{H}_2\text{O}(\text{as})$ are at 100 K, and the N_2O_4 is at 400 K. Increasing the thickness of the $\text{H}_2\text{O}(\text{as})$ layer decreases the rate of cooling of the N_2O_4 layer.

$\text{H}_2\text{O}(\text{as})$ and/or MgO boundary was given an initial temperature of 100 K, and the N_2O_4 layer was initially 400 K. The system was then allowed to evolve in time for 100 ns. As previously stated, phase change and material desorption were neglected; in this model, heat exchange only occurs via conduction. The maximum temperature of the N_2O_4 was monitored as it decreased from 400 K, using a spacer of 0–360 L $\text{H}_2\text{O}(\text{as})$ in increments of 60 L. Without an $\text{H}_2\text{O}(\text{as})$ spacer, the temperature drops to 100 K within 10 ns (Fig. 4.6). A 60-L spacer has a pronounced effect: it takes ~ 25 ns for the film to cool. As the spacer layer is increased, it takes longer and longer for the N_2O_4 to cool.

Recall that N_2O_4 and $\text{H}_2\text{O}(\text{as})$ have both been modeled with a constant thermal conductivity of $1 \text{ W/m}\cdot\text{K}$; the difference in temperature across the $\text{N}_2\text{O}_4/\text{H}_2\text{O}(\text{as})$ boundary is due to their different heat capacities and densities, and the heat flux is proportional to the temperature gradient. On the other hand, MgO(100) has a thermal conductivity more than two orders of magnitude larger. As we increase the thickness of the spacer layer, there are three major effects: (1) the average

temperature that the $\text{H}_2\text{O}(\text{as})$ layer reaches decreases, because the same amount of thermal energy has dissipated into an increasingly large quantity of $\text{H}_2\text{O}(\text{as})$; (2) it takes longer for a temperature change to occur at the $\text{H}_2\text{O}(\text{as})/\text{MgO}$ boundary because the distance between the N_2O_4 layer and MgO is increased; and (3) because the $\text{H}_2\text{O}(\text{as})$ does not reach as high of a temperature, the temperature gradient across the $\text{H}_2\text{O}(\text{as})/\text{MgO}$ boundary decreases and in turn decreases the heat flux.

The initial N_2O_4 temperature (400 K) was chosen somewhat arbitrarily at the beginning of these calculations. However, a range of initial temperatures was explored and it is noteworthy that in all cases, H_2O spacers greater than 180 L result in a decrease in temperature, to one-half the initial difference between the temperature of the N_2O_4 film and the 100-K MgO substrate, in about 10 ns. That is, for $\text{H}_2\text{O}(\text{as})$ -spacers above 180 L, the N_2O_4 -cooling rates are identical for the first 10 ns.

We note that pronounced increases in time-of-flight signal occur as the $\text{H}_2\text{O}(\text{as})$ film is increased from 0 to 180 L. Above 180 L, there is little to no increase in signal. When we consider the results depicted in Figure 4.6, this can be rationalized as the point where the high rate of heat transfer across the $\text{N}_2\text{O}_4/\text{MgO}$ or $\text{H}_2\text{O}(\text{as})/\text{MgO}$ boundary starts to be counteracted by the smaller temperature gradient at the boundary and by the distance from the N_2O_4 layer to the high-thermal conductivity MgO substrate.

Again, it should be emphasized that this trend was seen across a range of initial N_2O_4 temperatures. Yet, given the limitations of this model (*e.g.*, temperature-independent densities and thermal conductivities; neglect of phase change or desorption) this connection is likely a coincidence. This may, however, be an interesting phenomenon to explore in future calculations.

4.2.1 Temporal evolution of the plume

180 L of H₂O covered by 80 L of N₂O₄ was irradiated with a 1-mJ, 266-nm pulse, yielding a broad temporal profile and individual mass spectra. Figure 4.7 shows a typical single-shot (9-point average) result that characterizes exposed N₂O₄. The variation of the NO⁺/NO₂⁺ ratio across the temporal profile depends on N₂O₄ and H₂O spacer layer thicknesses, whereas the overall profile shape is independent of these details. In the present study, the shape of the temporal profile serves as an indicator of exposed, as opposed to buried, N₂O₄.

We can see from all spectra in Figure 4.7 that no H₂O⁺ or OH⁺ is detected. This result is robust, and indicates that no water crosses the layer of N₂O₄. This is true even after many pulses and the evident depletion of the N₂O₄ layer. Fourier-transform infrared spectroscopy, likewise, shows no change. Both of these results are true whether H₂O(as) or D₂O(as) is used, and under all conditions used for the studies presented in this work.

With regards to time-of-flight temporal profiles, the laser pulse is incident at $t = 0$. Due to the 2.5 cm distance between the surface and the center of the ionizing region of the time-of-flight mass spectrometer, there is a delay before material at the plume front can be detected. Reliable mass spectra are usually detected beginning at $t = 20$ μ s; this can be seen in Figure 4.7. The ionizing pulse has a duration of 7 μ s, followed by a 3- μ s extraction; the 10- μ s time-of-flight intervals commence with the extraction pulse. As a crude estimation, material which arrives at the detector between $t = 20$ and $t = 30$ μ s underwent ionization during $t = 13$ and $t = 20$ μ s. Given this range, the first detected molecules left the surface with an estimated speed of $1.6 \pm 3 \times 10^5$ cm/s. This estimate becomes much more crude when one considers that the ionizing region is 12.5 mm. Despite this, such estimates can provide insight.

The kinetic energy of a NO₂ molecule whose speed is $\sim 1.2 \times 10^5$ cm/s is 2800 cm⁻¹.

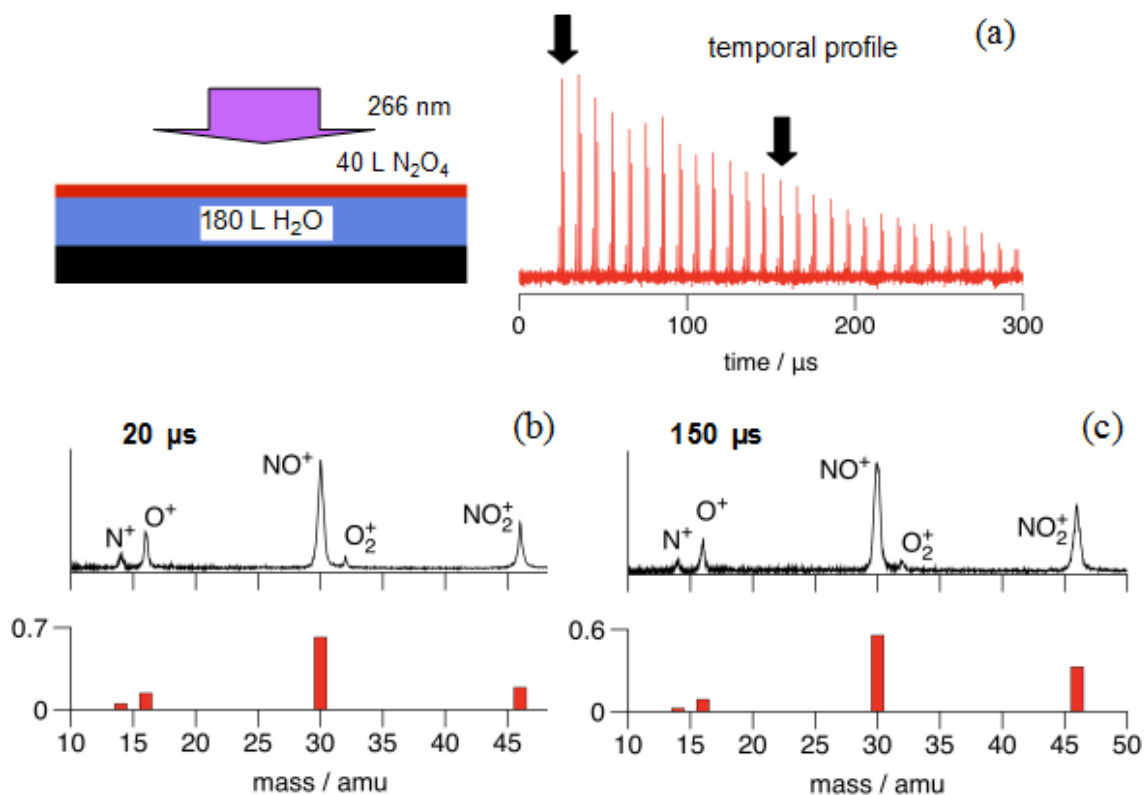


Figure 4.7: Extractions from the temporal profile at 20 and 150 μs (black arrows in panel a) yielding the mass spectra shown in panels b and c, respectively. The film composition is depicted in the upper left. At 20 μs , neutral NO_2 plays a significant role; its role is diminished at later times.

On the other hand, the speed of a species that leaves the surface at $t = 0$ and arrives at a point 2.5 cm from the surface 300 μs later (the last extraction in the temporal profile) is 8×10^3 cm/s. Were NO_2 and N_2O_4 to leave the surface at $t = 0$, the 300 μs arrival time would correspond to kinetic energies of 12.5 and 25 cm^{-1} , respectively. Later we will see that NO_2 most likely arises from photodissociation of gaseous N_2O_4 . The low energy of 25 cm^{-1} can be rationalized as being in the tail of a warm distribution. For example, the amount of signal in the 300 μs extraction is of order 1% of the total signal for the interval 0–300 μs .

4.3 Single-Pulse Results from Multi-Layer Samples

Samples such as those in Figure 4.11 are composed of a lower layer of $\text{H}_2\text{O}(\text{as})$ or $\text{D}_2\text{O}(\text{as})$, an N_2O_4 layer (typically from 80 L of NO_2), and a range of amorphous solid water (H_2O and D_2O , either separately or in adjacent layers) upper layer thickness. Deposition is carried out near 100 K. It is possible that reaction takes place at interfaces between N_2O_4 and amorphous solid water yielding, for example, HNO_2 and HNO_3 [11, 12]. The extent of such reaction is not known; however, no signature of these molecules was seen in Fourier-transform infrared spectra. In addition, the porous nature of amorphous solid water accommodates penetration. These caveats notwithstanding, N_2O_4 is contained in a reasonably well-defined layer.

Figure 4.8 shows typical temporal profiles and individual spectra for films with buried N_2O_4 . Unless otherwise stated, ~ 1 mJ pulses were used. Rows 1–3 correspond to $\text{H}_2\text{O}(\text{as})$ upper layers of 180, 720, and 1440 L; the ordinate scales are the same. The profile in row 1 shows that H_2O monomer arrives at the ionization region in two groups. On the other hand, NO_2^+ and NO^+ have profiles that differ from that of H_2O . The NO_2^+ peak arises from NO_2 and N_2O_4 , whereas the NO^+ peak arises from NO , NO_2 , and N_2O_4 . The NO contribution is modest, most likely arising from NO_2

Table 4.3: Peak areas and $R_N = \text{NO}^+/\text{NO}_2^+$ values for the spectra in Figure 4.8

pulse 1 (Fig. 4.8)	amu			R_N
	18	30	46	
a	1.92	1.27	0.95	1.34
b	1.86	0.40	0.40	1.00
c	1.86	1.14	1.01	1.13
d	2.82	0.49	0.44	1.11
e	2.64	0.89	0.95	0.94
f	2.75	0.38	0.45	0.84

photolysis. Hereafter, we shall refer to the combination of NO, NO₂, and N₂O₄ as N_xO_y, and we shall refer to the NO⁺/NO₂⁺ ratio as R_N . The lumpy features in the water temporal profiles vary from one first-shot profile to the next. What is robust, however, is that lumpy features are always present, as seen also in Figure 4.10.

The values of R_N for the Figure 4.8 spectra differ from one another, but none is close to the NO₂ value of 3.1 (Figure 4.3a). The largest is for row 1, spectrum a, which has $R_N = 1.34$ (Table 4.3). Many spectra have been examined, both within the profiles used in Figure 4.8, and in numerous other first-pulse profiles recorded over roughly a year. R_N is close to unity in essentially all of them, except at the shortest extraction times. Figure 4.9 shows R_N values for each extraction in the Figure 4.8 profiles.

Referring to Figure 4.3d, the R_N value of 0.9 for N₂O₄ is close to the first-pulse ratios of Figure 4.8 (see Figure 4.9), except for the first two extractions, which have low S/N. This differs markedly from the NO₂ value of 3.1. We conclude that N₂O₄ is the dominant N_xO_y constituent under the conditions of Figure 4.8. Row 2 of Figure 4.8 shows data for an upper amorphous solid water layer of 720 L. In light of the factor of two increase in upper amorphous solid water thickness, the amount of

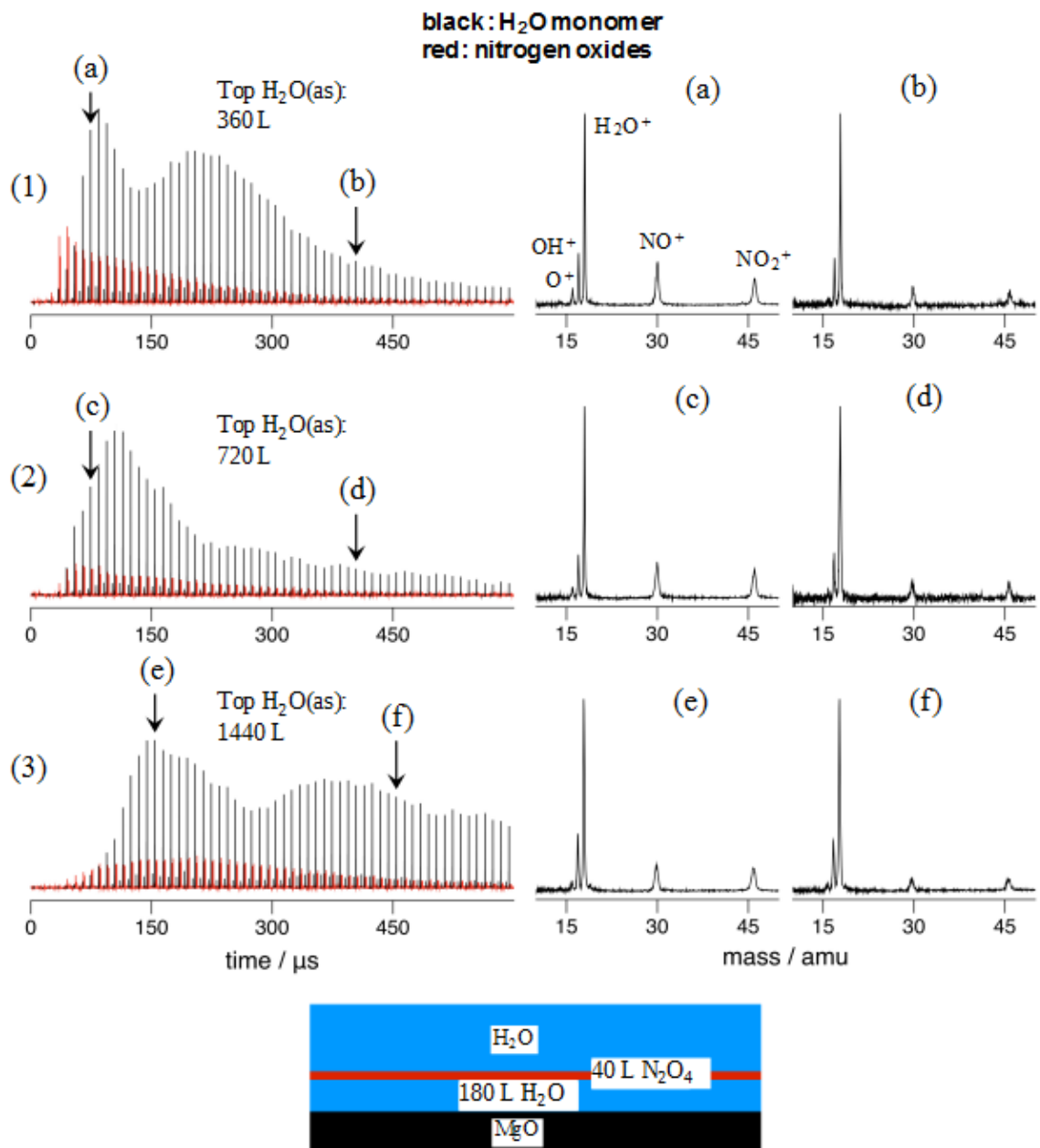


Figure 4.8: Temporal profiles and mass spectra for upper H₂O(as) layer thickness: (1) 360 L, (2) 720 L, and (3) 1440 L of H₂O(as) over 40 L N₂O₄ (from 80 L of NO₂) and 180 L of D₂O(as). Each profile is the average of nine individual first-pulse profiles (1 mJ, 266 nm). Red corresponds to NO⁺ and NO₂⁺. Black corresponds to H₂O⁺, OH⁺, and H⁺. The temporal profiles in rows (1)–(3) are on the same ordinate scale. The lower amorphous solid water layer is 180 L of D₂O, and the N₂O₄ layer is 40 L (80 L of NO₂). Mass spectra are shown in each row for the respective extractions in the temporal profiles indicated with vertical arrows. Sample composition is shown at the bottom.

Table 4.4: Peak areas and R_N values for the spectra in Figure 4.11

pulse 2 (Fig. 4.11)	amu			R_N
	18	30	46	
a	0.18	5.35	1.97	2.72
b	2.12	1.18	0.71	1.64
c	0.42	5.30	1.70	3.12
d	2.39	2.46	1.38	1.78
e	0.00	5.51	1.80	3.06
f	3.45	1.14	0.91	1.25

H₂O does not differ much from row 1. The upper amorphous solid water thickness for row 3 is four times that of row 1, and a propensity toward longer times is evident. The amount of H₂O that arrives at the ionization region is actually larger than for rows 1 or 2. One might have expected additional thickness to inhibit material from entering vacuum, *e.g.*, because of increased heat capacity.

4.3.1 Temporal profiles

There is no possibility that the majority of the H₂O detected mass spectrometrically leaves the film at $t = 0$ and travels without collision to the ionization region. For example, a transit time τ of 200 μs and $v = d/\tau$, with $d = 2.5$ cm, yields kinetic energy of 10 cm^{-1} . H₂O signal beyond 200 μs would correspond to kinetic energies < 10 cm^{-1} . Figure 4.10 shows significant signal out to 1200 μs , which corresponds to kinetic energy of 0.3 cm^{-1} . In Section 4.8 it is shown that the upper amorphous solid water layer is too thick to accommodate sublimation; H₂O that enters vacuum does so via fissures. The lumpy character is in accord with molecules undergoing collisions as they emerge from the fissures.

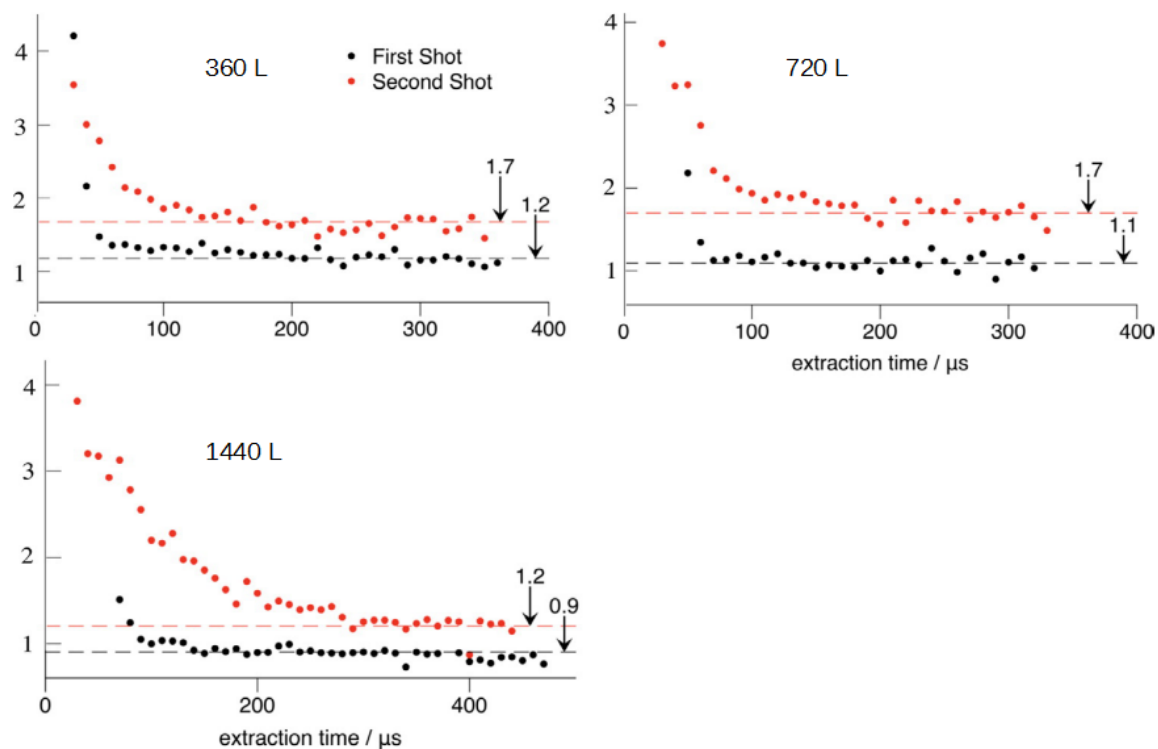


Figure 4.9: R_N values for a large number of extractions: First-pulse R_N values (black) settle down after the first few extractions to values of order unity. Second-pulse R_N values (red) are consistent with the presence of a significant amount of N_2O_4 in the surface region.

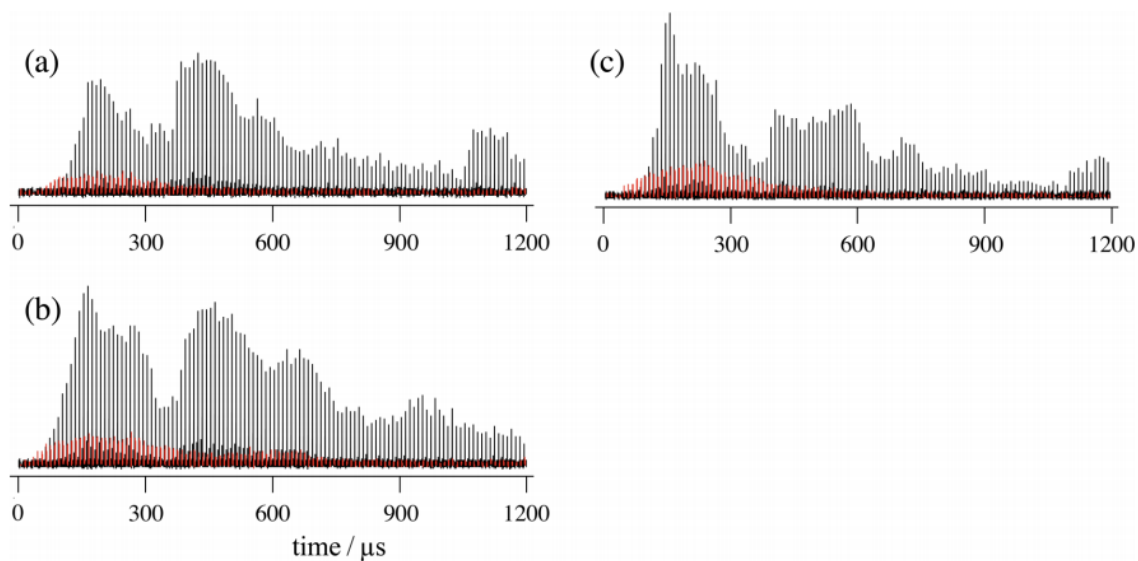


Figure 4.10: Temporal profiles of desorbed material for different spots on 1440 L of $H_2O(as)$ over a 40-L N_2O_4 film (from 80 L of NO_2) and a 180-L $H_2O(as)$ thermal buffer layer: Each panel is a single, first-pulse temporal profile. Red corresponds to NO^+ and NO_2^+ , black to H_2O^+ .

4.4 Subsequent Pulses Incident on the Same Spot

The first pulse to interact with a sample alters it significantly. Thus, we studied effects brought about by subsequent pulses, albeit one at a time. Figure 11 shows profiles and spectra for second pulses incident on the same spots as were the first. Results from all nine spots are summed. A striking effect is seen in the N_xO_y profiles. The R_N values obtained for each of them (Tables 4.3, 4.4 and Figure 4.9) resemble those of exposed N_2O_4 (Fig. 4.7). This supports a model in which robust fissures are formed with the first pulse, through which N_xO_y can be transported to the surface region with subsequent pulses. The R_N values for the earliest extractions in each profile indicate that NO_2 photoproduct reaches the mass spectrometer, confirming that N_2O_4 is already present at the surface. In light of the role played by 266-nm photodissociation of N_2O_4 , it is not feasible to determine quantitatively the respective amounts of gas phase N_2O_4 and NO_2 .

4.5 Fissure Growth in Stages

The results presented in Sections 4.3 and 4.8.3 indicate the formation of fissures through which material passes on its way to vacuum. This process depends on laser fluence. With fluence lowered by an order of magnitude (at constant energy), the first pulse yielded no signal, whereas a second (or sometimes third) pulse yielded respectable signal. Subsequent pulses yielded significant signal, and the N_xO_y temporal profiles displayed the characteristic shape and mass spectra of exposed N_2O_4 , as in Figure 4.7. Apparently the first pulse pushes fluid toward vacuum, but with insufficient thrust for it to exit the film. Competition between moving toward vacuum versus depositing on fissure walls favors the latter to the extent that

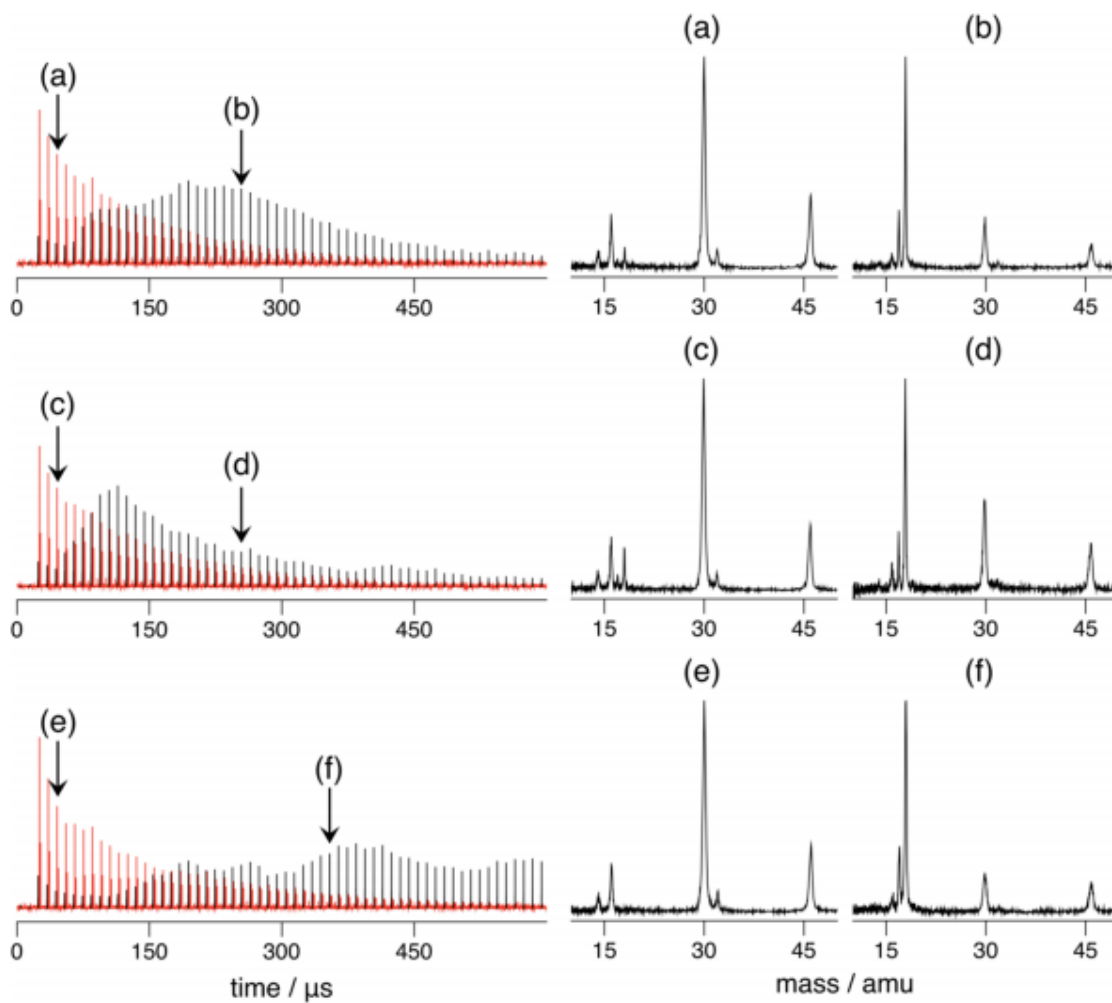


Figure 4.11: Temporal profiles are shown for a second 1-mJ laser pulse at the same locations as in Figure 4.8: Each profile is the sum of profiles from 9 spots. Red corresponds to NO^+ and NO_2^+ , black to H_2O . The ordinate scale is the same as in Figure 4.8. Mass spectra are shown on the right for the respective extractions in the temporal profiles indicated with vertical arrows on the left.

nothing exits the film.

The next pulse heats the N_2O_4 reservoir plus the N_2O_4 -rich material trapped in incipient fissures, resulting in material entering vacuum. Sometimes a third pulse is required. This behavior is in accord with the model discussed in Section 4.8.

4.6 Isotope Scrambling — Scraping the Walls

H/D isotope exchange (scrambling) sheds light on the mechanism of material transport. Figure 4.12 shows an example of facile H/D exchange that takes place when layers of $\text{D}_2\text{O}(\text{as})$ and $\text{H}_2\text{O}(\text{as})$ are placed atop N_2O_4 and the sample is irradiated. The samples were prepared at 100 K, at which temperature there is no exchange [13]. This was verified using Fourier-transform infrared spectroscopy.

The mass spectra shown in Figures 4.12a and 4.12b indicate that extensive exchange has occurred during the heated fluid's transit through the fissures. The upper layer is composed of 120 L each of $\text{D}_2\text{O}(\text{as})$ and $\text{H}_2\text{O}(\text{as})$: (a) $\text{D}_2\text{O}(\text{as})$ over $\text{H}_2\text{O}(\text{as})$, and (b) $\text{H}_2\text{O}(\text{as})$ over $\text{D}_2\text{O}(\text{as})$. This corresponds to an upper amorphous solid water thickness of roughly 150 nm, and exchange can only occur in the top half. This facile exchange underscores the heated nature of the fluid passing through the fissures and efficient mixing of H_2O and D_2O . The extent to which traces (a) and (b) resemble one another is striking. These data indicate that water is removed by the heated fluid from the fissure walls throughout the length of the fissure. Trace (c) is a check. It shows that there is little isotope scrambling due to impurity H_2O when 300 K gaseous D_2O is introduced into the chamber.

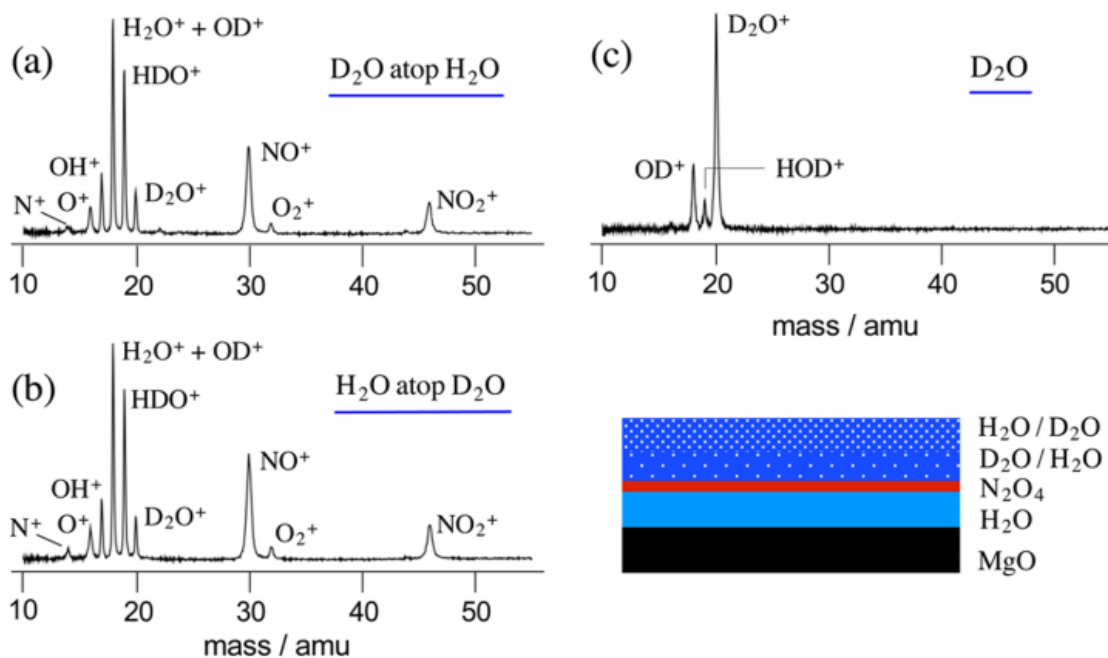


Figure 4.12: (a) and (b) show spectra for extractions at 50–60 μ s, following first-pulse 266-nm irradiation (1.5 mJ) for samples that have 40 L of N₂O₄ atop a 180 L H₂O(as) spacer and alternating H₂O(as) and D₂O(as) upper layers. In (a), the upper amorphous solid water layer has 120 L of D₂O(as) atop 120 L of H₂O(as), and in (b) this is reversed. In (c), a spectrum of 300-K gaseous D₂O recorded the same day shows only modest HDO contamination.

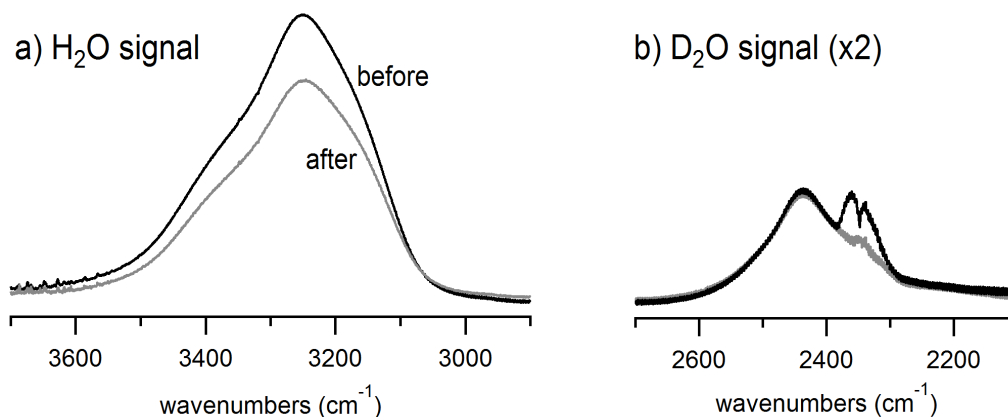


Figure 4.13: Transmission Fourier-transform infrared spectra of a multilayer film (40 L of N_2O_4 deposited over 180 L of $\text{D}_2\text{O}(\text{as})$, with 720 L of $\text{H}_2\text{O}(\text{as})$ on top) at 100 K, taken following deposition and after 70 pulses of 266 nm radiation. The peaks between 2400-2300 cm^{-1} are due to changes in background CO_2 .

4.7 Fourier-Transform Infrared Spectroscopic Results

It is desirable to record the production and removal of species under single-pulse conditions by using Fourier-transform infrared spectroscopy. This has not yet been achieved because of insufficient fluence and the limited spectral range of the InSb detector. However, we have recorded Fourier-transform infrared spectra that demonstrate water removal from the upper amorphous solid water layer. As mentioned earlier, the ($\text{D}_2\text{O}(\text{as})$) spacer between MgO and N_2O_4 is robust. Not once has it crossed the N_2O_4 layer.

Referring to Figure 4.13, 14% of the upper amorphous solid water layer has been removed by irradiation with 70 pulses. The fluence is at least an order of magnitude lower than that used in the time-of-flight mass spectrometry studies. The amorphous nature of the water is unchanged, as evidenced by a comparison of the spectra in Figures 4.13 to those in Figure 4.4.

4.8 Discussion

The data, together with a few straightforward estimates, led us to propose a model for material transport from the N_2O_4 layer to vacuum via fissures. Before starting the experiments, we expected that an amorphous solid water upper layer of several tens of monolayers would result in a modest amount of material entering the gas phase, and several hundred monolayers would result in virtually nothing entering the gas phase. In fact, the thickest amorphous solid water layer used, 1440 L, yielded the largest amount of released material.

4.8.1 Observables

Before discussing the model, it is useful to summarize the experimental observations. First, the transport of material to vacuum via pulsed heating of buried layers differs qualitatively from that of pulsed heating of samples of uniform composition. For example, small protonated water clusters have not been observed in any of the mass spectra recorded in the present study, whereas they are readily observed when exciting $\text{H}_2\text{O}(\text{as})/\text{CO}_2$ mixtures using focused infrared radiation in the OH-stretch region [14]. This underscores the fact that the mechanisms for the transport of material to vacuum differ for these two cases. Second, the phenomena described here and the so-called “volcano peak,” where embedded atoms and molecules are ejected from amorphous solid water upon heating, are different [15]. The latter involves homogeneous thermal heating of the film and the abrupt expulsion of guest molecules at a temperature corresponding to the phase transition to cubic ice. Our experiments involve selective pulsed heating of an embedded layer covered by a relatively thick amorphous solid water layer, followed by transport of

the heated fluid to vacuum.

The 266-nm photolysis of gaseous N_2O_4 yields NO_2 with translational and internal energy. In the dense environments of the present experiments, recombination takes place, and nascent excitations evolve to heat on a time scale that is much shorter than the pulse duration. The net effect is heating the N_2O_4 layer and its surroundings.

Molecules detected by time-of-flight mass spectrometry include N_2O_4 , NO_2 , NO , H_2O , and O_2 . When the upper layer is composed of $\text{H}_2\text{O}(\text{as})$ and $\text{D}_2\text{O}(\text{as})$, HDO and D_2O are also detected. The amount of NO is modest, and it shall not be considered further. Using D_2O to insulate N_2O_4 from the MgO substrate distinguishes this layer spectrally from H_2O atop the N_2O_4 . Molecules in the insulator layer never pass through the N_2O_4 .

Temporal profiles and mass spectra obtained with amorphous solid water-covered versus exposed N_2O_4 are revealing. For the former, the first pulse liberates mainly N_2O_4 . This manifests as a much smaller R_N value than for NO_2 (0.9 versus 3.1). On the other hand, a signature of exposed N_2O_4 is the presence of gas phase NO_2 photoproduct, and therefore larger R_N values (Figure 4.7).

For $\text{H}_2\text{O}(\text{as})$ -covered N_2O_4 , the R_N values for second, third, etc. pulses are larger than that of the first pulse. This is consistent with N_2O_4 being present at/near the surface due to the first pulse, with subsequent pulses displaying signatures of exposed N_2O_4 . For example, note the “pulse 2” entries in Table 4.4. In the same vein, under low-fluence conditions additional pulses are required to bring N_2O_4 to vacuum. Also, the fact that facile H/D exchange occurs when the upper layer is composed of $\text{H}_2\text{O}(\text{as})$ and $\text{D}_2\text{O}(\text{as})$ indicates that water that reaches the mass spectrometer has been entrained by heated material moving through fissures.

The above observations are consistent with material reaching vacuum via fissures. For all practical purposes, it is impossible for material to wend its way diffusively through porous amorphous solid water without freezing. Aspects of the model are

described below, starting with a phenomenon that caught our attention from the start: exceptionally long time scales for material arriving at the ionization region.

4.8.2 *Time scales*

Temporal profiles proved to be central to establishing transport mechanisms. Their time scales often exceeded 1 ms, and this plus their lumpy character surprised us. Experiments were repeated and scrutinized over many months, with widely varying conditions. We found that the main character is robust. Lumps differ from one profile to the next, but the profiles always display lumpy character, especially at long times. It is a signature of the processes whereby material enters vacuum.

As mentioned earlier, it is not feasible that H₂O molecules leave the surface at $t = 0$ and arrive 1200 μs later at the ionization region without undergoing collisions. Were collision-free transit to commence at $t = 0$, the kinetic energy for a 1200 μs arrival time would be a minuscule 0.33 cm^{-1} . Even for an arrival time of 150 μs , it would be only 21 cm^{-1} . Such low kinetic energies cannot be assigned to the tail of a distribution. For example, in Figure 4.10a, which is a typical spectrum, only $\sim 4\%$ of the signal lies within 150 μs .

These observations are consistent with the majority of the water molecules that leave the film at $t = 0$ arriving at the ionization region after undergoing collisions. Delayed departure after the laser firing would require at least hundreds of microseconds. The region emitting the molecules would have to have lost thermal contact with the rest of the film, and to an incredible extent. We deem this unlikely on the basis of the heat transfer calculations described below. We also deem it unlikely that large chunks of water are liberated that eventually reach the ionization region. No cluster ions were observed, though they are readily observed using other excitation methods [14]. The large-chunks mechanism is also inconsistent with the

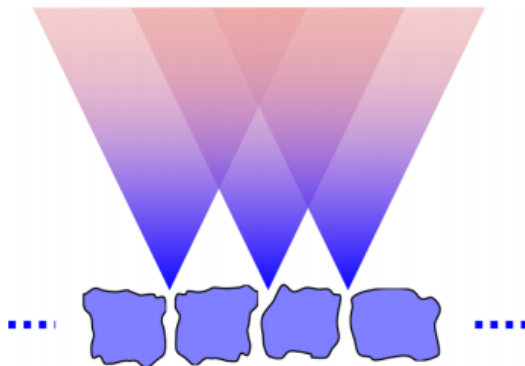


Figure 4.14: Cartoon illustrating how fissure effluents might interact, creating a turbulent flow of material.

efficient H/D exchange observed using layered samples. We conclude that the fissures and their effluents are key to understanding the long-time signals.

4.8.3 Fissures

The data are consistent with porous amorphous solid water undergoing morphological change when subjected to temperature and pressure gradients. For a laser beam diameter of 0.3 mm and a film thickness of 300 nm, the diameter-to-thickness ratio is 10^3 . Because amorphous solid water must maintain its macroscopic column density, there is a propensity to develop fissures. Heated fluid is composed of N_xO_y and entrained water, and its upward thrust also promotes fissure formation. The robust nature of large fissures is supported by the second, third, etc. pulse data.

Fissures that yield signal probably involve a reasonably direct path from the N_2O_4 layer to vacuum. Material cannot follow a trajectory that twists and turns without freezing. Were an amorphous solid water of density 0.8 g/cm^3 to convert completely to crystalline ice and vertical fissures, the fissures would account for roughly 13% of the surface area. This is not achieved, as evidenced by the large number of pulses needed to deplete the N_2O_4 reservoir.

The effluent from a given fissure collides with effluents from nearby fissures (Fig. 4.14). Regardless of angular spread, direction of main flow, or fissure shape, there is too much opening per unit area to not have collisions above the film surface, where the density of ejected material is high. It is not feasible that low-density gas travels through the fissures, as it would deposit on the walls. The material that makes its way to vacuum is liquid and/or high-density gas. As explained below, rapid cooling sets in near the film-vacuum interface following cessation of the 10-ns pulse. Amorphous solid water in this region cannot be heated to any significant degree through diffusive heat transfer.

Collisions between effluents from different fissures will result in a turbulent flow, deflecting species in many directions. This gives rise to collisions with metal surfaces (such as components of the time-of-flight mass spectrometer) and bouncing around within the region bounded by metal surfaces. This results in a spatially inhomogeneous density in the extraction region. We propose that this is responsible for the lumpy character at long times.

The picture that emerges is that pulsed heating creates pressure and temperature gradients, resulting in fissures that connect the N_2O_4 reservoir to vacuum. Heated N_xO_y removes water from fissure walls and carries it along. The pulse duration is long enough to heat N_xO_y as it passes through fissures, maintaining a warm fluid. The radiation also photodissociates N_2O_4 that has entered the gas phase prior to the pulse's termination.

4.8.4 *Material Transport*

The high-density environment converts absorbed 266-nm radiation to heat, and temperature and pressure gradients initiate morphological change in the amorphous solid water. Column densities are maintained over large horizontal length scales,

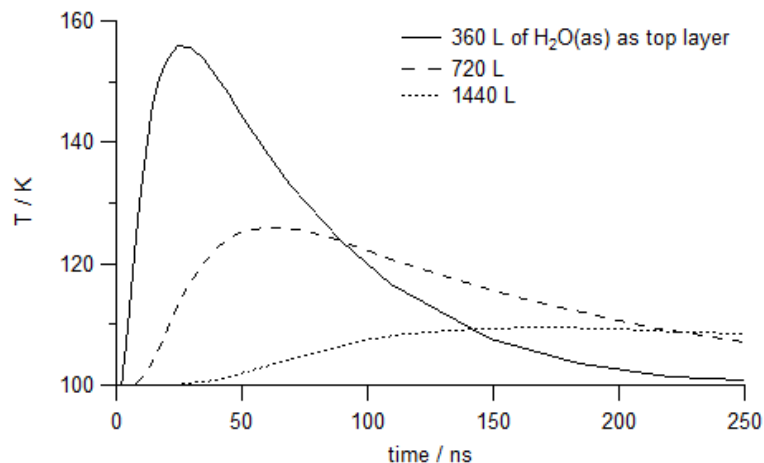


Figure 4.15: Surface temperature of 360, 720, and 1440-L films of $\text{H}_2\text{O}(\text{as})$ over 40 L N_2O_4 and 180 L $\text{H}_2\text{O}(\text{as})$ after heating the N_2O_4 to 400 K.

whereas fissures form on smaller scales. Many are wide enough to enable fluid to reach vacuum with the first pulse. Such fissures are expected to be robust.

Heat flow in layered films was calculated using the program COMSOL Multiphysics. The goal was to judge qualitatively how films cool following pulsed excitation, particularly near the vacuum interface. Thermal contact between layers was assumed, and phase changes and thermal desorption were neglected. The values for density, heat capacity, and thermal conductivity that were justified in Section 3.6 were used (see Table 3.1).

Figure 4.15 shows representative plots of calculated surface temperature versus time for starting temperatures of 400 K for N_2O_4 and 100 K for MgO and $\text{H}_2\text{O}(\text{as})$. For 1440 L of $\text{H}_2\text{O}(\text{as})$, the peak temperature is reached at 170 ns, with no temperature increase at 10 ns. For 720 L the peak is at 60 ns, again with no temperature increase at 10 ns. For 360 L the peak is at 30 ns, with an increase of 20 K at 10 ns.

In the experiments, material that enters vacuum removes heat, and the amorphous solid water insulation layer absorbs heated N_2O_4 thereby improving thermal conductivity to the MgO substrate. Moreover, no discernible degree of crystallinity has ever been observed in Fourier-transform infrared spectra in either

the insulation layer or the upper amorphous solid water layer following irradiation. Upon cessation of the 10-ns pulse, material in fissures begins to cool. In light of its proximity to surrounding amorphous solid water, it quickly freezes. On this basis, we estimate that for a 1440-L layer material passes through fissures with a minimum speed of order 10^2 m/s.

The above picture is consistent with the data. Even with 1440 L of $\text{H}_2\text{O}(\text{as})$, a large amount of N_2O_4 enters vacuum with the first pulse, which would not happen without it passing through fissures as a fluid. The first pulse deposits N_2O_4 at/near the surface. Referring to Figure 11, there is striking similarity between the N_xO_y signals observed for the second pulses and those associated with exposed N_2O_4 . This correspondence persists for subsequent pulses up to the largest number used (~ 70). This supports the proposed model, in which repeated photoexcitation pumps N_2O_4 from its reservoir to the surface through robust fissures.

Another result that is consistent with the model is that when the fluence is lowered to below the threshold for material release into vacuum, it takes two or more pulses to observe N_xO_y signals. When the heated fluid lacks the thrust necessary to enter vacuum, cooling traps material and its release to vacuum awaits the next pulse. The model also reconciles the facile H/D exchange that takes place when using $\text{H}_2\text{O}(\text{as})/\text{D}_2\text{O}(\text{as})$ layers. Exchange was efficient regardless of whether the $\text{D}_2\text{O}(\text{as})$ layer is above or below the $\text{H}_2\text{O}(\text{as})$ layer. These data demonstrate that water is stripped from fissure walls throughout transport. It will be informative to examine exchange using pulses of ~ 20 ps duration, as this separates (temporally) photoexcitation from transport.

4.9 Chapter 4 References

- [1] Linstrom, P. J.; Mallard, W. G. *NIST Chemistry WebBook, NIST Standard Reference Database Number 69*; National Institute of Standards and Technology: Gaithersburg MD, 2014.
- [2] Hisatsune, I. C. *J. Phys. Chem.* **1961**, *1319*, 2249–2253.
- [3] Russ, F. *Zeitschrift für Phys. Chemie* **1914**, *82*, 217–222.
- [4] Rieley, H.; McMurray, D. P.; Haqb, S. *J. Chem. Soc. Faraday Trans.* **1996**, *92*, 933–939.
- [5] Kim, Y.-K.; Rudd, M. E. *Phys. Rev. A* **1994**, *50*, 3954–3967.
- [6] Bergren, M. S.; Schuh, D.; Sceats, M. G.; Rice, S. A. *J. Chem. Phys.* **1978**, *69*, 3477–3482.
- [7] Hagen, W.; Tielens, A. G. G. M.; Greenberg, J. M. *Chem. Phys.* **1981**, *56*, 367–379.
- [8] Manca, C.; Martin, C.; Roubin, P. *Chem. Phys.* **2004**, *300*, 53–62.
- [9] Mitterdorfer, C.; Bauer, M.; Youngs, T. G. A.; Bowron, D. T.; Hill, C. R.; Fraser, H. J.; Finney, J. L.; Loerting, T. *Phys. Chem. Chem. Phys.* **2014**, *16*, 16013–16020.
- [10] Hallbrucker, A.; Mayer, E.; Johari, G. P. *J. Phys. Chem.* **1989**, *93*, 4986–4990.
- [11] Kim, S. K.; Kang, H. *J. Phys. Chem. Lett.* **2010**, *1*, 3085–3089.
- [12] Lignell, H.; Varner, M. E.; Finlayson-Pitts, B. J.; Gerber, R. B. *Chem. Phys.* **2012**, *405*, 52–59.
- [13] Park, S.-C.; Jung, K.-H.; Kang, H. *J. Chem. Phys.* **2004**, *121*, 2765–74.
- [14] Rebolledo-Mayoral, O. R.; Stomberg, J.; McKean, S.; Reisler, H.; Wittig, C. *J. Phys. Chem. C* **2012**, *116*, 563–569.
- [15] May, R. A.; Smith, R. S.; Kay, B. D. *J. Phys. Chem. Lett.* **2012**, *3*, 327–331.

CHAPTER 5: FUTURE EXPERIMENTS

There are two proposed paths for future experiments. The first, expansion of the infrared range, seeks to supplement the current study and to expand understanding of this system. The hope is that such experiments would round out the information already gleaned and bring these experiments to a more satisfying end than we currently have by allowing us to probe the N_2O_4 layer by transmission Fourier-transform infrared spectroscopy. The second, an introduction of gold nanoparticles to the system, is proposed as a next step in understanding processes that occur in the fissures of the amorphous solid water layer by changing the way that heat is introduced into the system.

5.1 Expanding the Infrared Range

An expansion of the infrared range that can be probed requires two changes to the experimental apparatus: changing the windows that the infrared beam must pass through and changing the detector. The current range that can be probed is 1850–7000 cm^{-1} . This is limiting because all of the absorption bands for $\text{NO}_2/\text{N}_2\text{O}_4$ in this range are weak combination bands.

The largest absorption band is at 1740 cm^{-1} and corresponds to the ν_9 asymmetric NO_2 stretch of NO_2 and N_2O_4 [1–3]. It is noteworthy that this absorption band is sensitive to the nature of the surrounding matrix [2]. It may be possible to detect changes before and after irradiation and to correlate the spectral signature with that of N_2O_4 deposited alone, N_2O_4 deposited as a layer in amorphous solid water, and NO_2 co-deposited with amorphous solid water, to characterize some of the movement through the films. For example, it might be possible to tell what percentage of the N_2O_4 deposited atop amorphous solid water percolates down into the water layer by

comparing spectra of N_2O_4 on bare MgO versus N_2O_4 atop varying thicknesses of amorphous solid water.

The current infrared range that can be probed is limited both by the CaF_2 windows through which the infrared beam must pass and by the InSb detector in current use. Commercial CaF_2 windows have a low-wavelength transmission cut-off around $10\ \mu\text{m}$ ($1000\ \text{cm}^{-1}$) for a 2-mm window thickness, while BaF_2 extends the range to $13.5\ \mu\text{m}$ ($740\ \text{cm}^{-1}$). A liquid nitrogen-cooled HgCdTe detector is commonly available with a low-wavelength cut-off of $24\ \mu\text{m}$ ($416\ \text{cm}^{-1}$), with a peak responsivity of $\geq 200\ \text{V/W}$ at $18\ \mu\text{m}$. This expands the IR range down to $740\ \text{cm}^{-1}$, allowing detection of the major infrared bands of N_2O_4 [1, 3, 4].

5.2 Introducing Gold Nanoparticles

Rather than forming random fissures in the amorphous solid water by using a guest molecule to forge its way through a layer, gold nanoparticles can be laser-heated to create more well-defined pathways in the amorphous solid water (Fig. 5.1). More specifically, uniform “chimneys” can be created in a layered film of N_2O_4 and H_2O (as) then probed by a laser pulse that is either resonant with the nanosphere but not the guest molecule, or one that is resonant with the guest molecule but transparent to the nanosphere. A variety of sizes and shapes of gold nanoparticles can be explored for optimum results, as they will absorb different wavelengths and create chimneys of varying diameters.

The absorption of radiation by gold nanoparticles is dominated by the effect of an electromagnetic field on the conduction-band electrons of the nanoparticle. The electrons are perturbed by the field induced by a photonic interaction, and Coulomb forces act to restore equilibrium between the electrons and the positive ions in lattice. The interplay between these two forces sets up a harmonic oscillation with a bulk

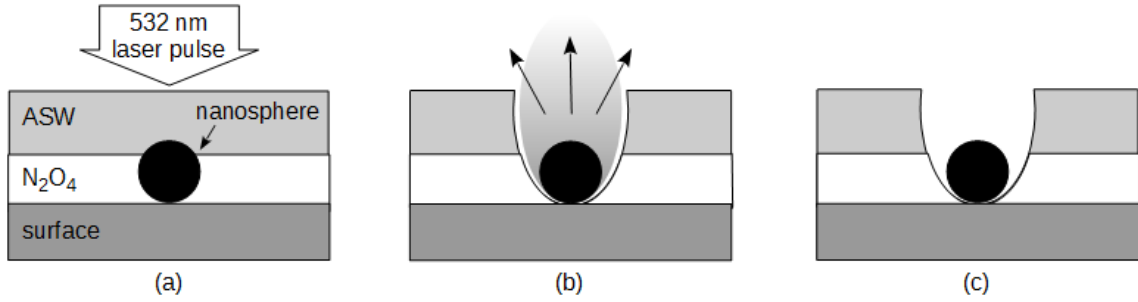


Figure 5.1: (a) N_2O_4 and amorphous solid water are deposited over a nanosphere and irradiated with a 532-nm laser pulse. (b) Material near the nanosphere is heated and expelled. (c) A well-defined pathway, or “chimney,” has been created.

plasmon frequency, ω_p :

$$\omega_p = \sqrt{\frac{Ne^2}{m_e \epsilon_0}} \quad (5.1)$$

where N is the electron density, e is the electric charge, m_e is the electron mass, and ϵ_0 is the permittivity of free space.

Once we go from bulk to nanoscale, the size of the particle affects the harmonic oscillations. This can be seen in the Drude-Sommerfeld model, in the equation for the size-dependant contribution to the dielectric function of the nanoparticle:

$$\epsilon(\omega, D) = 1 - \frac{\omega_p^2}{\omega^2 + i\gamma(D) \cdot \omega} \quad (5.2)$$

Here, ϵ is the dielectric function and γ is a phenomenological damping coefficient that is dependent on the particle diameter, D [5, 6]:

$$\gamma(D) = \gamma_0 + 2\frac{Av_F}{D} \quad (5.3)$$

Equation 5.3 relates the bulk damping coefficient of the material, γ_0 , to the

nanoparticle diameter with the Fermi velocity of the electrons, v_F , and A , a dimensionless parameter that accounts for additional damping effects [6].

The size effect arises partly from the polarizability of the nanoparticle, which affects the Fermi velocity. The electrons and holes separate by roughly the diameter of the particle, and a retardation effect occurs because one end of the particle has a delayed response to changes at the other end of the particle. This induces a phase delay in the oscillations and changes the period of oscillation [7]. Additionally, the mean free path of the electrons is reduced by electron-phonon collisions when the size of the particle approaches the mean free path [5].

It is worthwhile to explore the use of several nanosphere sizes both to optimize signal and to see if there are other differences in the ease of working with the particles. A range of sizes from 10 to 80 nm will all have significant absorption at 532 nm, although they will not all have identical peak absorption. This wavelength is convenient, as it is the second-harmonic frequency of a Nd:YAG laser; similarly, a 25×168 -nm nanorod will absorb at the fundamental frequency, 1064 nm, and may introduce a pathway that better approximates fissures than the “chimneys” we propose will be produced using nanospheres.

Once chimneys have formed, N_2O_4 or another guest molecule can be deposited. The intent is to fill the chimneys with material and then apply heat to the system once more via subsequent laser pulses. Two interesting situations may be compared: one where the laser pulse is resonant with the nanoparticle but not the guest molecule, as with 532-nm radiation, and one where the laser pulse will only heat the guest molecule, such as 355 or 266-nm radiation.

In the first scenario, the heat pulse originates at the nanoparticle and must conduct through the N_2O_4 to either create a hot fluid at the bottom of the chimney which must then force its way through the colder “plug” of N_2O_4 above it, presumably scraping the walls and taking H_2O with it. If the material is instead confined such that

the thermal front travels faster than the directly heated material can escape, it will instead evaporate material at the top of the chimney. The difference between these two processes may be apparent through time-of-flight mass spectrometry detection of the NO_2 monomer versus the dimer. Laser pulses with a lower fluence are more likely to induce evaporation at the surface, and differences in the proportion of water molecules to guest molecules that desorb in a high-fluence “wall-scraping” scenario may distinguish it from surface evaporation. Layering the chimney material with an additional guest molecule with a similar desorption barrier as N_2O_4 may also help distinguish the signatures of these two processes.

In the second scenario, the chimney contents should undergo uniform heating along the length of the chimney. If the time-of-flight mass spectra are similar to the second-pulse data collected with thick upper films of amorphous solid water over buried strata of N_2O_4 , this will contribute substantial evidence in agreement with the model that has been proposed in this thesis, i.e., that after the initial expulsion of material there exist robust, material-filled pathways connecting the buried stratum of N_2O_4 to vacuum.

With an expanded IR range, the quantity of N_2O_4 which deposits on the surface can be calibrated and, using heat-transfer simulations such as those depicted in Figure 5.2, the volume of the chimney can be estimated. Using both of these techniques, the quantity of N_2O_4 (or other guest molecule) within a chimney can be estimated.

5.2.1 COMSOL simulations: producing chimneys with gold nanospheres

COMSOL Multiphysics[®] was used to demonstrate the geometry of heat flow from a gold nanosphere on a MgO substrate, embedded in a surrounding medium. A 20-nm particle was placed 2 nm above the highly conductive MgO boundary because we do not anticipate ideal thermal contact between the nanoparticle and

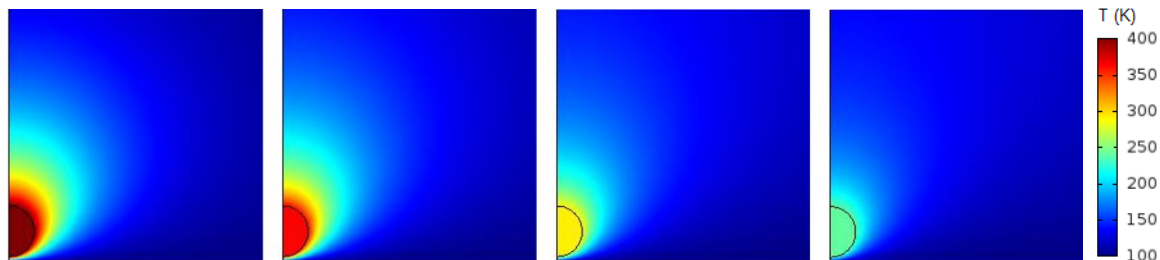


Figure 5.2: Heat transfer from a 20-nm, heated gold nanoparticle into a surrounding matrix. The nanoparticle is held at 400 K for 0.5 ns. The thermal evolution is shown here at $t = 0.5, 1, 2,$ and 3 ns.

the surface. This is in part because colloidal gold nanoparticles are capped with a layer of citrate molecules, which prevent the nanoparticles from aggregating further. The surrounding medium is given the physical properties of amorphous solid water and allowed to extend upwards and laterally for hundreds of nanometers to avoid boundary effects. The particle is arbitrarily held at 400 K for 0.5 ns and then allowed to cool. The temperature reached is not important in this simulation, as we are interested in the direction of heat flow.

As shown in Figure 5.2, heat is transferred vertically more than it is transferred laterally. The high conductivity of the MgO substrate rapidly cools the nanosphere and limits heat transfer in the horizontal direction. This is precisely what is necessary to form chimneys — we do not want significant lateral flow. Material above the nanosphere should reach temperatures which allow the desorption of the material; there may even be local superheating of the water surrounding the nanoparticle which results in eruptions as seen with N_2O_4 , but which will naturally escape towards vacuum through the warmer, more labile water molecules above the nanosphere and facilitate the formation of a chimney.

5.2.2 Preliminary experiments

To give an initial proof-of-principle, it was first verified that we could deposit nanoparticles on an MgO surface. An atomic force microscope was used to image a freshly cleaved piece of MgO. Solutions of citrate-capped 10, 20, 40, and 80-nm nanospheres in water [NanoPartz] were obtained; all absorb 532-nm radiation. A solution of 25×168-nm nanorods was also obtained, but has not yet been used as it absorbs at a different wavelength (1064 nm). The colloidal nanosphere solutions were diluted with water to $5 \pm 1 \times 10^{10}$ nanoparticles/mL. One drop of solution wet the entire face of the 1 cm × 1 cm MgO; with approximately 20 drops/mL, this gave a theoretical deposition of 20–30 nanoparticles/ μm^2 . The 80-nm particle solution was not diluted (see Table 5.1). After putting a drop of solution on the MgO surface, the water was gently evaporated using a low flow of N₂ gas. The surface was then imaged by atomic force microscopy. The nanoparticles were readily discernible on the surface, and had an average distribution of 1–10 nanoparticles/ μm^2 . The nanoparticles did not show a tendency to stick to defect sites such as along terrace edges of the MgO. The 20-nm particles did not clump together significantly, but the 80-nm particles appear to have aggregated. Figure 5.4 shows a typical atomic force microscopy image of nanoparticles on MgO.

20-nm gold spheres were deposited first; oxygen vacancies were not filled on these MgO substrates to avoid possible sintering of nanoparticles in close proximity to one another [8, 9]. Time-of-flight mass spectrometry signals acquired upon 532-nm irradiation of ASW deposited over the nanospheres were fairly sensitive to fluence — our typical energy of around 1.8 mJ (measured outside the chamber) focused on the surface gave no signal, but energies above about 6 mJ produced very large ion packets with only a small trail of neutral signal afterward. This was verified by recording a signal with the *e*-gun turned off, which showed the large, structureless ion signal

Table 5.1: Properties of nanoparticles for proposed future experiments and used for preliminary experiments. The nanoparticle dimensions are the sphere diameter or, for the nanorod, the length and width.

Size (nm)	λ_{max} (nm)	Concentration (nps/mL)
10	527	5.35×10^{12}
20	519	6.82×10^{11}
40	528	8.69×10^{10}
80	550	1.22×10^{10}
25×168	1064	3.3×10^{10}

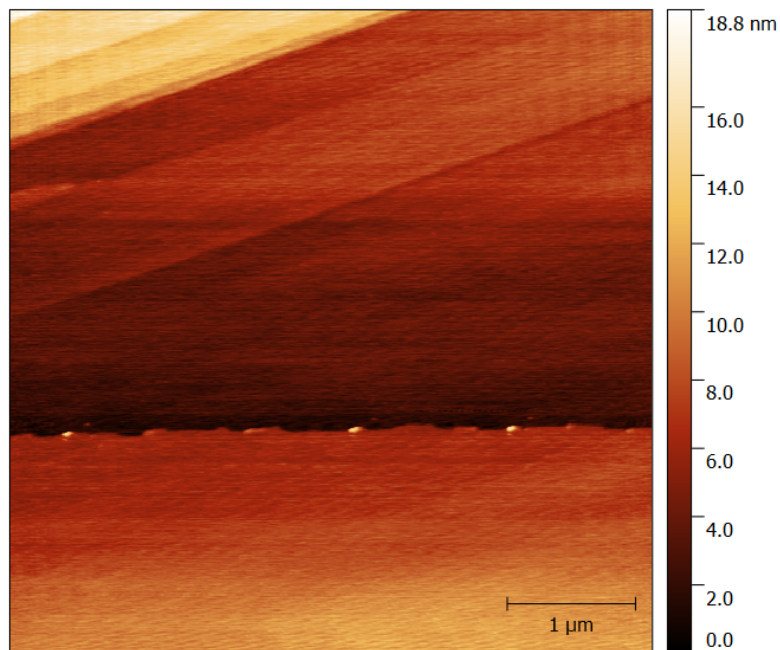


Figure 5.3: Atomic force microscopy image of bare MgO. Cleaved MgO provides a macroscopically flat surface with terracing as its main defect, as can be seen here. The upper half shows a series of parallel terracing; the sharp height transition in the lower half of the image is not typical, but it is a real feature of this section of the MgO surface and not an artifact. Note that over a distance of several micrometers, the total variation in terrace height is orders of magnitude smaller (<20 nm).

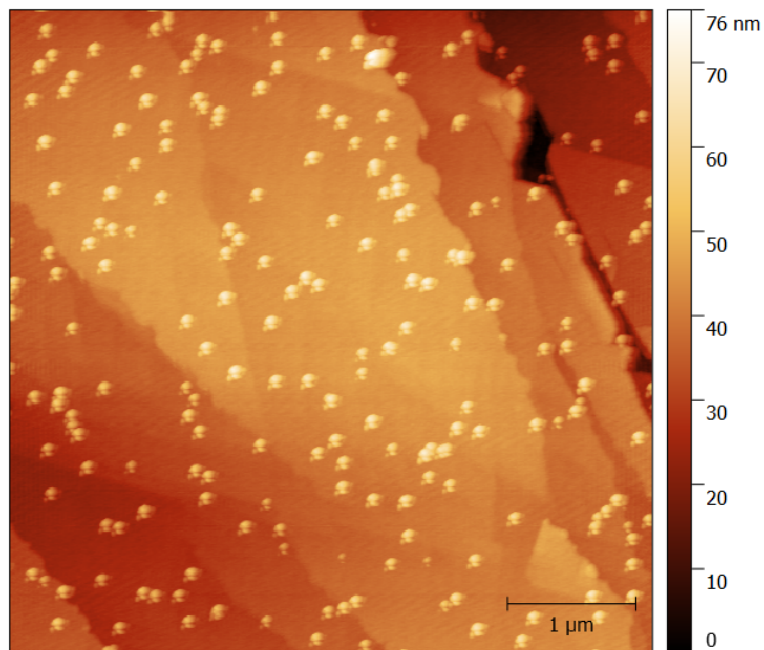


Figure 5.4: Atomic force microscopy image of 20-nm gold nanospheres on MgO. The nanospheres do not appreciably aggregate on the surface. Distinct height changes in the substrate are due to terrace edges; the nanospheres do not have a tendency to deposit at these terrace edges. These two observations have been true for all nanosphere sizes. Nanosphere sizes should be judged by their difference in height from the surrounding surface, as their apparent widths can be an artifact due to the microscope tip traversing the sharp height increase, as illustrated in Figure 5.5.

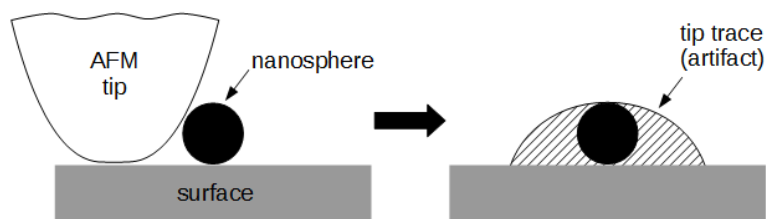


Figure 5.5: A cartoon showing how an atomic force microscope tip creates artifacts in the imaging of small particles with abrupt height changes. The size of the nanoparticles must be judged by the height of the particle as measured by the atomic force microscope, and not by its apparent size in relation to the scale of the image. This can be seen in Figure 5.4, but in Figure 5.7a the particles appear to be as large as 1 μm , which is more likely due to particle aggregation.

but no progression of signal afterward. In some cases, the discernible structure in the spectra showed fragments consistent with citrate, the ligand capping the nanospheres. Additionally, some of the spots on the surface that were irradiated with these higher fluences showed optical damage of the MgO.

A focused pulse of 5.2 mJ gave a clean time-of-flight profile with no formation of ionic species and an adequate signal intensity. Figure 5.6 shows a temporal profile collected from a *single laser pulse* and the sum of all of the individual mass spectra, showing the presence of only water. Laser pulses of this energy did not damage the surface. This data, although preliminary, shows that amorphous solid water can undergo laser-induced desorption via energy transfer from gold nanoparticles. However, repeated experiments (with new H₂O(as) depositions) showed progressively diminishing signal on location of MgO which had already been irradiated. A possible explanation for this was found when 80-nm particles were used.

The 80-nm particles were similarly deposited on a fresh-cleaved MgO surface and imaged via atomic force microscopy. Particles of this size appear to have aggregated some (Fig. 5.7a). Initial time-of-flight signals from laser irradiation showed large ion desorptions followed by very small water signals. Subsequent experiments had a continually decreasing signal. No damage to the surface was seen. After signal was lost, an atomic force microscopy image was taken of the surface. It appears that the nanoparticles themselves were ablated from the surface. As seen in Figure 5.7a, 80-nm particles are present on the surface immediately following deposition. However, once the surface has been irradiated there are large features on the surface that appear to be splatters of an exploded nanoparticle, a known phenomenon [10–12]. Note that the “splatters” are protruding from the surface, and not indents that would imply damage and pitting to the MgO surface. Obliteration of the nanoparticles would, of course, be consistent with a progressive inability to absorb 532-nm radiation.

10-nm particles were deposited on a fresh MgO surface, but could not be

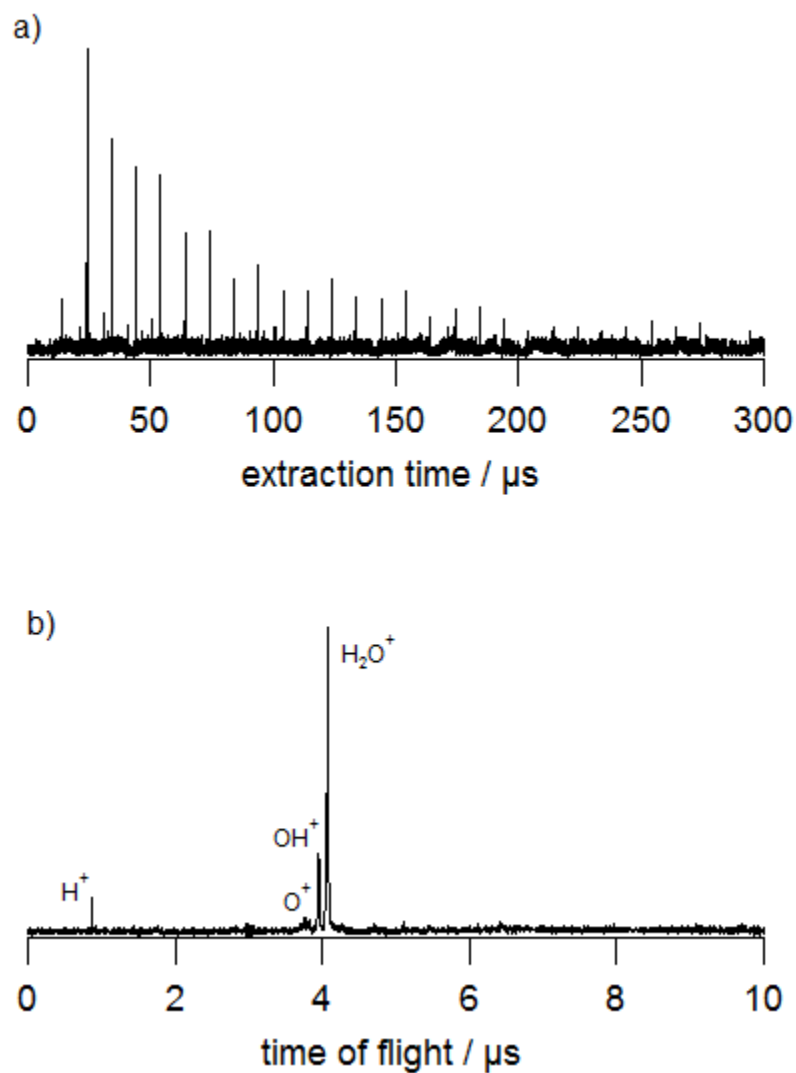
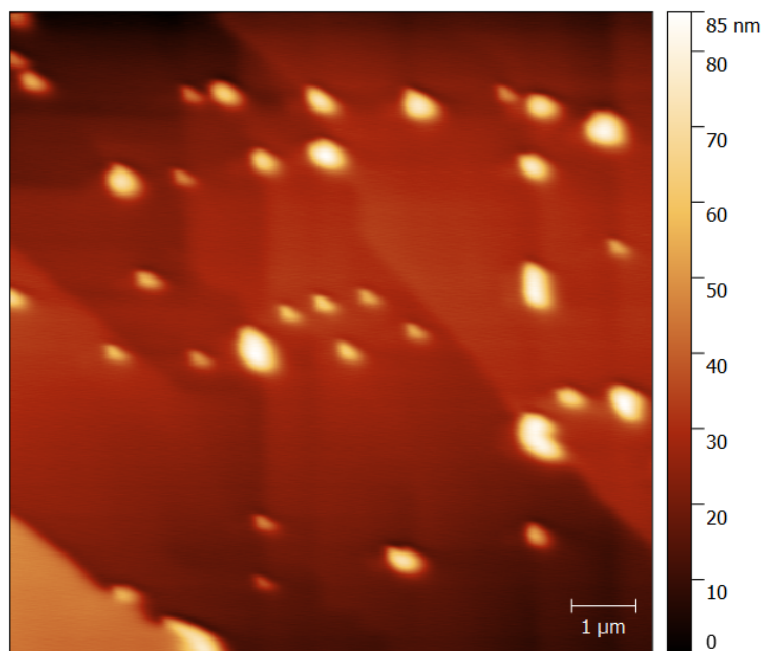
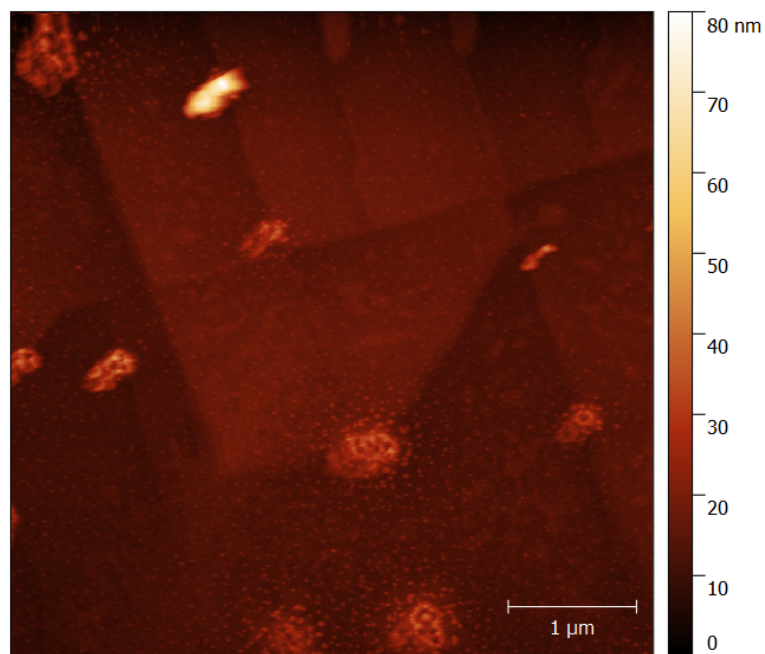


Figure 5.6: Time-of-flight spectra of water desorbed via irradiation of 20-nm gold nanoparticles with amorphous solid water on top. (a) Temporal profile, and (b) average of several individual time-of-flight spectra showing the typical signature of desorbed water.



(a)



(b)

Figure 5.7: Atomic force microscopy image of 80-nm gold nanospheres on MgO (a) before and (b) after laser irradiation. Laser fluences had to be high to desorb material, but any irradiated spot which yielded material did so for only a few pulses and subsequent experiments with fresh depositions still gave no signal. As can be seen in (b), the particles appear to have completely exploded and litter the surface with splattered material, which would no longer be able to absorb 532-nm radiation.

detected by atomic force microscopy; 40-nm particles were attempted as well but, for unknown reasons, showed no deposited nanoparticles in atomic force microscopy images and yielded no time-of-flight mass spectrometry signal in its first trial. At this juncture, 20-nm particles appear to offer the most promise, but more experimentation is necessary to adjust, for example, the concentrations used or to optimize conditions to attempt signal acquisition with these particle sizes.

Overall, these preliminary results give a proof-of-principle and have also highlighted some of the challenges that will be encountered in pursuing experiments using gold nanoparticles. Work must first be done to optimize the signal that can be acquired and to increase the longevity of the irradiated nanoparticles. This may require the exploration of differing nanoparticle deposition techniques and other modifications to the experimental conditions.

5.3 Chapter 5 References

- [1] Roux, J. A.; Wood, B. E. *J. Opt. Soc. Am.* **1983**, *73*, 1181–1188.
- [2] Fateley, W. G.; Bent, H. A.; Crawford, Jr., B. *J. Chem. Phys.* **1959**, *31*, 204–217.
- [3] Givan, A.; Loewenschuss, A. *J. Chem. Phys.* **1989**, *90*, 6135–6142.
- [4] Givan, A.; Loewenschuss, A. *J. Chem. Phys.* **1990**, *93*, 866–867.
- [5] Link, S.; El-Sayed, M. A. *J. Phys. Chem. B* **1999**, *103*, 4212–4217.
- [6] Berciaud, S.; Cognet, L.; Tamarat, P.; Lounis, B. *Nano Lett.* **2005**, *5*, 515–518.
- [7] Myroshnychenko, V.; Rodríguez-Fernández, J.; Pastoriza-Santos, I.; Funston, A. M.; Novo, C.; Mulvaney, P.; Liz-Marzán, L. M.; García de Abajo, F. J. *Chem. Soc. Rev.* **2008**, *37*, 1792–1805.
- [8] Bore, M. T.; Pham, H. N.; Switzer, E. E.; Ward, T. L.; Fukuoka, A.; Datye, A. K. *J. Phys. Chem. B* **2005**, *109*, 2873–2880.
- [9] Veith, G. M.; Lupini, A. R.; Rashkeev, S.; Pennycook, S. J.; Mullins, D. R.; Schwartz, V.; Bridges, C. A.; Dudney, N. J. *J. Catal.* **2009**, *262*, 92–101.
- [10] Link, S.; Burda, C.; Mohamed, M. B.; Nikoobakht, B.; El-Sayed, M. A. *J. Phys. Chem. A* **1999**, *103*, 1165–1170.
- [11] Inasawa, S.; Sugiyama, M.; Yamaguchi, Y. *J. Phys. Chem. B* **2005**, *109*, 9404–9410.
- [12] Hashimoto, S.; Werner, D.; Uwada, T. *J. Photochem. Photobiol. C Photochem. Rev.* **2012**, *13*, 28–54.

CHAPTER 6: CONCLUSION

An experimental approach has been developed for studying laser-initiated material transport and removal in layered films of amorphous solid water and N_2O_4 . A MgO substrate at 100 K is covered with an amorphous solid water layer to insulate heated N_2O_4 from the MgO substrate, which has high thermal conductivity. The N_2O_4 layer is covered with up to 1440 L of amorphous solid water. Pulsed 266-nm irradiation (10 ns; 1 mJ, focused with a 50 cm lens to ~ 0.3 mm diameter) heats N_2O_4 , and we propose that material flow takes place through fissures that extend from the N_2O_4 layer to vacuum. Temporal profiles and mass spectra (at 10 μs intervals) following a single pulse provide information on timescales and transport mechanisms.

The microcosm created in these studies is challenging insofar as developing a quantitative model. Nonetheless, qualitative understanding has been achieved, with trends and phenomena in line with predictions. A quantitative model will require a combination of laboratory and computational work.

Specific contributions to this research include the design and implementation of a specialized gas dosing system for vapor deposition of $\text{NO}_2(\text{g})$ onto the MgO substrate to form $\text{N}_2\text{O}_4(\text{s})$. The substrate holder was modified from previous designs to improve thermal contact with the copper blocks of the sample holder. A computational simulation of heat transfer in $\text{H}_2\text{O}(\text{as})/\text{N}_2\text{O}_4$ on a MgO surface was modeled, and trends in cooling rates under varying conditions were found to be consistent with the proposed mechanism of material release. The main features of the current model are summarized below.

Laser-initiated heating of the N_2O_4 layer results in fissures that connect the heated layer to vacuum. The pressure of the heated fluid provides thrust that launches material toward the surface. Fissures allow transport of heated material to vacuum without freezing on the walls. Many of the fissures are robust, surviving many pulses.

It is possible to halt the flow of heated fluid prior to it entering vacuum by reducing the fluence. Subsequent irradiation causes fluid to enter vacuum, and this fracking-like pumping continues with consecutive laser pulses. Efficient H/D scrambling using alternating $\text{H}_2\text{O}(\text{as})$ and $\text{D}_2\text{O}(\text{as})$ layers demonstrate that water is removed from fissure walls and entrained in fluid flow. There is interplay between the fluid freezing onto fissure walls versus removal of water from the fissure walls by the heated fluid.

Heated material reaches vacuum with a single pulse. As the thickness of the upper amorphous solid water layer is increased, the fractional amount of water that enters vacuum increases, presumably because warm fluid passes over more fissure area. The N_xO_y -rich fluid that moves through the fissures continues to be heated as long as the pulse is on. Figure 4.15 indicates that cooling is efficient enough that fluid in a fissure freezes shortly after termination of the pulse. This can be used to obtain a rough lower bound of the speed with which fluid passes through fissures toward vacuum.

For a 1000-nm thick amorphous solid water layer, material that travels through the fissures does so at 100 m/s or faster. Had the speed been lower, material that commenced travel at the N_2O_4 layer with the onset of the laser pulse would freeze before it reached the sample surface. In other words, material moving toward the surface would freeze on the fissure wall. With thinner samples, it follows that a significant amount of effluent enters the gas phase within the duration of the laser pulse. This is consistent with our observation of early N_xO_y arrival times at the ionization region, as well as the presence of NO_2 , presumably due to N_2O_4 266-nm photodissociation.

Fissure density is high enough to ensure collisions between effluents from neighboring fissures. This rationalizes long arrival times at the ionization region, e.g., > 1 ms, and the lumpy appearance of the temporal profiles. We propose that ejected material undergoes collisions with other molecules and metal surfaces, such as components of the time-of-flight mass spectrometer, and takes a circuitous path

before reaching the ionization region.

It would be useful to characterize material transport through fissures more quantitatively, i.e., by preparing fissures whose properties are known and controllable. We have obtained preliminary results along these lines using a sparse density of gold nanospheres on MgO. Such particles serve as templates for creating channels in amorphous solid water through deposition and pulsed heating.

In closing, similarities between the phenomena observed in this study and those on Enceladus are noteworthy, despite the enormous scale differences. Enceladus has a subsurface ocean of liquid water below a solid water mantle 30–40 km thick. Nevertheless, stresses due to gravitational interactions cause fissures in the ice that expand and contract, releasing water that contains numerous small molecules. This fluid is transported through fissures, and jets are observed. Though beyond the scope of this paper, such similarities are intriguing. More pertinently, most of Enceladus is around 77 K, but the vents are 197 K. Areas near the vents may go through non-crystallizing thermal processes as local temperatures fluctuate.

Notably, crystallization and the “molecular volcano” effect are not required for the expulsion of guest molecules from porous amorphous solid water; this can occur without detectable thermal processing of the amorphous solid water. This has ramifications for the understanding of processes which might expel guest molecules embedded in amorphous solid water which has accreted on dust grains in the interstellar medium. Repeated low-fluence radiation can progressively move a volatile molecule towards vacuum, and expulsion of both water and guest molecules can occur without causing morphological changes in the amorphous solid water.

BIBLIOGRAPHY

- Agnew, S. F.; Swanson, B. I.; Jones, L. H.; Mills, R. L.; Schiferl, D. *J. Phys. Chem.* **1983**, *87*, 5065–5068.
- Andersson, O.; Inaba, A. *Phys. Chem. Chem. Phys.* **2005**, *7*, 1441–1449.
- Andersson, O.; Suga, H. *Solid State Commun.* **1994**, *91*, 985–988.
- Andersson, O.; Suga, H. *Phys. Rev. B* **2002**, *65*, 140201(4).
- Angell, C. A. *Annu. Rev. Phys. Chem.* **2004**, *55*, 559–583.
- Anisimov, S. I.; Bäuerle, D.; Luk'Yanchuk, B. S. *Phys. Rev. B* **1993**, *48*, 12076–12081.
- Anisimov, S. I.; Luk'Yanchuk, B. S.; Luches, A. *Appl. Surf. Sci.* **1996**, *96-98*, 24–32.
- Bar-Nun, A.; Dror, J.; Kochavi, E.; Laufer, D. *Phys. Rev. B* **1987**, *35*, 2427–2435.
- Bar-Nun, A.; Herman, G.; Laufer, D.; Rappaport, M. L. *Icarus* **1985**, *63*, 317–332.
- Bar-Nun, A.; Kleinfeld, I.; Kochavi, E. *Phys. Rev. B* **1988**, *38*, 7749–7754.
- Barron, T. H. K.; Berg, W. T.; Morrison, J. A. *Proc. R. Soc. London A* **1959**, *250*, 70–83.
- Bartram, M. E.; Koel, B. E. *Surf. Sci.* **1989**, *213*, 137–156.
- Batista, E. R.; Ayotte, P.; Bilić, A.; Kay, B. D.; Jónsson, H. *Phys. Rev. Lett.* **2005**, *95*, 223201(4).
- Bauschlicher, Jr, C. W.; Komornicki, A.; Roos, B. *J. Am. Chem. Soc.* **1983**, *105*, 745–748.
- Berciaud, S.; Cognet, L.; Tamarat, P.; Lounis, B. *Nano Lett.* **2005**, *5*, 515–518.
- Bergren, M. S.; Schuh, D.; Sceats, M. G.; Rice, S. A. *J. Chem. Phys.* **1978**, *69*, 3477–3482.
- Bernstein, M. P.; Sandford, S. A.; Allamandola, L. J.; Gillette, J. S.; Clemett, S. J.; Zare, R. N. *Science* **1999**, *283*, 1135–1138.
- Bore, M. T.; Pham, H. N.; Switzer, E. E.; Ward, T. L.; Fukuoka, A.; Datye, A. K. *J. Phys. Chem. B* **2005**, *109*, 2873–2880.
- Brown, D. E.; George, S. M.; Huang, C.; Wong, E. K. L.; Rider, K. B.; Smith, R. S.; Kay, B. D. *J. Phys. Chem.* **1996**, *100*, 4988–4995.
- Burke, D. J.; Brown, W. A. *Phys. Chem. Chem. Phys.* **2010**, *12*, 5947–5969.

- Campbell, C. T.; Valone, S. M. *J. Vac. Sci. Technol. A* **1985**, *3*, 408–411.
- Campbell, M. J.; Liesegang, J.; Riley, J. D.; Jenkin, J. G. *J. Phys. C* **1982**, *15*, 2549–2558.
- Carson, J. K.; Lovatt, S. J.; Tanner, D. J.; Cleland, A. C. *Int. J. Heat Mass Transf.* **2005**, *48*, 2150–2158.
- Chang, E. T.; Poston, T. M.; Gokcen, N. A.; *Density , Compressibility , Thermal Conductivity , and Mechanical Movement of Solid Hydrazine*; Tech. Rep.; The Aerospace Corporation; El Segundo; 1976.
- Cholette, F.; Zubkov, T.; Smith, R. S.; Dohnálek, Z.; Kay, B. D.; Ayotte, P. *J. Phys. Chem. B* **2009**, *113*, 4131–4140.
- Collings, M. P.; Anderson, M. A.; Chen, R.; Dever, J. W.; Viti, S.; Williams, D. A.; McCoustra, M. R. S. *Mon. Not. R. Astron. Soc.* **2004**, *354*, 1133–1140.
- Cuppen, H. M.; Herbst, E. *Astrophys. J.* **2007**, *668*, 294–309.
- d’Hendecourt, L. B.; Allamandola, L. J.; Baas, F.; Greenberg, J. M. *Astron. Astrophys.* **1982**, *109*, L12–L14.
- Dixon-Warren, S. J.; Jackson, R. C.; Polanyi, J. C.; Rieley, H.; Shapter, J. G.; Weiss, H. *J. Phys. Chem.* **1992**, *96*, 10983–10994.
- Dohnálek, Z.; Kimmel, G. A.; Ayotte, P.; Smith, R. S.; Kay, B. D. *J. Chem. Phys.* **2003**, *118*, 364–372.
- Draine, B. T. *Annu. Rev. Astron. Astrophys.* **2003**, *41*, 241–289.
- Dunning, W. J. *Q. Rev. Chem. Soc.* **1955**, *9*, 23–50.
- Ehrenfreund, P.; Charnley, S. B. *Annu. Rev. Astron. Astrophys.* **2000**, *38*, 427–483.
- Ehrenfreund, P.; Dartois, E.; Demyk, K.; d’Hendecourt, L. *Astron. Astrophys.* **1998**, *20*, L17–L20.
- English, N. J.; Tse, J. S. *Phys. Rev. B* **2011**, *83*, 184114(9).
- English, N. J.; Tse, J. S.; Gallagher, R. *Phys. Rev. B* **2010**, *82*, 092201(4).
- Falenty, A.; Hansen, T. C.; Kuhs, W. F. *Nature* **2014**, *516*, 231–233.
- Fateley, W. G.; Bent, H. A.; Crawford, Jr., B. *J. Chem. Phys.* **1959**, *31*, 204–217.
- Gálvez, O.; Maté, B.; Herrero, V. J.; Escribano, R. *Icarus* **2008**, *197*, 599–605.
- Ghormley, J. A.; Hochanadel, C. J. *Science* **1971**, *171*, 62–64.
- Giauque, W. F.; Kemp, J. D. *J. Chem. Phys.* **1938**, *6*, 40–51.

- Giauque, W. F.; Stout, J. W. *J. Am. Chem. Soc.* **1936**, *58*, 1144–1150.
- Gibb, E. L.; Whittet, D. C. B.; Boogert, A. C. A.; Tielens, A. G. G. M. *Astrophys. J. Suppl. Ser.* **2004**, *151*, 35–73.
- Givan, A.; Loewenschuss, A. *J. Chem. Phys.* **1989**, *90*, 6135–6142.
- Givan, A.; Loewenschuss, A. *J. Chem. Phys.* **1990**, *93*, 866–867.
- Givan, A.; Loewenschuss, A. *J. Chem. Phys.* **1990**, *93*, 7592–7600.
- Goguen, J. D.; Buratti, B. J.; Brown, R. H.; Clark, R. N.; Nicholson, P. D.; Hedman, M. M.; Howell, R. R.; Sotin, C.; Cruikshank, D. P.; Baines, K. H.; Lawrence, K. J.; Spencer, J. R.; Blackburn, D. G. *Icarus* **2013**, *226*, 1128–1137.
- Gudipati, M. S.; Allamandola, L. J. *Astrophys. J.* **2004**, *615*, L177–L180.
- Gudipati, M. S.; Allamandola, L. J. *Astrophys. J.* **2006**, *638*, 286–292.
- Hagen, W.; Tielens, A. G. G. M.; Greenberg, J. M. *Chem. Phys.* **1981**, *56*, 367–379.
- Hallbrucker, A.; Mayer, E.; Johari, G. P. *J. Phys. Chem.* **1989**, *93*, 4986–4990.
- Hama, T.; Watanabe, N. *Chem. Rev.* **2013**, *113*, 8783–839.
- Handa, Y. P.; Klug, D. D. *J. Phys. Chem.* **1988**, *92*, 3323–3325.
- Hansen, C. J.; Esposito, L. W.; Stewart, A. I. F.; Meinke, B.; Wallis, B.; Colwell, J. E.; Hendrix, A. R.; Larsen, K.; Pryor, W.; Tian, F. *Nature* **2008**, *456*, 477–479.
- Hansen, C. J.; Shemansky, D. E.; Esposito, L. W.; Stewart, A. I. F.; Lewis, B. R.; Colwell, J. E.; Hendrix, A. R.; West, R. A.; Waite, Jr., J. H.; Teolis, B. D.; Magee, B. A. *Geophys. Res. Lett.* **2011**, *38*, L11202(5).
- Hashimoto, S.; Werner, D.; Uwada, T. *J. Photochem. Photobiol. C Photochem. Rev.* **2012**, *13*, 28–54.
- Hawkins, S.; Kumi, G.; Malyk, S.; Reisler, H.; Wittig, C. *Chem. Phys. Lett.* **2005**, *404*, 19–24.
- Heinrich, V. E.; Cox, P. A. *The Surface Science of Metal Oxides*; Cambridge University Press: Cambridge, 1994.
- Hessinger, J.; White, Jr., B. E.; Pohl, R. O. *Planet. Space Sci.* **1996**, *44*, 937–944.
- Hisatsune, I. C. *J. Phys. Chem.* **1961**, *1319*, 2249–2253.
- Hudson, R. L.; Donn, B. *Icarus* **1991**, *94*, 326–332.
- Iess, L.; Stevenson, D. J.; Parisi, M.; Hemingway, D.; Jacobson, R. A.; Lunine, J. I.; Nimmo, F.; Armstrong, J. W.; Asmar, S. W.; Ducci, M.; Tortora, P. *Science* **2014**, *344*, 78–80.

- Inasawa, S.; Sugiyama, M.; Yamaguchi, Y. *J. Phys. Chem. B* **2005**, *109*, 9404–9410.
- Incropera, F. P.; DeWitt, D. P.; Bergman, T. L.; Lavine, A. S. *Fundamentals of Heat and Mass Transfer*, 6th ed.; John Wiley & Sons, 2006.
- Jenniskens, P.; Banham, S. F.; Blake, D. F.; McCoustra, M. R. S. *J. Chem. Phys.* **1997**, *107*, 1232–1241.
- Jenniskens, P.; Blake, D. F. *Science* **1994**, *265*, 753–756.
- Jenniskens, P.; Blake, D. F. *Astrophys. J.* **1996**, *473*, 1104–1113.
- Johari, G. P.; Hallbrucker, A.; Mayer, E. *J. Chem. Phys.* **1992**, *97*, 5851–5855.
- Johari, G. P.; Hallbrucker, A.; Mayer, E. *Nature* **1987**, *330*, 552–553.
- Kim, S. K.; Kang, H. *J. Phys. Chem. Lett.* **2010**, *1*, 3085–3089.
- Kim, Y.-K.; Rudd, M. E. *Phys. Rev. A* **1994**, *50*, 3954–3967.
- Klinger, J. *Science* **1980**, *209*, 271–272.
- Koch, T. G.; Horn, A. B.; Chesters, M. A.; McCoustra, M. R. S.; Sodeau, J. R. *J. Phys. Chem.* **1995**, *99*, 8362–8367.
- Kohata, K.; Fukuyama, T.; Kuchitsu, K. *J. Phys. Chem.* **1982**, *86*, 602–606.
- Kohl, I.; Mayer, E.; Hallbrucker, A. *Phys. Chem. Chem. Phys.* **2000**, *2*, 1579–1586.
- Korolik, M.; Suchan, M. M.; Johnson, M. J.; Arnold, D. W.; Reisler, H.; Wittig, C. *Chem. Phys. Lett.* **2000**, *326*, 11–21.
- Krasnopoler, A.; George, S. M. *J. Phys. Chem. B* **1998**, *102*, 788–794.
- Krupskii, I. N.; Manzhely, V. G.; Koloskova, L. A. *Phys. Status Solidi* **1968**, *27*, 263–268.
- Kumi, G.; Ph. D. thesis; University of Southern California; 2007.
- Kvick, A.; McMullan, R. K.; Newton, M. D. *J. Chem. Phys.* **1982**, *76*, 3754–3761.
- Laufer, D.; Bar-Nun, A.; Pat-El, I.; Jacovi, R. *Icarus* **2013**, *222*, 73–80.
- Laufer, D.; Kochavi, E.; Bar-Nun, A. *Phys. Rev. B* **1987**, *36*, 9219–9227.
- Lignell, H.; Varner, M. E.; Finlayson-Pitts, B. J.; Gerber, R. B. *Chem. Phys.* **2012**, *405*, 52–59.
- Link, S.; Burda, C.; Mohamed, M. B.; Nikoobakht, B.; El-Sayed, M. A. *J. Phys. Chem. A* **1999**, *103*, 1165–1170.
- Link, S.; El-Sayed, M. A. *J. Phys. Chem. B* **1999**, *103*, 4212–4217.

- Linstrom, P. J.; Mallard, W. G. *NIST Chemistry WebBook, NIST Standard Reference Database Number 69*; National Institute of Standards and Technology: Gaithersburg MD, 2014.
- Lisse, C.; Bar-Nun, A.; Laufer, D.; Belton, M.; Harris, W.; Hsieh, H.; Jewitt, D. In *Sci. Sol. Syst. Ices*; Gudipati, M. S.; Castillo-Rogez, J., Eds.; Astrophysics and Space Science Library, Vol. 356; Springer New York: New York, NY, 2013; Chapter 13, pp 455–485.
- Madey, T. E.; Johnson, R. E.; Orlando, T. M. *Surf. Sci.* **2002**, *500*, 838–858.
- Makarounis, O.; Jenkins, R. J.; *Thermal diffusivity and heat capacity measurements at low temperatures by the flash method*; Tech. Rep.; U.S. Naval Radiological Defense Laboratory; San Francisco; 1962.
- Malyk, S.; Kumi, G.; Reisler, H.; Wittig, C. *J. Phys. Chem. A* **2007**, *111*, 13365–13370.
- Mamyrin, B. A. *Int. J. Mass Spectrom.* **2001**, *206*, 251–266.
- Manca, C.; Martin, C.; Roubin, P. *Chem. Phys.* **2004**, *300*, 53–62.
- Mastrapa, R. M. E.; Grundy, W. M.; Gudipati, M. S. In *Sci. Sol. Syst. Ices*; Gudipati, M. S.; Castillo-Rogez, J., Eds.; Astrophysics and Space Science Library, Vol. 356; Springer New York: New York, NY, 2013; Chapter 11, pp 371–408.
- May, R. A.; Smith, R. S.; Kay, B. D. *J. Phys. Chem. Lett.* **2012**, *3*, 327–331.
- May, R. A.; Smith, R. S.; Kay, B. D. *J. Chem. Phys.* **2013**, *138*, 104501(11).
- May, R. A.; Smith, R. S.; Kay, B. D.; Alan May, R.; Scott Smith, R.; Kay, B. D. *J. Chem. Phys.* **2013**, *138*, 104502(11).
- Mayer, E. *J. Phys. Chem.* **1985**, *89*, 3474–3477.
- Mayer, E.; Pletzer, R. *Nature* **1986**, *319*, 298–301.
- McLafferty, F. W. *Anal. Chem.* **1956**, *28*, 306–316.
- Merienne, M. F.; Jenouvrier, A.; Coquart, B.; Lux, J. P. *J. Atmos. Chem.* **1995**, *20*, 281–297.
- Minissale, M.; Congiu, E.; Baouche, S.; Chaabouni, H.; Moudens, A.; Dulieu, F.; Manicó, G.; Pirronello, V. *Chem. Phys. Lett.* **2013**, *565*, 52–55.
- Miotello, A.; Kelly, R. *Appl. Phys. A* **1999**, *69*, S67–S73.
- Mitterdorfer, C.; Bauer, M.; Youngs, T. G. A.; Bowron, D. T.; Hill, C. R.; Fraser, H. J.; Finney, J. L.; Loerting, T. *Phys. Chem. Chem. Phys.* **2014**, *16*, 16013–16020.

- Myroshnychenko, V.; Rodríguez-Fernández, J.; Pastoriza-Santos, I.; Funston, A. M.; Novo, C.; Mulvaney, P.; Liz-Marzán, L. M.; García de Abajo, F. J. *Chem. Soc. Rev.* **2008**, *37*, 1792–1805.
- Narten, A. H.; Venkatesh, C. G.; Rice, S. A. *J. Chem. Phys.* **1976**, *64*, 1106–1121.
- Newman, S. F.; Buratti, B. J.; Brown, R. H.; Jaumann, R.; Bauer, J.; Momary, T. *Icarus* **2008**, *193*, 397–406.
- Ossenkopf, V. *Astron. Astrophys.* **1993**, *280*, 617–646.
- Parent, P.; Laffon, C.; Mangeney, C.; Bournel, F.; Tronc, M. *J. Chem. Phys.* **2002**, *117*, 10842–10851.
- Park, S.-C.; Jung, K.-H.; Kang, H. *J. Chem. Phys.* **2004**, *121*, 2765–74.
- Porco, C. C.; DiNino, D.; Nimmo, F. *Astron. J.* **2014**, *148*, 45(24).
- Porco, C. C.; et al. *Science* **2006**, *311*, 1393–1401.
- Rebolledo-Mayoral, O. R.; Stomberg, J.; McKean, S.; Reisler, H.; Wittig, C. *J. Phys. Chem. C* **2012**, *116*, 563–569.
- Rieley, H.; Colby, D. J.; McMurray, D. P.; Reeman, S. M. *Surf. Sci.* **1997**, *390*, 243–249.
- Rieley, H.; McMurray, D. P.; Haqb, S. *J. Chem. Soc. Faraday Trans.* **1996**, *92*, 933–939.
- Roux, J. A.; Wood, B. E. *J. Opt. Soc. Am.* **1983**, *73*, 1181–1188.
- Russ, F. *Zeitschrift für Phys. Chemie* **1914**, *82*, 217–222.
- Salzmann, C. G.; Radaelli, P. G.; Mayer, E.; Finney, J. L. *Phys. Rev. Lett.* **2009**, *103*, 105701(4).
- Sato, S.; Senga, T.; Kawasaki, M. *J. Phys. Chem. B* **1999**, *103*, 5063–5069.
- Schlegel, H. B.; Skancke, A. *J. Am. Chem. Soc.* **1992**, *115*, 7465–7471.
- Schou, J. R.; Amaruso, S.; Lunney, J. G. In *Laser Ablation and its Applications*; Phipps, C., Ed.; Optical Sciences; Springer: Santa Fe, New Mexico, 2007; Chapter 4, pp 67–91.
- Seiber, B. A.; Wood, B. E.; Smith, A. M.; Müller, P. R.; Delsemme, A. H.; Wenger, A. *Science* **1970**, *170*, 652–654.
- Shulman, L. M. *Astron. Astrophys.* **2004**, *416*, 187–190.
- Slack, G. A. *Phys. Rev.* **1962**, *126*, 427–441.

- Slack, G. A. *Phys. Rev. B* **1980**, *22*, 3065–3071.
- Smoluchowski, R. *Science* **1978**, *201*, 809–811.
- Speedy, R. J.; Debenedetti, P. G.; Smith, R. S.; Huang, C.; Kay, B. D. *J. Chem. Phys.* **1996**, *105*, 240–244.
- Spencer, J. R.; Pearl, J. C.; Segura, M.; Flasar, F. M.; Mamoutkine, A.; Romani, P.; Buratti, B. J.; Hendrix, A. R.; Spilker, L. J.; Lopes, R. M. C. *Science* **2006**, *311*, 1401–1405.
- Spitale, J. N.; Hurford, T. A.; Rhoden, A. R.; Berkson, E. E.; Platts, S. S. *Nature* **2015**, *521*, 57–60.
- Stevenson, K. P.; Kimmel, G. A.; Dohnálek, Z.; Smith, R. S.; Kay, B. D. *Science* **1999**, *283*, 1505–1507.
- Suchan, M. M.; Ph. D. thesis; University of Southern California; 2001.
- Thrower, J. D.; Collings, M. P.; Rutten, F. J. M.; McCoustra, M. R. S. *J. Chem. Phys.* **2009**, *131*, 244711.
- van Dishoeck, E. F. *Faraday Discuss.* **2014**, *168*, 9–47.
- van Dishoeck, E. F.; Herbst, E.; Neufeld, D. A. *Chem. Rev.* **2013**, *113*, 9043–9085.
- Veith, G. M.; Lupini, A. R.; Rashkeev, S.; Pennycook, S. J.; Mullins, D. R.; Schwartz, V.; Bridges, C. A.; Dudney, N. J. *J. Catal.* **2009**, *262*, 92–101.
- Waite, Jr., J. H.; et al. *Nature* **2009**, *460*, 487–490.
- Wang, H.; Bell, R. C.; Iedema, M. J.; Tsekouras, A. A.; Cowin, J. P. *Astrophys. J.* **2005**, *620*, 1027–1032.
- Westley, M. S.; Baratta, G. A.; Baragiola, R. A. *J. Chem. Phys.* **1998**, *108*, 3321–3326.
- Wiley, W. C.; McLaren, I. H. *Rev. Sci. Instrum.* **1955**, *26*, 1150–1157.
- Yabushita, A.; Hama, T.; Iida, D.; Kawanaka, N.; Kawasaki, M.; Watanabe, N.; Ashfold, M. N. R.; Looock, H.-P. *J. Chem. Phys.* **2008**, *129*, 044501.
- Yabushita, A.; Inoue, Y.; Senga, T.; Kawasaki, M. *J. Phys. Chem. A* **2004**, *108*, 438–446.
- Yates, Jr., J. T. *Experimental Innovations in Surface Science*; AIP Press Springer-Verlag: New York, 1998.
- Yu, X.; Leitner, D. M. *J. Chem. Phys.* **2005**, *123*, 104503(10).
- Zhigilei, L. V.; Kodali, P. B. S.; Garrison, B. J. *J. Phys. Chem. B* **1998**, *102*, 2845–2853.